Optical polarization anisotropy in nonpolar GaN thin films due to crystal symmetry and anisotropic strain

DISSERTATION

zur Erlangung des akademischen Grades
doctor rerum naturalium
(Dr. rer. nat.)
im Fach Physik

eingereicht an der
Mathematisch-Naturwissenschaftlichen Fakultät I
Humboldt-Universität zu Berlin

von
Herr M.Sc. Pranob Misra
geboren am 17.01.1979 in Dehradun, Indien

Präsident der Humboldt-Universität zu Berlin:
Prof. Dr. Hans Jürgen Prömel (in Vertretung)

Dekan der Mathematisch-Naturwissenschaftlichen Fakultät I:
Prof. Thomas Buckhout, PhD

Gutachter:

1. Prof. Dr. Klaus H. Ploog
2. Prof. Dr. Oliver Benson
3. Prof. Dr. Elias Muñoz

eingereicht am: 6. October 2005
Tag der mündlichen Prüfung: 13. Dezember 2005

Zusammenfassung

Diese Arbeit befasst sich mit den optischen Eigenschaften von dünnen GaN-Schichten verschiedener Orientierungen. Hierbei werden die optischen Eigenschaften von verspannten *M*- und *A*-plane sowie unverspannten *C*-plane GaN-Schichten untersucht und die Ergebnisse im Rahmen von Bandstrukturberechnungen diskutiert. Die unverspannten *C*-plane Schichten zeigen dabei aufgrund ihrer Kristallsymmetrie keine Anisotropie der optischen Polarisation in der Filmebene. Im Falle der *M*- und *A*-plane GaN-Schichten liegt jedoch die ausgewählte c-Achse in der Schichtebene, so dass für Licht, welches senkrecht zur Schichtebene einfällt, eine starke Anisotropie bzgl. der Polarisationeigenschaften in der Filmebene erwartet wird. Diese wird in der Tat experimentell beobachtet und durch theoretische Rechnungen bestätigt. Die Anisotropie hat zwei Beiträge:
— die reduzierte Symmetrie des Kristallgitters bei *M*- und *A*-plane GaN sowie
— die Modifikation der elektronischen Bandstruktur durch eine biaxiale, anisotrope Verspannung in der GaN-Schichtebene.

Im Rahmen dieser Arbeit werden die Bandstrukturveränderungen theoretisch mittels eines $\mathbf{k}\cdot\mathbf{p}$-Näherungsansatzes untersucht. Diese Veränderungen beeinflussen sowohl die Übergangsenergien als auch die Oszillatorstärken. Man findet, dass die *C*-plane Schicht im Falle einer isotropen Verspannung in der Filmebene keine Anisotropie der optischen Polarisation zeigt. Allerdings erwartet man eine Anisotropie in der optischen Antwort, wenn eine stark anisotrope Verspannung in dem Film erzeugt wird. Im Fall der *M*-plane Schichten erwartet man eine Polarisationsanisotropie auch für die unverspannte Schicht. Eine Verspannung in der Filmebene führt dann zu einer zusätzlichen, signifikanten Änderung der Bandstruktur und der Symmetrie der Valenzbandzustände. Die Abhängigkeit der Übergangsenergien und der Oszillatorstärken in *A*-plane GaN-Schichten von der Verspannung in der Filmebene entspricht der im *M*-plane GaN, wenn man die x- und y-Achse vertauscht. In beiden Fällen zeigen die drei Übergänge von den drei oberen Valenzbändern in das untere Leitungsband andere Polarisationseigenschaften als die entsprechenden Übergänge in *C*-plane GaN-Schichten. Für einen bestimmten Wertebereich der Verspannung in der Filmebene sind diese Übergänge nahezu vollständig *x*-,*z*- bzw. *y*-artig polarisiert. Die Übergangsenergien werden mit verschiedenen optischen Methoden bestimmt und die Ergebnisse mit den theoretischen Rechnungen verglichen.

Die verwendeten Schichten wurden auch mittels Transmissionspektroskopie untersucht. Im Falle der *M*-plane GaN-Schichten können zwei fundamentale Übergänge identifiziert werden, wobei der elektrische Feldvektor $\boldsymbol{E}$ des einfallenden Lichtes einmal parallel und einmal senkrecht auf der c-Achse steht. Die zugehörigen Transmissionspektren sind bei Raumtemperatur um 50 meV gegeneinander verschoben. Die *M*-plane GaN-Schicht besitzt unterschiedliche Dielektrizitätskonstanten für $\boldsymbol{E} \parallel \boldsymbol{c}$ und $\boldsymbol{E} \perp \boldsymbol{c}$, welche zu zusätzlichem Dichroismus und Doppelbrechung führen. Als Resultat findet eine Filterung der Polarisation für einfallendes, linear polarisiertes Licht statt. Die elektrische Feldkomponente $\perp \boldsymbol{c}$ wird stärker absorbiert als die Komponente $\parallel \boldsymbol{c}$. Diese Polarisationsfilterung äußert sich für schmalbandiges Licht in Form einer Drehung der Polarisationsebene in Richtung der c-Achse, wobei ein maximaler Rotationswinkel von 40° gefunden wurde. Die gemessene Rotation wurde mit Ergebnissen aus Rechnungen verglichen, die auch die Doppelbrechung der GaN-Schicht berücksichtigten. Im Energiebereich, in dem die Polarisationsfilterung am effektivsten ist, ist der Effekt der Doppelbrechung verschwindend gering und kann somit bei der Bestimmung des Rotationswinkels vernachlässigt werden. Weiterhin ist der Rotationswinkel, welcher durch den Quotienten der jeweiligen Transmittanzen entlang der beiden ausgezeichneten Achsen $\perp c$ und $\parallel c$ gegeben ist, näherungsweise durch das Produkt aus Schichtdicke und Differenz der Absorptionskoeffizienten beider Polarisationsrichtungen bestimmt.

Weiterhin wird die Polarisationsanisotropie in der Photolumineszenz (PL) von *M*-plane und *A*-plane GaN-Schichten bei tiefen und höheren Temperaturen untersucht. Um die Anisotropie zu quantifizieren, wird der Polarisationsgrad berechnet. Bei tiefen Temperaturen ist nur das oberste Valenzband besetzt, was zu einem hohen Polarisationsgrad führt. Mit zunehmender Temperatur steigt die Besetzung des zweithöchsten Valenzbandniveaus und der Polarisationsgrad nimmt ab.

Schlagwörter:
Galliumnitrid, Nichtpolare Flächen von GaN, Bandstrukturberechnungen, Dünne Filme, Optische Eigenschaften, Polarisationsanisotropie

Abstract

In this work, we focus on the optical response of GaN thin films grown along various orientations.

The optical properties of strained *M*- and *A*- and unstrained *C*-plane GaN thin films are investigated, and the results are explained with help of band-structure calculations. Unstrained *C*-plane films do not show any in-plane polarization anisotropy due to the underlying crystal symmetry. However, the surface normal of *M*- or *A*-plane films is perpendicular to the unique *c* axis of the wurtzite crystal structure of GaN, and the optical properties of such films are therefore expected to be strongly dependent on the in-plane polarization of a normally incident light beam. This anisotropy has two contributions:
— the reduced crystal symmetry of the *M* and *A* plane of GaN.
— the electronic band structure (EBS) modification due to the biaxial, anisotropic in-plane strain in the layer.

We calculate the strain-induced band-structure modification using the $\mathbf{k}\cdot\mathbf{p}$ perturbation approach. The valence-band (VB) states are modified affecting both the transition energies as well as the oscillator strengths. We observe that *C*-plane GaN does not show any in-plane polarization anisotropy, when an isotropic in-plane strain is applied. However, one expects to see an anisotropy in the optical response with the application of an anisotropic in-plane strain. For the case of *M*-plane and *A*-plane GaN, one expects to see an in-plane polarization anisotropy even for the unstrained case. Additionally, the in-plane strain significantly changes the band structure and the symmetry of the VB states. The dependence of the transition energies and the values of oscillator strength on the in-plane strain, for *A*-plane GaN is similar to *M*-plane GaN except for the exchange of *x* and *y* axis. The three transitions, involving electrons in the conduction band (CB) and holes in the top three VBs, will exhibit a very different polarization characteristic than the ones for *C*-plane GaN. These transitions are labelled as T_1, T_2, and T_3 and are predominantly *x*, *z*, and *y* polarized, respectively, for a certain range of in-plane strain values, present in our samples. We measure the energies for these transitions using various optical methods and compare these values with the one derived from the theoretical calculations.

For *M*-plane GaN thin films, two fundamental transitions can be identified, which occur when the electric field vector $\boldsymbol{E}$ is $\perp$ and $\parallel$ $\boldsymbol{c}$. These transitions give rise to a transmittance spectrum separated by 50 meV at room temperature with respect to each other. The *M*-plane GaN film also exhibits different dielectric constants for $\boldsymbol{E} \parallel \boldsymbol{c}$ and $\boldsymbol{E} \perp \boldsymbol{c}$ giving rise to linear dichroism in addition to linear birefringence. This results in a polarization filtering of an incident, linearly polarized light beam after transmission, because the component of the electric field vector $\perp$ $\boldsymbol{c}$ is more strongly absorbed than the one $\parallel$ $\boldsymbol{c}$. This filtering manifests itself, for quasi monochromatic light, as a rotation of the polarization vector toward the *c* axis and can be as large as 40° for an initial angle of 60°, for our samples. We compare the measured polarization rotation with calculated values taking into account the birefringence of the GaN film. In the energy range where the filtering is most effective, the birefringence almost disappears and can therefore be neglected for the determination of the rotation angle. Finally, the rotation, which is determined by the transmittance for the two orthogonal polarization directions, can be very well approximated by the product of the film thickness and the difference of the absorption coefficients for the two polarization directions.

The in-plane polarization anisotropy is also studied in emission for both the *M*- and the *A*-plane GaN thin films by measuring the photoluminescence (PL) spectra at low and elevated temperatures. The degree of polarization (ρ) is calculated to quantify the in-plane polarization anisotropy. At low temperatures, only the top most VB state is occupied giving rise to a large value of ρ. As the occupation of the second highest VB state increases with increasing temperature, the degree of polarization decreases.

Keywords:
Gallium Nitride, Nonpolar planes of GaN, band-structure calculations, thin films, optical properties, polarization anisotropy

Parts of this work have already been published:

Pranob Misra, Yue Jun Sun, Oliver Brandt, and Holger T. Grahn, *Angular dependence of the in-plane polarization anisotropy in the absorption coefficient of strained M-plane GaN films on γ-$LiAlO_2$*, Phys. Status Solidi B **240**, 293-296 (2003).

Pranob Misra, Yue Jun Sun, Oliver Brandt, and Holger T. Grahn, *In-plane polarization anisotropy and polarization rotation for M-plane GaN films on $LiAlO_2$*, Appl. Phys. Lett. **83**, 4327-4329 (2003).

Pranob Misra, Yue Jun Sun, Oliver Brandt, and Holger T. Grahn, *Polarization filtering by nonpolar M-plane GaN films on $LiAlO_2$*, J. Appl. Phys. **96**, 7029-7035 (2004).

Pranob Misra, Yue Jun Sun, Oliver Brandt, and Holger T. Grahn, *Polarization anisotropy and filtering for M-plane GaN films*, Phys. Status Solidi C **2**, 2704-2707 (2005).

Kunimichi Omae, Timur Flissikowski, Pranob Misra, Oliver Brandt, Holger T. Grahn, K. Kojima and Y. Kawakami, *Dynamic polarization filtering in anisotropically strained M-plane GaN films*, Appl. Phys. Lett. **86**, 191909, 3 pages (2005).

Sandip Ghosh, Pranob Misra, Holger T. Grahn, Bilge Imer, Shuji Nakamura, S. P. DenBaars, and J. S. Speck, *Polarized photoreflectance spectroscopy of strained A-plane GaN films on R-plane sapphire*, J. Appl. Phys. **98**, 026105, 3 pages (2005).

Abbreviations

CB	Conduction Band
cw-PL	Continuous Wave Photoluminescnece
EBS	Electronic Band Structure
LB	Linear Birefringence
LD	Linear Dichroism
μ PL	Micro Photoluminescence
MOVPE	Metal-Organic Vapor-Phase Epitaxy
MQW	Multiple Quantum Well
PAMBE	Plasma-Assisted Molecular Beam Epitaxy
PEM	Photo-Elastic Modulator
PL	Photoluminescence
PR	Photoreflectance
PSPD	Polarization Sensitive Photodetector
R	Reflectance
RHEED	Reflection High-Energy Electron Diffraction
RT	Room Temperature
SEM	Scanning Electron Microscopy
T	Transmittance
UV	Ultra Violet
VB	Valence Band
WZ	Wurtzite
XRD	X-Ray Diffraction

Contents

1 Introduction **1**
1.1 Nonpolar planes of GaN — Polarization anisotropy 2
1.2 Aim of this work 3

2 Structural and optical properties of GaN **5**
2.1 Crystal structure of GaN 5
2.2 Strain and stress 7
2.2.1 Strain state for different growth orientations 8
2.2.2 Measurement of the out-of-plane strain 10
2.3 Modification of the band structure due to biaxial strain 12
2.3.1 Bir-Pikus approach for ***k.p*** perturbation in wurtzite semiconductor 13
2.3.2 Strain modified band structure for *C*-, *M*- and *A*-plane GaN . . . 16
2.4 Summary 26

3 Structural properties of GaN thin films **27**
3.1 *C*-plane GaN thin films on a GaN template 27
3.2 *M*-plane GaN thin films on lithium aluminate 28
3.3 *A*-plane GaN thin films on *R*-plane sapphire 30
3.4 Summary 31

4 Optical processes in GaN semiconductors **32**
4.1 Basics of optical properties and measurements techniques 32
4.1.1 The complex dielectric function in isotropic media 32
4.1.2 Relationship between optical constants 34
4.1.3 Absorption versus emission processes in semiconductors 35
4.1.4 Photoreflectance spectroscopy 37
4.1.5 Photoluminescence spectroscopy 39
4.2 Optical characterization of GaN semiconductor thin films 41
4.2.1 *C*-plane GaN films 42
4.2.2 *M*-plane GaN films 47
4.2.3 *A*-plane GaN films 57
4.3 Summary 60

5 Polarization anisotropy in *M*-plane GaN thin films **62**
5.1 Electromagnetic wave propagation in layered media 62
5.1.1 Matrix formulation for isotropic layered media 63
5.1.2 Wave propagation in anisotropic layered media 68

5.1.3 Experimental evidence of polarization anisotropy 72
5.1.4 Calculation of the refractive index and absorption coefficient for *M*-plane GaN thin films 75
5.1.5 Polarization filtering and rotation 80
5.1.6 Polarization rotation for linearly polarized light at an angle of 45 degrees 81
5.1.7 Polarization rotation for linearly polarized light at arbitrary polarization angle 83
5.1.8 Linear dichroism and birefringence in *M*-plane GaN 84
5.1.9 Polarization rotation taking linear dichroism and linear birefringence into account 85
5.1.10 Dynamic polarization filtering in *M*-plane GaN films 90
5.2 Summary 90

6 Polarization anisotropy of photoluminescence... 92
6.1 *M*-plane GaN thin films 93
6.2 *A*-plane GaN thin films 96
6.3 Summary 98

7 Conclusions and outlook 99

A Mathematical and experimental determination... 101
A.1 A mathematical framework for the measurement of polarization rotation 101
A.1.1 Mueller calculus : Stokes vector & Mueller matrix 101
A.2 Experimental setup 103

Acknowledgement 113

Curriculum Vitae 115

Selbständigkeitserklärung 116

Chapter 1

Introduction

Epitaxial GaN and its alloys with Al and In are emerging wide-gap semiconductors well suited for the fabrication of semiconductor devices including visible-ultraviolet light emitting diodes and lasers, visible-ultraviolet detectors, and high-temperature, high-frequency transistors.[1] As such, this alloy system in conjunction with the established arsenide- and phosphide-based systems can be used to create full color displays. GaN and its alloys crystallize, at ambient pressures, in the hexagonal wurtzite structure, and therefore, are polarized at equilibrium since they have a singular polar axis, the [0001] axis. In contrast, zincblende structure, the common crystal symmetry for other semiconductors, is not polarized in equilibrium as it has four symmetry-equivalent polar axes, whose contributions cancel each other.

The vast majority of group III-nitride devices are grown along the [0001] *c* axis of the wurtzite (WZ) crystal structure, referred to as *C*-plane growth. While *C*-plane oriented (Al,In,Ga)N films are the most commonly grown nitrides for device applications, the active layers of the optoelectronic devices grown along this orientation suffer from undesirable spontaneous and piezoelectric polarization effects which generate electrostatic fields. [2] These electrostatic fields give rise to quantum-confined Stark effect and tend to separate the electron and the hole wave functions in a quantum well, reducing their overlap and resulting in a lower luminous efficiency due to a lower transition probability. The uniqueness of the [0001] polar axis of the wurtzite phase implies that any direction orthogonal to it, such as $[1\bar{1}00]$ (Ref. [3]), will not carry spontaneous polarization components. At the same time, these directions will carry no piezoelectric polarization, if shear stresses in the growth plane are absent.

Recently, it has been demonstrated that such electrostatic fields can be avoided by growing $(1\bar{1}00)$-oriented *M*-plane GaN heterostructures.[4] The successful synthesis and demonstration of an improved quantum efficiency of GaN/(Al,Ga)N quantum wells has triggered a surge of activity in studying nonpolar group-III nitride thin films and heterostructures. Efforts in this direction have been made using *M*-plane structures such as GaN films, [5] GaN/(Al,Ga)N, [4, 6] and (In,Ga)N/GaN [7, 8] multiple-quantum-well (MQW) structures grown on γ-$LiAlO_2$. More recently, $(11\bar{2}0)$-oriented *A*-plane structures such as GaN films, [9, 10, 11, 12] GaN/(Al,Ga)N MQWs, [13, 14, 15, 16, 17, 18] and (In,Ga)N/GaN MQWs [19, 20, 21] have been realized on *R*-plane sapphire.

The plane orthogonal to the *C* plane are termed as nonpolar, since the cations and the anions on this surface, are equal in number.

1.1 Nonpolar planes of GaN — Polarization anisotropy

In addition to improved luminous efficiency, the nonpolar GaN films, which include the *M* plane and *A* plane, have a distinct advantage, in comparison to the *C*-plane GaN, that the unique *c* axis of the WZ crystal structure lies in the growth plane. This leads to an anisotropy in the optical properties of the film for the electric-field vector $\boldsymbol{E}$ of the incident light beam polarized parallel ($\parallel$) and perpendicular ($\perp$) to the *c* axis. Such in-plane polarization anisotropy in the optical response is absent in *C*-plane oriented films, because the unique *c* axis lies in the growth direction and it is difficult to achieve, for the case of thin films, significant optical polarization parallel to this axis. Note that in-plane polarization anisotropy is an optical property of nonpolar GaN, where the optical response depends on the angle which the polarization vector of the incident linearly polarized light makes with the *c* axis of WZ crystal structure. It is very different than the piezoelectric and spontaneous polarization in GaN based heterostructures which give rise to electrostatic fields. The optically anisotropic response for materials such as nonpolar GaN can be used to fabricate devices, in which the state of optical polarization is of critical importance for optical information processing. The usual group IV and III-V semiconductor thin films do not show any significant in-plane anisotropy in their optical absorption coefficient α due to their cubic crystal structure, which has high crystal symmetry. This symmetry breaks down in the case of the WZ crystal structure, even more so for nonpolar planes as compared to the *C* plane, which still maintains the hexagonal symmetry, giving rise to intrinsic polarization anisotropy.

Recently, it has been shown that strained *M*-plane GaN films are a potential candidate for the fabrication of polarization-sensitive photodetectors (PSPDs).[22, 23] Because of the combination of a large mismatch in lattice constants and thermal expansion coefficients between GaN and commonly used substrates, even thick GaN films are usually strained. Since strain affects the electronic band structure (EBS), it further modifies the polarization selection rules for optical absorption. Similar modifications of the band structure due to the in-plane strain were also reported for isotropic materials such as GaAs, which can exhibit a polarization anisotropy in the in-plane dielectric function, when anisotropic strain reduces the underlying symmetry of the valence bands (VBs), resulting in a mixing of heavy- and light-hole states.[24] The advantage of an intrinsically anisotropic material for the fabrication of PSPDs is that it allows for the miniaturization of the detection system, leading to a large-scale integration and easier alignment. No external polarizing element, such as sheet polarizers and prisms is needed which is inconvenient from the point of view of economics and mechanical aspects such as size and alignment.

In addition to using anisotropic materials for the fabrication of PSPDs, the anisotropic crystal properties of $CuPt_B$-type ordered materials such as $In_{0.5}Ga_{0.5}P$ alloys have been increasingly utilized for new devices such as tunable polarization

converters[25] and polarized light-emitting diodes[26] as well as new device features such as polarization stabilization of vertical-cavity surface-emitting lasers.[27, 28] Polarization threshold switches[29] and reset-set flip flops[30] have also been realized using ordered $In_{0.5}Ga_{0.5}P$ alloys, which exhibit different absorption coefficients along the $[011]$ and $[01\bar{1}]$ directions. However, the $CuPt_B$-type alloy ordering and the resulting in-plane polarization anisotropy in the absorption coefficient becomes weaker, if a higher Ga concentration is used to increase the band-gap energy. Therefore, a limitation of $In_{0.5}Ga_{0.5}P$ is the narrow range of its operating wavelength.

In addition to the above applications, modulators based on the rotation of the polarization vector have been demonstrated in uniaxially strained, [001]-oriented GaAs/(Al,Ga)As MQWs [31, 32] and biaxially strained [110]-oriented MQWs [33], which has both a high contrast and a fast response. Linear dichroism due to inherent or strain-induced anisotropies in the VB structure gives rise to polarization filtering, which appears as a rotation of the polarization vector after transmission of linearly polarized light.[31, 34] The polarization rotation can be modulated by selective photoexcitation, since the photoexcited carriers bleach the anisotropic absorption and remove the static linear dichroism. [35]

1.2 Aim of this work

Although nonpolar GaN is an ideal candidate for the fabrication of devices based on optical in-plane polarization anisotropy, a fundamental knowledge concerning the optical properties of the nonpolar thin films is essential in predicting the optical response and the design of these devices. This work is concerned with the theoretical and experimental investigation of the electronic band structure of GaN thin films and its modification due to the in-plane strain. Nonpolar planes including the *M* and the *A* planes are investigated, and their properties are compared to *C*-plane GaN. The goal of this study is to elucidate the differences between the properties of the commonly used *C*-plane films, and films grown along the nonpolar orientations. The in-plane polarization anisotropy in the optical response of nonpolar GaN can be used by incorporating them in advanced active devices which are based on polarization-coded logic.

In Chapter 2, we study the EBS modification of the various planes of GaN (*C*, *M*, and *A* plane) due to the in-plane strain in these layers. The strain in the epitaxially grown films is inevitably present due to the mismatch in the lattice constants and the thermal expansion coefficients between the substrate and GaN. A theoretical investigation of the influence of the in-plane strain on the band structures, with special emphasis on the wave function characteristic of the valence band states, the oscillator strength, and the resulting polarization properties of the three band-edge transitions is carried out. This study distinguishes the state of strain for the *C*-plane case, where the in-plane strain is isotropic in nature for samples grown on substrates having hexagonal symmetry, as opposed to anisotropic in-plane strain in the case of *M*- and *A*-plane GaN. Furthermore, the presence of the unique *c* axis in the film plane lowers the symmetry of the nonpolar orientations, giving rise to anisotropic optical polarization properties.

In Chapter 3, a brief introduction to the growth conditions and the quantification of the out-of-plane strain in the film is done. The *C*-plane GaN film is grown on a thick GaN template, while the *M*-plane film is grown on γ-$LiAlO_2$. Both samples are grown by plasma-assisted molecular-beam epitaxy (PAMBE). The growth condition for these samples are well-established giving rise to good results in terms of surface morphology and crystal quality. The *A*-plane GaN sample is grown on *R*-plane sapphire by metal-organic vapor phase epitaxy (MOVPE). The strain state for all the samples is measured using high-resolution x-ray diffraction.

In Chapter 4, the optical properties of GaN grown along different orientations is studied using spectroscopic techniques such as reflectance, transmittance, photoluminescence, and photoreflectance. The energy of the excitonic transitions involving the electrons in the conduction band (CB) and the holes in the top three valence bands is determined. The transition energies obtained for nonpolar planes are different as compared to unstrained *C*-plane GaN. This difference in energy is explained in terms of the strain in the film. In addition to the transition energies, the polarization properties quantified by the oscillator strengths is also different for the various samples with different orientations. The symmetry of the wave function of the VB state determines the components of the oscillator strength and, therefore, the polarization selection rules. The theoretical results for the strain-induced modification of the EBS are used to explain the experimental results.

In Chapter 5, the in-plane polarization anisotropy in absorption is studied in detail for *M*-plane GaN films. Two fundamental directions are identified, which are parallel and perpendicular to unique *c* axis of the WZ crystal structure. The anisotropic optical properties of *M*-plane GaN thin films include — in addition to linear birefringence typically observed in the transparency regime below the energy gap — also linear dichroism, i.e., different absorption coefficients for different polarization directions. The dichroism manifests itself in a polarization filtering, which can be directly observed as a rotation of the polarization vector of the incoming linearly polarized light beam after transmission. It is found that, in addition to the reduced symmetry of the nonpolar planes of GaN, anisotropic in-plane strain can drastically enhance the in-plane polarization anisotropy, thereby increasing the effectiveness of polarization filtering and rotation.

In Chapter 6, an in-plane polarization anisotropy in emission is studied for the *M*- and *A*-plane GaN films and the observed anisotropy is explained in terms of the band structure.

Chapter 2

Structural and optical properties of GaN

2.1 Crystal structure of GaN

There are two common crystal structures existing for group-III nitrides: the wurtzite and the zincblende structures. The wurtzite crystal structure is thermodynamically stable for bulk GaN, AlN and InN. The zincblende crystal structure for the group-III nitrides has been stabilized by epitaxial growth of thin films on cubic substrates such as Si and GaAs. The wurtzite crystal structure has a hexagonal unit cell and thus two lattice constants, c and a. It contains two atoms of each type in the unit cell and belongs to the space group $P6_3mc$. This structure consists of two inter-penetrating hexagonal close packed (HCP) sublattices, each with one type of atoms offset along the c axis by 3/8 of cell height, i.e., 3c/8. The zincblende structure has a cubic unit cell containing one atom of the group-III element and one nitrogen atom. The zincblende and wurtzite structures are similar as for both the atoms of the group-III element is coordinated by 4 N atoms and vice versa. Although, both these structures are tetrahedrally coordinated, the main difference is that, while in zincblende structure, looking in the direction of the body diagonal of the cube, the adjacent planes of cation and anion are rotated by 180° with respect to each other. This rotation is absent in wurtzite structure. Furthermore, the stacking sequence of the closed-packed diatomic planes is also different. For the wurtzite structure, the stacking sequence of the (0001) plane is ABABABA in the [0001] direction, while for the zincblende structure, the stacking sequence of the (111) plane is ABCABC along the [111] direction, where the letter A, B or C represents a anion-cation bond like Ga-N.

A stick and ball representation of the wurtzite crystal structure for GaN is depicted in Fig. 2.1(a). The figure shows the four-fold coordination of Ga with N and vice versa. Figure 2.1(b) shows a schematic diagram of the wurtzite crystal structure, depicting the various planes and directions. In the hexagonal crystal system, a four-axis coordinate system is used to identify the various planes and directions. The four indices are called the Miller-Bravais indices, and a plane is defined by 4 indices, i.e., $(h\,k\,i\,l)$. As the three basis vectors are in-plane with an angle of 120° to each other, it follows $-i = h + k$. The planes of the same family are identified by permutations of the first three indices, as is the case for the Miller indices of the cubic systems. As clearly shown in Fig. 2.1(a), the

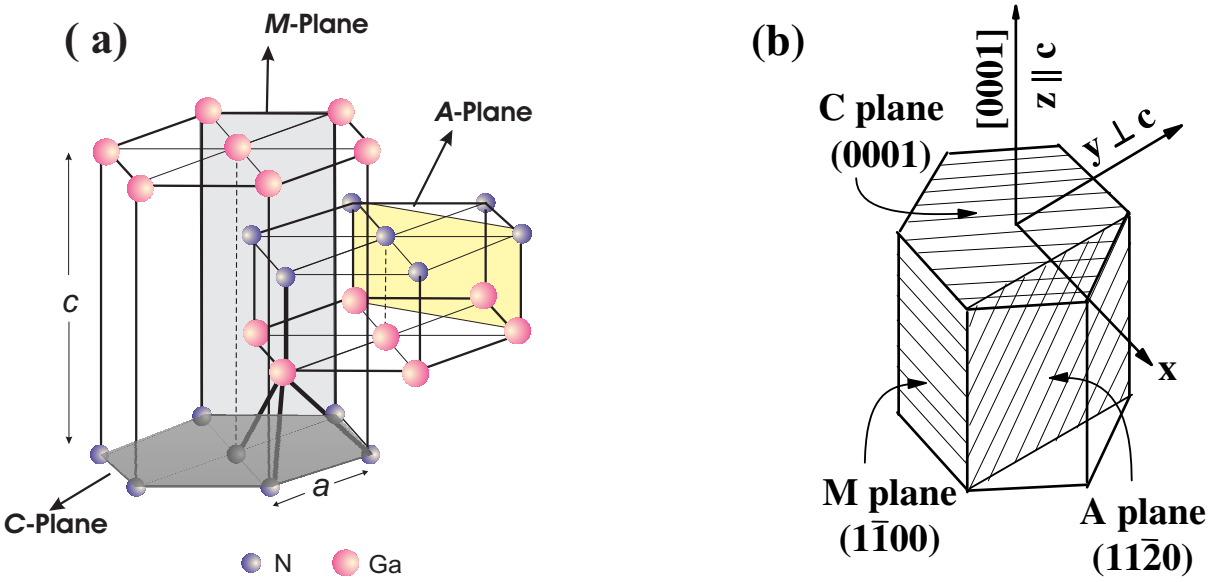

Figure 2.1: (a) Atomic coordination for the wurtzite crystal structure in GaN. The Ga and N atoms have a four-fold coordination. The c and a lattice constants are also shown. (b) Schematic diagram of the wurtzite unit cell. The coordinate system and the Miller indices for the C, M, and A planes are shown.

stacking sequence of the wurtzite GaN along the [0001], i.e., the c direction is ABABAB. According to the Miller index system, the C plane is (0001) or (000$\bar{1}$), the M plane (1$\bar{1}$00) and permutations thereof, while the A plane is denoted by family of (11$\bar{2}$0) planes. There are 2 C planes, 6 M planes and 6 A planes as can be seen in Fig. 2.1(b). The C plane is normal to any of the M or A planes, while one can always find a pair of M and A planes, which are orthogonal to each other. The C plane is a polar plane of the wurtzite crystal structure in the sense that it is either a cation-terminated face or an anion-terminated face. This is clearly depicted in Fig. 2.1(a). The figure also shows the M and A planes, which are nonpolar because in these planes there is an equal number of cations and anions. The schematic diagram in Fig. 2.1(b) shows the nomenclature for the various directions. The z-direction is along c axis [0001], which is normal to the C plane, while the x axis is along [11$\bar{2}$0], which is normal to the A plane. The y axis is parallel to [1$\bar{1}$00], which is normal to the M plane.

GaN is mainly prepared by heteroepitaxy, i.e., an epitaxial deposition process, in which a material is deposited on a structurally and/or chemically dissimilar substrate. The lattice constants of the layer will generally be different to the one of the substrate. This difference inevitably leads to strain in the films because of the mismatch of the lattice constants and the thermal expansion coefficients between the epilayer and the substrate. Until recently, GaN layers were mostly grown in C-plane orientation, in which the growth direction is along the [0001] axis, the unique c axis of wurtzite crystal structure. The quantum efficiency of the active layers based on C-plane GaN is theoretically lower than the ones grown along nonpolar directions, due to the presence of electrostatic fields within the heterostructure.[4, 36, 37]. These fields are generated by the spontaneous and piezoelectric polarizations [2, 36] along the [0001] axis of hexagonal group-III nitrides heterostructures. To circumvent this problem, recent developments have been undertaken, with an increasing interest in the growth of nonpolar planes

of GaN. [6, 8, 13, 17, 18, 38, 39, 40, 41, 42] This leads to no spontaneous polarizations along the GaN/(Al,Ga)N [4] interface or the (In,Ga)N/GaN interface in the MQWs grown for the active region.

Throughout this work, we will mostly discuss the structural and the optical properties of *M*-plane GaN, which is grown on tetragonal γ-$LiAlO_2$(100) substrates . Additionally *A*-plane [11$\bar{2}$0] GaN, which is also nonpolar and is grown on *R*-plane [1$\bar{1}$02] sapphire, will be examined. We will also compare the results of these nonpolar GaN films to the homoepitaxially grown *C*-plane GaN. The purpose of this chapter is to give an overview of the consequences of the biaxial, isotropic and anisotropic in-plane strain on the structural and optical properties of *C*-, *M*-, and *A*-plane GaN films.

2.2 Strain and stress

A general deformation of the solid is described in terms of a continuous deformation field **u**(**r**), specifying the vector displacement of the part of the solid that, in equilibrium, occupies the position **r** such that **r**=(**x**,**y**,**z**). The bold font denotes a vector quantity. The strain tensor, ε_{ij}, being symmetric is related to the deformation field by the equation

$$\varepsilon_{ij} = \frac{1}{2}\left(\frac{du_j}{dx_i} + \frac{du_i}{dx_j}\right) , \tag{2.1}$$

where i, j = 1,2 and 3 for the three spatial directions. For a sufficiently small stress σ, the amount of strain is, according to Hooke's law, proportional to the magnitude of the applied stress. Hooke's law therefore states that

$$\sigma_{ij} = c_{ijkl}\varepsilon_{kl} , \tag{2.2}$$

where c_{ijkl} are the 3^4=81 stiffness constants and $i, j, k, l = 1, 2$, or 3. Einstein's summation rule is used, where the summation is executed over repeated indices such that S_{ij} M_j = $\sum_{j=1-3} S_{ij}M_j$. Based on the symmetry of the stress and strain tensors, the elastic stiffness constants have the following symmetry properties: $c_{ijkl} = c_{jikl} = c_{ijlk}$. The equalities of the first two and the last two suffixes reduce the independent stiffness constants to 36. It can also be shown that $c_{ijkl} = c_{klij}$. This relation further reduces the number of constants to 21. Since the wurtzite crystal belongs to the C_{6v}^4 space group, the maximum number of constants required for GaN are 5.[43] The displacement field is usually described by the strain components, ϵ, instead of the strain fields, ε. Therefore, the stress and the strain components are frequently written in contracted notation. It can be shown that for the stiffness constants c_{ijkl} the first two suffixes are abbreviated by a single suffix, which varies from 1 to 6, and the last two are abbreviated in the same way. Therefore, we have the following scheme:

tensor notation	11	22	33	23, 32	31, 13	12, 21
matrix notation	1	2	3	4	5	6

(2.3)

We, thus, reduce the 4 index tensor system, c_{ijkl}, to a 2 index pseudo-tensor system, i.e., C_{ij}. Besides that we are dealing with 2 instead of 4 indices in replacing the two suffices (i, j) and (k, l) by single suffices, this expression has the advantage that it enables

us to consider the contracted variables, C_{ij} as elements of a matrix. The disadvantage is that these elements of a matrix cannot be manipulated by the rules of tensor transformation. Taking into account the wurtzite crystal symmetry of GaN, one obtains the following relation denoting the generalized Hooke's law

$$\begin{pmatrix} \sigma_{xx} \\ \sigma_{yy} \\ \sigma_{zz} \\ \sigma_{yz} \\ \sigma_{xz} \\ \sigma_{xy} \end{pmatrix} = \begin{pmatrix} C_{11} & C_{12} & C_{13} & 0 & 0 & 0 \\ C_{12} & C_{11} & C_{13} & 0 & 0 & 0 \\ C_{13} & C_{13} & C_{33} & 0 & 0 & 0 \\ 0 & 0 & 0 & C_{44} & 0 & 0 \\ 0 & 0 & 0 & 0 & C_{44} & 0 \\ 0 & 0 & 0 & 0 & 0 & C_{66} \end{pmatrix} \begin{pmatrix} \epsilon_{xx} \\ \epsilon_{yy} \\ \epsilon_{zz} \\ \epsilon_{yz} \\ \epsilon_{xz} \\ \epsilon_{xy} \end{pmatrix} , \tag{2.4}$$

where $1 \rightarrow x$, $2 \rightarrow y$, and $3 \rightarrow z$ and $C_{66} = \frac{C_{11}-C_{12}}{2}$. Normally, the film does not incorporate any shear strain and thus the values σ_{xy}, σ_{xz}, and σ_{yz} are equal to zero. Therefore, the matrix in Eq. (2.4) can be simplified to a 3×3 matrix. The stress and strain are related by 4 elements of the elastic stiffness constant C_{ij} according to:

$$\begin{pmatrix} \sigma_{xx} \\ \sigma_{yy} \\ \sigma_{zz} \end{pmatrix} = \begin{pmatrix} C_{11} & C_{12} & C_{13} \\ C_{12} & C_{11} & C_{13} \\ C_{13} & C_{13} & C_{33} \end{pmatrix} \begin{pmatrix} \epsilon_{xx} \\ \epsilon_{yy} \\ \epsilon_{zz} \end{pmatrix} , \tag{2.5}$$

2.2.1 Strain state for different growth orientations

***C* plane: Growth along** [0001]

The growth direction for the *C*-plane GaN films is along the *z*-direction, which is parallel to the *c* axis, i.e., [0001]. The corresponding strain arising in the growth plane is usually isotropic, i.e., $\epsilon_{xx} = \epsilon_{yy}$, because *C*-plane films are mostly grown on substrates having a hexagonal symmetry, e.g., *C*-plane SiC or *C*-plane sapphire. The strain components are thus $\epsilon_{\parallel} = \epsilon_{xx}, \epsilon_{yy}$ and $\epsilon_{\perp} = \epsilon_{zz}$. Eq. (2.5) can be simplified to the following

$$\begin{pmatrix} \sigma_{xx} \\ \sigma_{yy} \\ \sigma_{zz} \end{pmatrix} = \begin{pmatrix} (C_{11} + C_{12})\epsilon_{\parallel} + C_{13}\epsilon_{\perp} \\ (C_{12} + C_{11})\epsilon_{\parallel} + C_{13}\epsilon_{\perp} \\ 2C_{13}\epsilon_{\parallel} + C_{33}\epsilon_{\perp} \end{pmatrix} , \tag{2.6}$$

The first two elements of the column vector indicate that the stress in *C*-plane oriented films is isotropic in the growth plane such that $\sigma_{xx} = \sigma_{yy} = \sigma_{\parallel}$ and $\sigma_{zz} = \sigma_{\perp}$. As the growth direction is along the *c* axis, the film is free to expand or contract along this direction, leading to $\sigma_{\perp} = 0$. Therefore,

$$\frac{\epsilon_{\perp}}{\epsilon_{\parallel}} = -2\frac{C_{13}}{C_{33}} . \tag{2.7}$$

Eq. (2.7) is Poisson's relation. The film will expand along the growth direction, if the strain is compressive in nature, and will contract along the growth direction, if the strain is tensile. The in-plane stress $\sigma_{\parallel}$ and the in-plane strain $\epsilon_{\parallel}$ are related by Young's modulus Y in the plane. Using Eq. (2.7) in $\sigma_{\parallel} = (C_{11} + C_{12})\epsilon_{\parallel} + C_{13}\epsilon_{\perp}$, we obtain:

$$\frac{\sigma_{\parallel}}{\epsilon_{\parallel}} = Y = C_{11} + C_{12} - 2\frac{C_{13}^2}{C_{33}} . \tag{2.8}$$

***M* plane: Growth along** $[1\bar{1}00]$

In this case, the unique c axis for the wurtzite crystal structure, lies in the growth plane, and the growth direction is perpendicular to the c axis and parallel to the y axis, $[1\bar{1}00]$ (cf. Fig. 2.1). In contrast to the hexagonal symmetry for substrates used in C-plane GaN growth, M-plane GaN is generally grown on γ-$LiAlO_2$ substrates, which have a tetragonal symmetry. In the case of M-plane films, the strain state is anisotropic, i.e., $\epsilon_{xx} \neq \epsilon_{zz}$, because the lattice constants and the thermal expansion coefficients are different for the film and the substrate along the z- as well as the x-direction. Therefore, Eq. (2.4) takes the following form:

$$\begin{pmatrix} \sigma_{xx} \\ \sigma_{yy} \\ \sigma_{zz} \end{pmatrix} = \begin{pmatrix} C_{11}\epsilon_{xx} + C_{12}\epsilon_{yy} + C_{13}\epsilon_{zz} \\ C_{12}\epsilon_{xx} + C_{11}\epsilon_{yy} + C_{13}\epsilon_{zz} \\ C_{13}(\epsilon_{xx} + \epsilon_{yy}) + C_{33}\epsilon_{zz} \end{pmatrix} , \tag{2.9}$$

As the growth direction is along the y axis, the film is free to expand or contract along this direction, i.e., $\sigma_{yy} = 0$, which leads to

$$\epsilon_{yy} = -\frac{C_{12}\epsilon_{xx} + C_{13}\epsilon_{zz}}{C_{11}} . \tag{2.10}$$

***A* plane: Growth along** $[11\bar{2}0]$

For A-plane GaN films, the growth direction is along the $[11\bar{2}0]$ direction which, according to our nomenclature, is parallel to the x axis. The strain in this case is also anisotropic, i.e., $\epsilon_{yy} \neq \epsilon_{zz}$, because the films are grown on R-plane sapphire. The R plane of sapphire is an inclined plane and has different lattice constants along two normal direction as opposed to C-plane of sapphire, which has a hexagonal symmetry. In this case, the film is free to expand along the x-direction, i.e., $\sigma_{xx} = 0$, and

$$\epsilon_{xx} = -\frac{C_{12}\epsilon_{yy} + C_{13}\epsilon_{zz}}{C_{11}} . \tag{2.11}$$

This equation is same as Eq. (2.10) except for the exchange of x and y. This symmetry occurs because the matrix in Eq. (2.4), which defines the relation between the stress and strain, is symmetric in x and y. Furthermore, as explained above, one can always find a pair of M and A planes, which are orthogonal to each other, and thus we can exchange one by another by replacing x with y.

Lattice parameters and thermal characteristics of various substrates

With the absence of a native substrate for GaN, it is mostly grown on different substrates such as SiC, γ-$LiAlO_2$, or sapphire. These substrates have different lattice constants and thermal expansion coefficients than GaN, which inevitably leads to strain in the epitaxially grown films.

Table 2.1 shows the lattice parameters of the various substrates used for the epitaxial growth of GaN. The lattice mismatch is different in both directions, if the substrate does not have a hexagonal crystal symmetry, as is the case for GaN grown on γ-$LiAlO_2$. These values are evaluated by considering the lattice mismatch between the substrate

Table 2.1: Lattice parameters of the substrate materials used for nitride growth and their lattice mismatch with GaN. The lattice parameters of various substrates, most of which are having hexagonal crystal structure, are shown in column 3 for a and in column 4 for c. The second column denotes the crystal symmetry where h denotes Hexagonal and t denotes Tetragonal. The matched direction of the substrate with respect to GaN is stated in column 5 and 6 (**Matched direction**) for both $\parallel a$ and $\parallel c$. The lattice mismatch evaluated with the values given in columns (a) and (c) is shown in the last column. The matched direction of GaN with the various substrates is also shown. $*$ denotes that the strain is anisotropic for GaN on γ-$LiAlO_2$. The lattice constants are taken from Ref. [44] for GaN, AlN and 6H-SiC, from Ref. [45] for γ-$LiAlO_2$ and from Ref. [46] for ZnO and Sapphire.

Crystal		a [Å]	c [Å]	Matched direction $\parallel a$	Matched direction $\parallel c$	Mismatch
GaN	h	3.1876	5.1846	$-$	$-$	0%
AlN	h	3.112	4.982	$a_{GaN} \parallel a_{AlN}$	$c_{GaN} \parallel c_{AlN}$	-2.7%
Sapphire	h	4.758	12.991	$a_{GaN} \parallel a_{Sapphire}/\sqrt{3}$	—	49%(13%)
6H-SiC	h	3.0812	15.102	$a_{GaN} \parallel a_{SiC}$	$c_{GaN} \parallel c_{SiC}$	-3.1%
ZnO	h	3.250	5.207	$a_{GaN} \parallel a_{ZnO}$	$c_{GaN} \parallel c_{ZnO}$	2.1 %
γ-$LiAlO_2$	t	5.1687	6.2679	$a_{GaN} \parallel c_{LiAlO_2}/2$	$c_{GaN} \parallel a_{LiAlO_2}$	-0.3% $\parallel c$; -1.7%$\perp c^*$

and the epilayer at room temperature. The contribution due to the mismatch in the thermal expansion coefficients, which will also be substantial due to high growth temperatures, is not included. Therefore, the total strain may be different from the values calculated from lattice constants alone. Let a_l and c_l be the relaxed lattice constants for the layer, a_l^s and c_l^s be the strained lattice constants for the layer and a_s and c_s be the substrate lattice constants. The lattice mismatch between the film and the substrate will be $\Delta a = (a_l - a_s)/a_l$ along the a direction and similarly $\Delta c = (c_l - c_s)/c_l$ along the c direction. The strain is anisotropic for GaN films grown on γ-$LiAlO_2$ or R-plane sapphire because the lattice constants in the two in-plane directions for the layer are different from the ones of the substrate.

2.2.2 Measurement of the out-of-plane strain

The determination of the strain state and the composition of group-III nitrides relies almost exclusively on x-ray diffraction (XRD). A direct kinematical analysis of the results, i.e., calculating the lattice constants from the measured angular separation between the reflections of the substrate and the layer, should in principle lead to an estimation of the strain components. For a family of planes, $\{h\,k\,i\,l\}$, in a wurtzite crystal structure, the distance between parallel planes is given by:

$$\frac{1}{d^2} = \frac{4(h^2 + k^2 + hk)}{3a^2} + \frac{l^2}{c^2}\,, \tag{2.12}$$

where a and c are the lattice constant along the $[1\bar{1}00]$ and [0001] directions, respectively. d is the distance between two nearest-neighbor parallel planes determined by $\{h\,k\,i\,l\}$. For the case of a family of M-plane oriented films, where the growth plane is $\{1\bar{1}00\}$, the distance d is given by $d = \frac{\sqrt{3}a}{2}$. Similarly for a $\{0001\}$ family of planes, i.e., C-plane oriented films, the distance $d = c$, while for $\{11\bar{2}0\}$, i.e., A-plane oriented films, $d = \frac{a}{2}$.

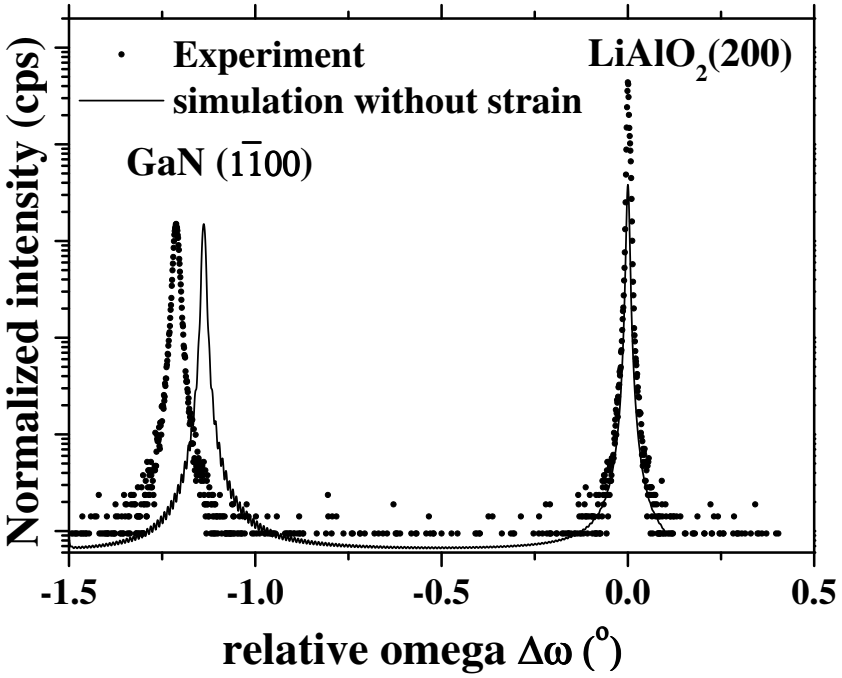

Figure 2.2: A typical symmetric, triple-crystal $\omega-2\theta$ scan for a M-plane sample grown by PAMBE on γ -$LiAlO_2$ is shown. The substrate peak, labelled $LiAlO_2$, is taken as the reference. A simulation based on dynamical diffraction theory is also plotted to identify the peak position for an unstrained M-plane GaN film of same thickness. The peak position corresponding to the layer is shifted with respect to unstrained GaN thin film showing strain.

The strained lattice constant, a_l^s, of the wurtzite GaN can be determined using the symmetric ω-2θ XRD scan, and the value of the residual strain along the various axes is estimated to be:
$\epsilon_{zz} = (c_l^s - c_l)/c_l$ for the case of C-plane GaN.
$\epsilon_{yy} = (a_l^s - a_l)/a_l$ for the case of M-plane GaN.
$\epsilon_{xx} = (a_l^s - a_l)/a_l$ for the case of A-plane GaN.

It is not possible to measure the in-plane strain components using the standard ω-2θ measurement for M-plane GaN grown on γ-$LiAlO_2$, without resorting to grazing incidence XRD because of the absence of subsequent substrate peaks due to different crystal symmetry of the substrate.

Figure 2.2 shows a typical symmetric ω-2θ x-ray scan for an M-plane GaN film grown on $LiAlO_2$. We follow the same procedure as employed in Refs. [44] and [47] to determine the structural parameters of the GaN films. Note that, in this chapter, the data of Fig. 2.2 is used for qualitative discussion in order to show the strain in the film. A more detailed description of the measurement setup and the calculation of the values of the out-of-plane strain is given in Chapter 3. We can see a diffraction peak from the substrate labelled as $LiAlO_2$ (200), which is taken as the reference. It also shows the peak from the M-plane GaN film, which is labelled GaN (1$\bar{1}$00). The thick substrate, which is assumed to be unstrained, is taken as the reference, and its peak position is taken to be zero. The out-of-plane strain can be determined by the help of simulations, which are based on dynamical diffraction theory [44]. The simulations

were performed assuming ideal, defect-free crystals and perfect interfaces for a film of the same thickness, but with no in-plane strain. The relative shift in the peak position between the experimentally measured curve and the one simulated signifies that the film is under strain, which changes the out-of-plane lattice constant, a_l^s. The lattice constant of the strained layer is higher than the one for the unstrained layer so that the film, as expected, exhibits out-of-plane dilation (cf. Table 2.1). The lattice constant and the out-of-plane strain are measured at room temperature. The built-in strain is expected to increase with decreasing temperature due to the difference in the thermal expansion coefficients between the GaN epilayer and the substrate material.

2.3 Modification of the band structure due to biaxial strain

The optical and the electronic transport properties of a semiconductor are mostly governed by the electronic band structure in the vicinity of the valence-band maxima and conduction-band minima. For group-III-nitride semiconductors, sp^3 hybridization, causes their conduction band to be determined from *s*-like antibonding and their valence bands from *p*-like bonding orbitals. In the language of elementary group theory, including spin, the two-fold conduction band transforms like Γ_7^c, while the symmetry of the 3 two-fold valence bands is Γ_9^v, Γ_7^v, and Γ_7^v. The corresponding band-to-band transitions can be distinguished by appropriate selection rules: the transition between the Γ_9^v valence band and the Γ_7^c conduction band is forbidden in the Π configuration, i.e., when the electric field of the incoming light is *z* polarized. In the analysis of conventional zincblende semiconductors, one assumes a parabolic dispersion for the conduction band, and 4×4 and/or 6×6 Bir-Pikus Hamiltonians are used to describe the three uppermost valence bands. When treating the valence bands together with the conduction band, one makes use of the 8×8 Kane Hamiltonian. [48] The Kane and the Bir-Pikus Hamiltonians are constructed for the cubic crystal system. Various groups have made effort to write an equivalent Hamiltonian for GaN using quasi-cubic symmetry. The work by Suzuki [49] and references therein describe the validity and the quasi-cubic approximations one has to make , while writing a similar Hamiltonian for a semiconductor having a wurtzite crystal structure as for the zincblende crystal structure.

As discussed above, the films are grown using heteroepitaxy and are therefore strained. Consequently, it is important to calculate the band structure as a function of strain in the films. The strain significantly changes the valence band (VB) structure, especially in the case of *M*-plane GaN, where the strain is anisotropic and larger than for GaN grown along other orientations.

Starting with the Schrödinger equation, let us formulate the $\boldsymbol{k}\cdot\boldsymbol{p}$ perturbation method:

$$\mathbf{H}\Psi_{n\mathbf{K}}(\mathbf{r}) = (\frac{\mathbf{p}^2}{2m_0} + V(\mathbf{r}) + \mathbf{H}_{so})\mathbf{\Psi}_{n\mathbf{K}}(r) = E_n(\mathbf{K})\mathbf{\Psi}_{n\mathbf{K}}(r)\ , \tag{2.13}$$

where $V(\mathbf{r})$ is the crystal potential with the periodicity of the lattice, $\mathbf{K}$ is the wavevector, m_0 is the free electron mass, $\mathbf{H}_{so}$ stands for the spin-orbit interaction and the wavefunctions $\mathbf{\Psi}_{n\mathbf{K}}(\mathbf{r})$ satisfying Eq. (2.13) are:

$$\mathbf{\Psi}_{n\mathbf{K}}(\mathbf{r}) = \exp^{i\mathbf{K}\cdot\mathbf{r}} \mathbf{u}_{n\mathbf{K}}(\mathbf{r}) \ , \tag{2.14}$$

where $\mathbf{u}_{n\mathbf{K}}(\mathbf{r})$ is the Bloch function with $\mathbf{u}_{n\mathbf{K}}(\mathbf{r+R}) = \mathbf{u}_{n\mathbf{K}}(\mathbf{r})$, and $\mathbf{R}$ is the translation vector of the Bravais lattice and n is the band index. $\mathbf{H}_{so}$ is of the form

$$\mathbf{H}_{so} = \frac{\hbar}{4m_0^2c^2}(\boldsymbol{\nabla} V \times \mathbf{p}) \cdot \boldsymbol{\sigma} = \frac{\hbar}{4m_0^2c^2}(\boldsymbol{\sigma} \times \boldsymbol{\nabla} V) \cdot \mathbf{p} \ , \tag{2.15}$$

where σ_i (i = x,y,z) denote the Pauli spin matrices. Substituting the Bloch function into the Schrödinger equation, Eq. (2.13), we obtain

$$(\mathbf{H}_0 + \mathbf{H}_1 + \mathbf{H}_{so})\mathbf{u}_{n\mathbf{K}}(\mathbf{r}) = E_n(\mathbf{K})\mathbf{u}_{n\mathbf{K}}(\mathbf{r}) \ , \tag{2.16}$$

where

$$\mathbf{H}_0 = \frac{\mathbf{p}^2}{2m_0} + \mathbf{V}(\mathbf{r}) \ , \tag{2.17}$$

$$\mathbf{H}_1 = \frac{\hbar}{m_0}\boldsymbol{K} \cdot \boldsymbol{p} \ , \tag{2.18}$$

$$\mathbf{H}_{so} = \begin{cases} \mathbf{H}_{so}^0 = \frac{\hbar}{4m_0^2c^2}(\boldsymbol{\nabla} V \times \mathbf{p}) \cdot \boldsymbol{\sigma} \\ \mathbf{H}_{so}^1 = \frac{\hbar}{4m_0^2c^2}(\boldsymbol{\nabla} V \times \mathbf{K}) \cdot \boldsymbol{\sigma} \end{cases} , \tag{2.19}$$

where $\mathbf{H}_{so}^0$ stands for the K-independent or the atomic-like spin-orbit interaction and $\mathbf{H}_{so}^1$ for the K-dependent spin-orbit interaction. The essence of the $\boldsymbol{k}\cdot\boldsymbol{p}$ method is to treat $\mathbf{H}_{so}^0$ and $\mathbf{H}_{so}^1$ as small perturbations. For simplicity, $\mathbf{H}_{so}^1$ is completely neglected because its effect is small.

2.3.1 Bir-Pikus approach for $k \cdot p$ perturbation in wurtzite semiconductor

In treating the six valence bands together with the two conduction bands on equal footing, one makes use of the 8×8 Bir-Pikus Hamiltonian,[50] which is given by

$$\begin{pmatrix} H_{cc}^{'} & H_{cv}^{'} \\ H_{cv}^{'\dagger} & H_{vv}^{'} \end{pmatrix} , \tag{2.20}$$

with the basis function being $[u_1^c, u_2^c, u_1^v, u_2^v, u_3^v, u_4^v, u_5^v, u_6^v]$

$$
\begin{aligned}
u_1^c &= |S,\uparrow\rangle\ , \\
u_2^c &= |S,\downarrow\rangle\ , \\
u_1^v &= \frac{1}{\sqrt{2}}|X+iY,\uparrow\rangle\ , \\
u_2^v &= \frac{1}{\sqrt{2}}|X+iY,\downarrow\rangle\ , \\
u_3^v &= |Z,\uparrow\rangle\ , \\
u_4^v &= |Z,\downarrow\rangle\ , \\
u_5^v &= \frac{1}{\sqrt{2}}|X-iY,\uparrow\rangle\ , \\
u_6^v &= \frac{1}{\sqrt{2}}|X-iY,\downarrow\rangle\ ,
\end{aligned}
\tag{2.21}
$$

$|\uparrow\rangle$ and $|\downarrow\rangle$ are the spin functions corresponding to spin-up and spin-down states, respectively. $|X\rangle$, $|Y\rangle$, and $|Z\rangle$ are the Bloch functions at the Γ-point (k=0) transforming like x, y, and z, respectively. $H_{cc}^{'}$ and $H_{vv}^{'}$ are 2×2 and 6×6 matrices for the conduction-band and valence-band states, respectively without any interaction between them. The interaction between the conduction-band and valence-band states is described by $H_{cv}^{'}$. One can treat this interaction within second order perturbation theory due to the large band gap of GaN. Then, the 8×8 Hamiltonian splits into a 2×2 Hamiltonian H_{cc} for the conduction band (CB) and a 6×6 Hamiltonian H_{vv} for the VB, respectively. Note that the matrices H_{vv} and H_{cc} are different from $H_{vv}^{'}$ and $H_{cc}^{'}$. This difference lies in the value of the masses and the Luttinger-like parameters defined below. For a strained semiconductor, the Hamiltonian is further modified giving rise to the following matrix:[49]

$$
H_{cc} = \begin{pmatrix} E_c & 0 \\ 0 & E_c \end{pmatrix}\ , \tag{2.22}
$$

$$
H_{vv} = \begin{pmatrix}
F & 0 & -H^* & 0 & \kappa^* & 0 \\
0 & G & \Delta & -H^* & 0 & \kappa^* \\
-H & \Delta & \Lambda & 0 & I^* & 0 \\
0 & -H & 0 & \Lambda & \Delta & I^* \\
\kappa & 0 & I & \Delta & G & 0 \\
0 & \kappa & 0 & I & 0 & F
\end{pmatrix}\ , \tag{2.23}
$$

where

$$
E^c = \alpha_{\parallel}\epsilon_{zz} + \alpha_{\perp}(\epsilon_{xx}+\epsilon_{yy}) + \frac{\hbar^2 K_z^2}{2m_{\parallel}^e} + \frac{\hbar^2 K_{\perp}^2}{2m_{\perp}^e}, \tag{2.24}
$$

$$
F = \Delta_1 + \Delta_2 + \lambda + \theta, \tag{2.25}
$$

$$
G = \Delta_1 - \Delta_2 + \lambda + \theta, \tag{2.26}
$$

$$H = i(A_6 K_z K_+ + A_7 K_+ + D_6 \epsilon_{z+}), \tag{2.27}$$

$$I = i(A_6 K_z K_+ - A_7 K_+ + D_6 \epsilon_{z+}), \tag{2.28}$$

$$\kappa = A_5 K_+^2 + D_5 \epsilon_+; \Delta = \sqrt{2}\Delta_3, \tag{2.29}$$

$$\lambda = A_1 K_z^2 + A_2 K_\perp^2 + D_1 \epsilon_{zz} + D_2(\epsilon_{xx} + \epsilon_{yy}), \tag{2.30}$$

$$\theta = A_3 K_z^2 + A_4 K_\perp^2 + D_3 \epsilon_{zz} + D_4(\epsilon_{xx} + \epsilon_{yy}), \tag{2.31}$$

$$\epsilon_+ = \epsilon_{xx} - \epsilon_{yy} + 2i\epsilon_{xy}; \epsilon_{z+} = \epsilon_{xz} + i\epsilon_{yz}, \tag{2.32}$$

$$K_+ = K_x + iK_y, K_\perp^2 = K_x^2 + K_y^2. \tag{2.33}$$

The parameters D_i (*i=1 to 6*) denote the deformation potentials for the valence bands, and A_j (*j=1 to 7*) are equivalent to the Luttinger parameters and determine the hole effective masses. α and m^e denote the conduction band deformation potential and electron effective mass, respectively. $m_\parallel$ and $m_\perp$ are not the electron effective masses but are the sum of the free electron mass. [49] ϵ_{lm} and K_l $(l, m = x, y, z)$ are the strain and wavevector components. Δ_1 is the crystal-field energy parameter and is equal to the crystal-field splitting, while Δ_2 and Δ_3 are the spin-orbit energy parameters. In the quasi-cubic approximation, we have $\Delta_2 = \Delta_3$, and the spin-orbit splitting is given by $3\Delta_2 = 3\Delta_3$. The eigenvalues of the above matrix for the VB yield three distinct energies, which we denote as E_j^v. The difference between H_{vv} (H_{cc}) and H'_{vv} (H'_{cc}) lies in $m_\parallel$, $m_\perp$ and Luttinger-like parameters A_j.

Six distinct valence band deformation potentials, in addition to the strain tensor and the overall hydrostatic deformation potential, are necessary to describe the band structure under strain. Numerous sets of valence band deformation potentials have been derived from both first principle calculations and fits to experimental data. [51, 52, 53, 54, 55, 56, 57, 58, 59, 60, 61] To determine the deformation potentials D_1, D_2, and D_5, different approximations have been taken.[56, 62] A widely quoted work by Suzuki *et al.* [51], who use the first-principle calculations to determine the band-structure, suggest $D_1 = -15.35$ eV, $D_2 = -12.32$ eV, $D_3 = 3.03$ eV, $D_4 = -1.52$ eV and $D_5 = -2.05$ eV. The value for D_6 is not determined.

Shikanai *et al.* [63] found out that the experimentally determined value for D_3^{exp} and D_4^{exp} differ from the theoretically estimated values D_3^{theory} and D_4^{theory} by Suzuki *et al.* [51] given above. Both ratios $D_3^{\text{exp}}/D_3^{\text{theory}}$ and $D_4^{exp}/D_4^{\text{theory}}$ have a value of about 2.9. A method put forward by Ghosh *et al.* [55] was to multiply all values suggested by Suzuki *et al.*, [51, 58, 59] achieved by theoretical first principle calculations, with a constant value of about 2.7. In this way, the quasi-cubic approximation still continues to be satisfied, as for the theoretically estimated values. The deformation potential

values thus obtained are $\alpha_\perp = \alpha_\parallel = \alpha = -44.5$ eV and $D_1 = -41.4$ eV, $D_2 = -33.3$ eV, $D_3 = 8.2$ eV, $D_4 = -4.1$ eV and $D_5 = -4.7$ eV. There is a considerable discrepancy in the deformation potentials reported by various groups, and further work is needed to determine which results are most accurate. However, we will use the values determined by Ghosh *et al.* [55] for the deformation potentials to calculate the band structure of GaN.

Similarly, elastic constants for wurtzite GaN have been obtained from a number of experiments [61, 64, 65, 66, 67] and calculations. [67, 68, 69, 70, 71, 72] A widely cited work is by Polian *et al.* [64], who measured the elastic constants using Brillouin scattering. They obtained the following values: C_{11}=390 GPa, C_{12}=145 GPa, C_{13}=106 GPa, C_{33}=398 GPa, and C_{44}=105 GPa. However, the experiments done by various other groups suggest values, which disagree to a considerable extent among each other. Nonetheless, we will use the values given by Polian and coworkers.

2.3.2 Strain modified band structure for *C*-, *M*- and *A*-plane GaN

We now discuss the transition energies for the free excitons associated with the top three valence bands in GaN. We calculate the strain dependence of the interband transition energies at the fundamental band gap of GaN and the components of the oscillator strength using the $\mathbf{k}\cdot\mathbf{p}$ perturbation approach. As the various planes of GaN are discussed, the appropriate nomenclature is used to distinguish the various excitonic transitions for different planes Using the approach outlined by Ghosh *et al.* [55], we can calculate the transition energies and its dependence on the in-plane strain. Similarly, the dependence of the values of the oscillator strength on the in-plane strain is calculated. For these calculations, the band gap of GaN was chosen such that the *A*-exciton transition energy in unstrained GaN is 3.479 eV in the low-temperature limit as observed in experiments on free standing GaN. [73] The components of the oscillator strength for the transitions, which determine the polarization selection rules, are obtained from the oscillator strength of the type $f_{i\beta} = |\langle\psi^{CB}|p_\beta|\psi_i^{VB}\rangle|^2$ where β can be x, y or z for light polarized along these directions and i = 1, 2 or 3 for the top three transitions. Here $|\psi^{CB}\rangle = |S\rangle$ and $|\psi_i^{VB}\rangle = a_{ix}|X\rangle + a_{iy}|Y\rangle + a_{iz}|Z\rangle$ represent the orbital part of the conduction band and valence band basis functions, respectively. The coefficient $a_{i\beta}$ (i = 1,2,3) is obtained by determining the eigenvectors of H^{vv} defined in Eq. (2.23). The relative values of the oscillator strengths $|\langle S|p_x|X\rangle|^2$, $|\langle S|p_y|Y\rangle|^2$, and $|\langle S|p_z|Z\rangle|^2$ are normalized to the same value in accordance to Ref. [74]. Each element $f_{i\beta}$ with β = x, y, or z denotes the transition probability from the valence band to the conduction band, when the incoming light is polarized along the x, y or z direction, respectively. For more details on the calculation and the various parameters, see the work by Ghosh *et al.*[55] and references therein. The $f_{i\beta}$ obey the following sum rules:

$$\begin{aligned} f_{ix} + f_{iy} + f_{iz} &= 1; \quad i = 1, 2, \text{or } 3 \\ f_{1\beta} + f_{2\beta} + f_{3\beta} &= 1; \quad \beta = x, y, \text{or } z \end{aligned} \tag{2.34}$$

The first relation reveals that for each transition denoted by i the sum of the oscillator strength for the x, y , and z polarization is unity. Similarly, the second relation states that for each polarization, the sum of the oscillator strength for all three transition is

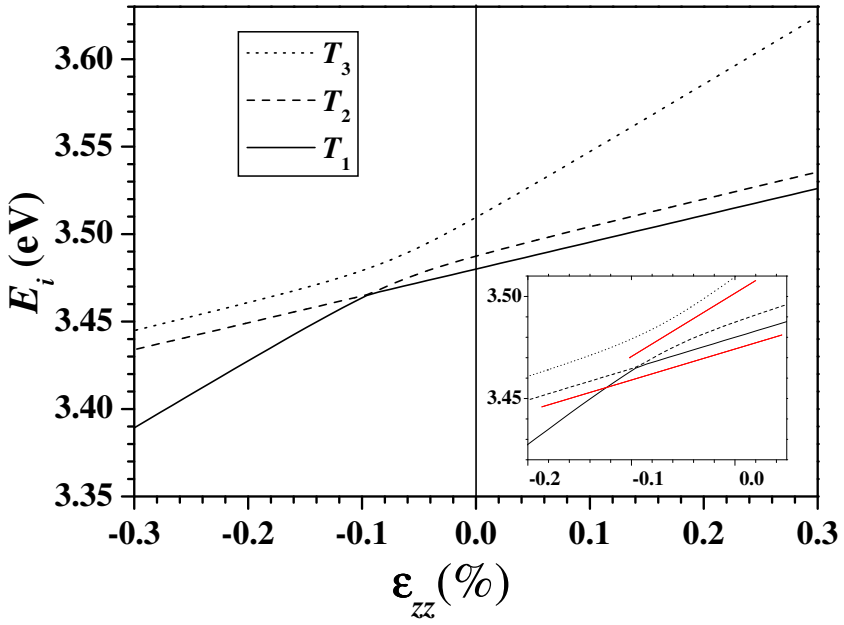

Figure 2.3: Calculated transition energies E_1, E_2, and E_3 as a function of biaxial, isotropic in-plane strain $\epsilon_{xx} = \epsilon_{yy}$ for a *C*-plane GaN film at 5 K. The inset shows the energy range, where a single anticrossing occurs. The dotted lines in the inset are a guide to eye.

unity.

Strain-modified EBS of *C*-plane oriented films: Growth along [0001]

The band structure for unstrained, hexagonal GaN is isotropic in the *C* plane in the vicinity of the Γ point, i.e., **K**=0. Therefore, in unstrained, wurtzite GaN, there are three closely spaced top valence band states at this point, which are Γ_9, Γ_7^{upper} and Γ_7^{lower} and are labeled as heavy hole (HH), light hole (LH) and spin-orbit crystal-field split-off (SCH) hole. The excitons involving electrons in the conduction band and holes in the valence band are referred to as *A*-, *B*-, and *C*-excitons. Since the spin-orbit interaction is very small, given by $3\Delta_3 = 15$ meV [63], both the top two valence-bands are formed of two equivalent *p*-orbital functions, which are $|X\rangle$- and $|Y\rangle$-like, and the energy levels for the two bands are almost degenerate at the Γ point. Only a small spin-orbit and crystal-field interaction exists and splits the energy of these top two valence bands.

For a film under strain, the symmetry of the VB states is significantly modified so that it is no longer possible to describe the transition in terms of *A*-, *B*-, and *C*-excitons. A different nomenclature is therefore adopted, in which the transition involving the top three valence bands are referred to as the T_1, T_2, and T_3 transitions, respectively, in order of increasing energy. For the unstrained case, the T_1, T_2, and T_3 transitions are identical to the *A*-, *B*-, and *C*-transitions. As mentioned before, the strain state for *C*-plane GaN is usually isotropic in nature, i.e., $\epsilon_{xx} = \epsilon_{yy}$.

We have calculated the dependence of the values of the transition energies and the oscillator strengths on the in-plane isotropic strain using the $\mathbf{k}\cdot\mathbf{p}$ perturbation approach for the three transitions T_1, T_2, and T_3. It is difficult to determine the individual com-

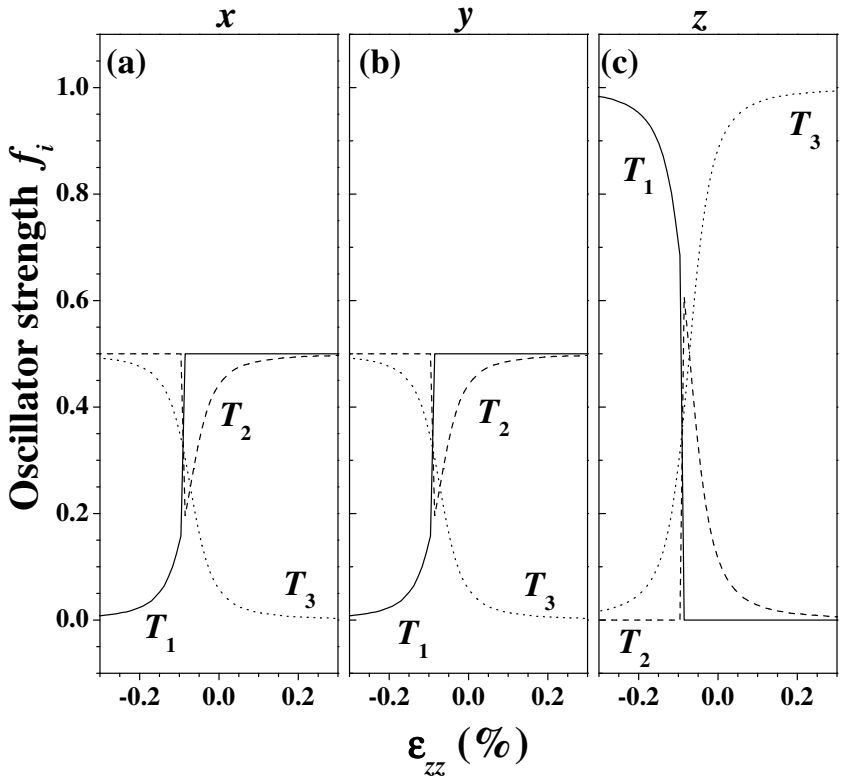

Figure 2.4: Relative (a) x, (b) y and (c) z components of the oscillator strength for the T_1 (solid line), T_2 (dashed line), and T_3 (dotted line) transition as a function of out-of-plane strain ϵ_{zz} calculated for the case, when the in-plane strain is isotropic in nature, i.e., $\epsilon_{xx} = \epsilon_{yy}$, calculated for a C-plane GaN film at 5 K. The oscillator strength shows abrupt change at ϵ_{zz}=-0.096% corresponding to $\epsilon_{xx} = \epsilon_{yy}$ = 0.18 % for all three transitions. At these strain values, the transitions T_1 and T_2 exhibit an anticrossing behavior.

ponents of the in-plane strain values independently. We plot the data versus ϵ_{zz} rather than the biaxial, isotropic in-plane strain, $\epsilon_{xx} = \epsilon_{yy}$, because the value of the lattice constant, c, is directly measured and, thus, the values of ϵ_{zz} are definitely determined by XRD. Since the in-plane strain is isotropic in nature ($\epsilon_{xx} = \epsilon_{yy}$), the out-of-plane can unambiguously determine the in-plane strain using Eq. (2.7). For the more general case, the biaxial, anisotropic in-plane strain values can be determined by comparing the experimentally measured values for the transition energies to the calculated values for a fixed out-of-plane strain ϵ_{zz}. Figure 2.3 shows the variation of the three calculated transition energies as a function of the out-of-plane strain for $|\epsilon_{zz}| \leq 0.3\%$. A negative out-of-plane strain denotes a tensile in-plane strain, while a positive out-of-plane strain signifies a compressive in-plane strain according to Eq. (2.7). The inset of Fig. 2.3 shows that T_1 and T_2 exhibit an anticrossing at ϵ_{zz} = -0.096 %, This anticrossing behavior, which is defined as the exchange of band characteristics. is even more evident in the dependence of the oscillator strength on the out-of-plane strain which we study next.

Figure 2.4 shows the x-, y-, and z- component of the oscillator strength of the three transitions as a function of out-of-plane strain ϵ_{zz}, when the in-plane strain is isotropic in nature, i.e., ϵ_{xx}=ϵ_{yy}. As expected, the results reveal that the oscillator strength is identical for both the x and y polarization. Hence, for each value of isotropic in-plane strain, the x and y polarization contribute equally for each transition. For large out-of-

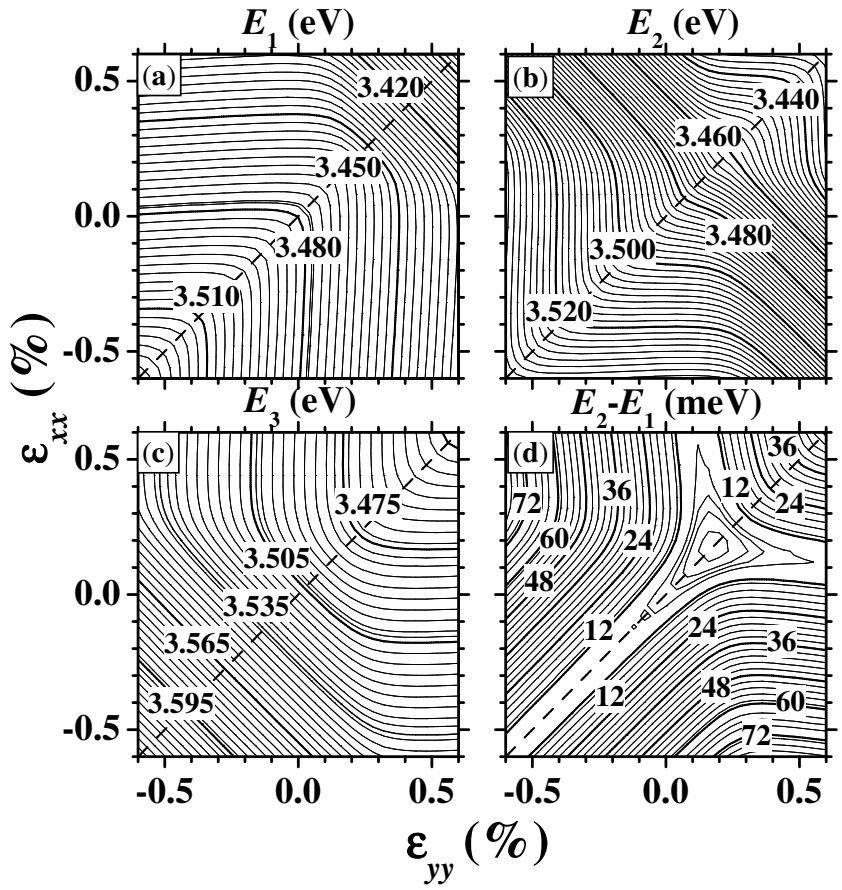

Figure 2.5: The calculated transition energies E_1, E_2, and E_3 as a function of in-plane strain ϵ_{xx} and ϵ_{yy} for a *C*-plane GaN film at 5 K. The energy difference $E_2 - E_1$ is also plotted as a function of in-plane strain. The dashed line denotes the condition for isotropic strain, i.e., $\epsilon_{xx} = \epsilon_{yy}$.

plane tensile (positive) strain, the T_1 transition has an equal contribution from both the x and y polarization while the z contribution is zero. The oscillator strength component is therefore $[\frac{1}{2}, \frac{1}{2}, 0]$. This is similar for the T_2 transition. The T_3 transition, however, is basically fully z polarized ([0,0,1]). For an isotropic out-of-plane compressive (negative) strain, the T_1 transition is almost fully z polarized ([0,0,1]), while the T_2 and T_3 transitions have an equal contribution from the x and y polarization ($[\frac{1}{2}, \frac{1}{2}, 0]$). The sum of the value of the oscillator strength for the three transition together add up to one for each energy transition such that the relations in Eq. (2.34) are satisfied. These polarization properties arise essentially from the symmetry of the wave functions of the strain-modified VB states. The anticrossing behavior is more evident in Fig. 2.4, where at ϵ_{zz}= -0.096%, corresponding to ϵ_{xx}=ϵ_{yy}=0.18%, the transition T_1 (solid line) changes from purely $|Z\rangle$-like [cf. Fig. 2.4(c)] to equally $|X\rangle$- and $|Y\rangle$-like [cf. Figs. 2.4(a) and 2.4(b)]. Furthermore, the transition T_2 (dashed line) changes from equally $|X\rangle$- and $|Y\rangle$-like to Z-like.

It is more interesting to study the more general case, when the in-plane strain is anisotropic and biaxial in nature. The $\mathbf{k}\cdot\mathbf{p}$ calculations are therefore extended to determine the dependence of the transition energies and values of the oscillator strength on anisotropic in-plane strain. Figures 2.5(a)–2.5(c) show the contour plots for the varia-

tion of the transition energies E_1, E_2, and E_3 as a function of the in-plane strain for the range $|\epsilon_{xx}|$ and $|\epsilon_{yy}| \leq 0.6\%$ for the three excitonic transitions T_1, T_2, and T_3, respectively. The solid lines denotes regions of equal energies. The isotropic strain relation ($\epsilon_{xx} = \epsilon_{yy}$) is shown by a dashed line. As can be seen from these figures, the energy can be drastically changed by applying biaxial, anisotropic in-plane strain. Figure 2.5(d) shows the energy difference for the top two transitions calculated as $E_2 - E_1$. The value of transition energies for $\epsilon_{zz} = 0$ is consistent with the result for unstrained *C*-plane GaN, where the separation between the top two valence band, $E_2 - E_1$, is due to spin-orbit and crystal-field coupling only. However, one can increase the separation between the energy of the top two VB states by introducing an anisotropic strain, where $\epsilon_{xx} \neq \epsilon_{yy}$. The anisotropy in strain breaks the crystal symmetry, which is maintained for the case of isotropic *C*-plane strain. As can be seen from Fig. 2.5(d), the values of isotropic strain $\epsilon_{xx} = \epsilon_{yy}$= 0.17% the energy splitting $E_2 - E_1$=0. At this point, the in-plane strain cancels the combined crystal-field and spin-orbit splitting of the top two VBs. We find that for *C*-plane GaN grown on substrates with hexagonal symmetry we cannot separate T_1 and the T_2 states using isotropic strain in the *C* plane within a certain range. Domen *et al.* [62] shows that the energy separation between the top two valence band states remain almost the same as the isotropic strain changes. They concede that the only way to separate the A and B excitons is to distinguish $|X\rangle$ from $|Y\rangle$, i.e., to introduce an anisotropy in the *C*-plane strain. This is true for most of the strain values. However, for strain values $\epsilon_{xx}, \epsilon_{yy} \geq 0.3\%$ one can separate these two states. This is also evident in Fig. 2.3, where the top two energies E_1 and E_2 does separate for $\epsilon_{zz} \leq -0.15\%$.

As mentioned before, the main parameters that determine the polarization anisotropy in the absorption coefficient are the three polarization components ($\beta = x, y, z$) of the oscillator strength $f_{i\beta}$ for each transition T_i, which are given by $|\langle \psi^{CB} | p_\beta | \psi_i^{VB} \rangle|^2$. Figure 2.6 shows the variation of the relative values of the x, y, and z component of the oscillator strength for these three transitions. These are shown by gray scale plots for a *C*-plane strain range of $|\epsilon_{xx}|$ and $|\epsilon_{yy}| \leq 0.6\%$. The relative oscillator strengths are shown on the bar scale below the figure. It has the magnitude of 1, when shown in black, and zero, when shown in white.

The condition of isotropic strain is satisfied by the dashed line. Along this line the oscillator strength for i^{th} transition for the x-component is identical to y-component, i.e., $f_{ix} = f_{iy}$ (i=1,2,3), which means that there exist no in-plane polarization anisotropy in unstrained or isotropically strained *C*-plane GaN. Moreover, as shown in Fig. 2.6, the component of oscillator strength for the y polarization (f_{iy}) can be obtained by taking a mirror image of the component with the x polarization (f_{ix}), about the line of isotropic strain ($\epsilon_{xx} = \epsilon_{yy}$). For strain values away from the isotropic condition, one expects to observe a in-plane polarization anisotropy. Figure 2.6 shows that for certain in-plane anisotropic strain values the T_1 transition becomes purely x-polarized, while the T_2 transition becomes purely y-polarized.

Strain-modified EBS of *M*-plane oriented films: Growth along $[1\bar{1}00]$

The band structure of *M*-plane GaN is identical to *C*-plane GaN, when the film is unstrained. Hence, the top three transitions for *C*-plane, which are the *A*, *B*, and *C*

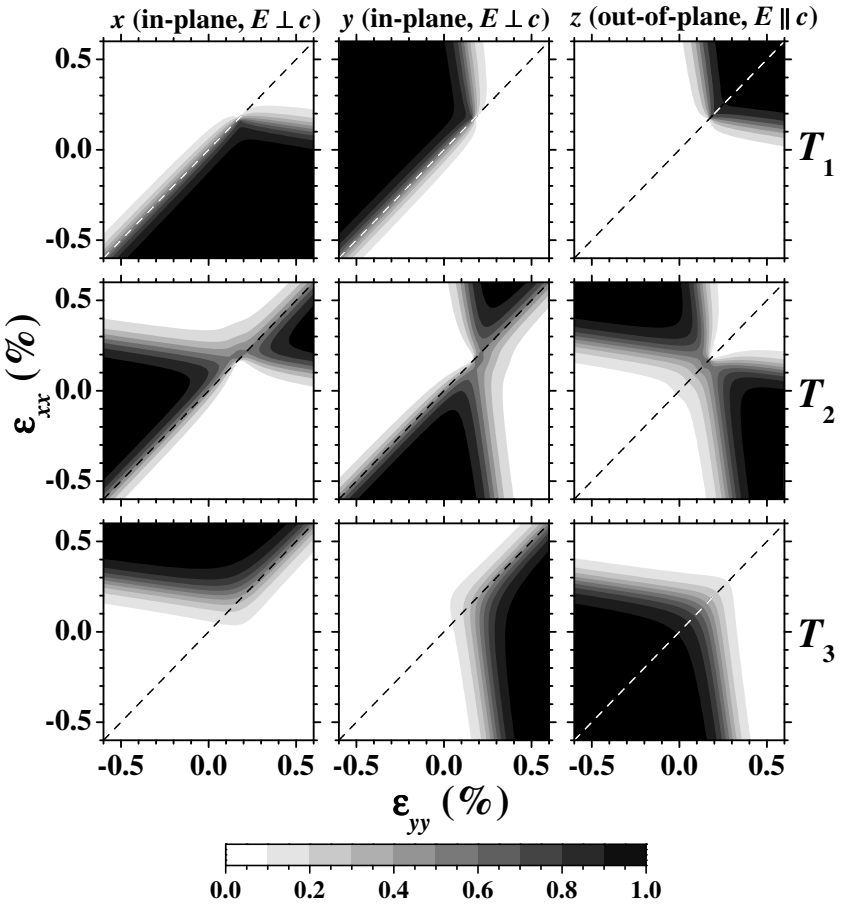

Figure 2.6: Relative x-, y- and z-components of the oscillator strength of the T_1, T_2, and T_3 transitions as a function of in-plane strain ϵ_{xx} and ϵ_{yy} for a C-plane GaN film at 5 K. The dashed line denotes the condition for isotropic strain, i.e., $\epsilon_{xx} = \epsilon_{yy}$.

transitions are equivalent to the T_1, T_2 and T_3 transitions in their wavefunctional character. However, the in-plane symmetry of M-plane films is lower than for C-plane films. Here, according to our nomenclature, the unique c axis lies in the film plane along with the x axis. The out-of-plane direction is thus parallel to $[1\bar{1}00]$, i.e., the y axis. One expects to see an in-plane polarization anisotropy even in the unstrained case because of the lower symmetry of this plane.

We carry out a similar study for M-plane GaN as was done for C-plane GaN in the previous subsection. The functional dependence of the values of the transition energies and the oscillator strengths on the isotropic M-plane strain in M-plane oriented films is significantly different from the case for isotropic C-plane strain in C-plane oriented films. For M-plane GaN films, when the in-plane strain is isotropic and biaxial in nature, we have $\epsilon_{xx} = \epsilon_{zz}$. Since it is difficult to determine the in-plane strain values experimentally for M-plane GaN on γ-$LiAlO_2$, the energy dependence is also calculated as a function of out-of-plane strain ϵ_{yy}. The in-plane strain is related to the out-of-plane strain by Poisson's relation in Eq. (2.10). The in-plane strain is along the x ($[11\bar{2}0]$) direction and along the z ([0001]) direction. Figure 2.7 shows the variation of the three calculated transition energies as a function of the out-of-plane strain for a range of $|\epsilon_{yy}| \leq 0.4\%$. A negative out-of-plane strain denotes a tensile in-plane strain,

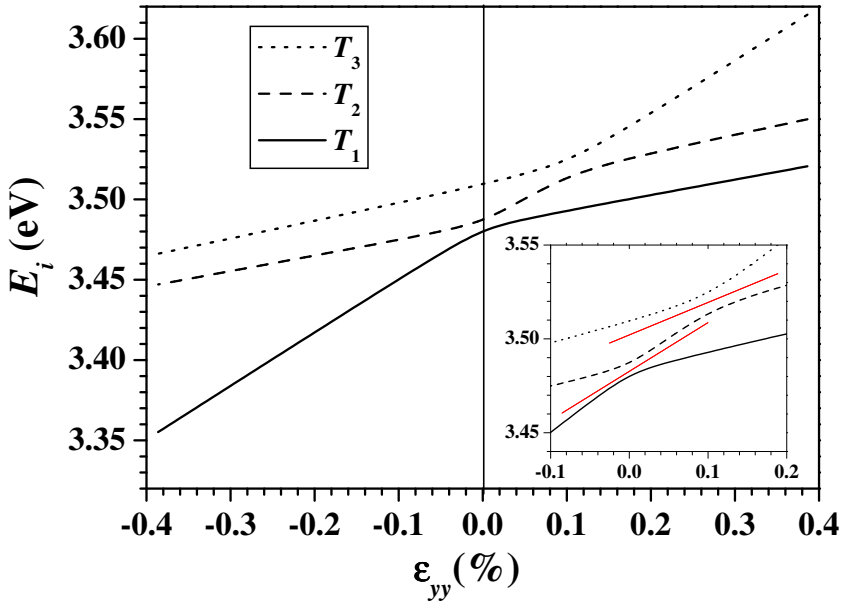

Figure 2.7: Calculated transition energies E_1, E_2, and E_3 as a function of biaxial, isotropic in-plane strain $\epsilon_{xx} = \epsilon_{zz}$ for M-plane GaN film at 5 K. The inset shows the energy range, where two anticrossings occurs. The dotted lines in the inset are a guide to eye.

while a positive out-of-plane strain signifies a compressive in-plane strain, according to Eq. (2.10), which reduces to $\epsilon_{yy} = -(C_{12} + C_{13})\epsilon_{\|}/C_{11}$ with $\epsilon_{xx} = \epsilon_{zz} = \epsilon_{\|}$ for the case of isotropic strain. Biaxial, isotropic in-plane strain in the M plane lifts the symmetry in the x-y plane of the wurtzite crystal structure and changes the original $|X \pm iY\rangle$-like VB states of unstrained GaN to $|X\rangle$-like and $|Y\rangle$-like states. A compressive strain along x, which is negative according to our sign convention, induces a dilation along y so that the energy of the $|X\rangle$-like states is raised, while the energy of the $|Y\rangle$-like states is lowered. The situation is reversed for tensile strain along x, where the energy for the transition between the CB and the $|X\rangle$-like VB is lowered. As shown in Fig. 2.7, an in-plane tensile strain (out-of-plane compressive, negative strain) induces a decrease in the transition energy, while an in-plane compressive strain (out-of-plane tensile, positive strain) induces an increase in the transition energy. At zero in-plane strain values, the transition energies match with the A, B, and C transitions for unstrained C-plane GaN as reported by Torii and coworkers. [73] The dashed line in the inset of Fig. 2.7 reveal two anticrossings (exchange of band characteristics). These are at ϵ_{yy}=0% corresponding to in-plane strain of ϵ_{xx}=ϵ_{zz}=0 and at ϵ_{yy}=+0.096% corresponding to in-plane strain of ϵ_{xx}=ϵ_{zz}=-0.15%. This behavior is different than C-plane GaN, where only one anticrossing is present. The exchange of the band characteristic becomes even more evident in the oscillator strength.

Figures 2.8(a)-2.8(c) show the x-, y-, and z- components of the oscillator strengths for the three transitions as a function of out-of-plane strain ϵ_{yy}. These calculations were performed for the case of isotropic in-plane strain, i.e., $\epsilon_{xx} = \epsilon_{zz}$. These results reveal that for a large out-of-plane tensile (positive) strain the T_1 transition is predominantly x polarized, the T_2 transition z polarized, and the T_3 transition y polarized. For large out-of-plane compressive (negative) strain, the T_1 transition is predominantly y polarized, the T_2 transition x polarized, and the T_3 transition z polarized. These po-

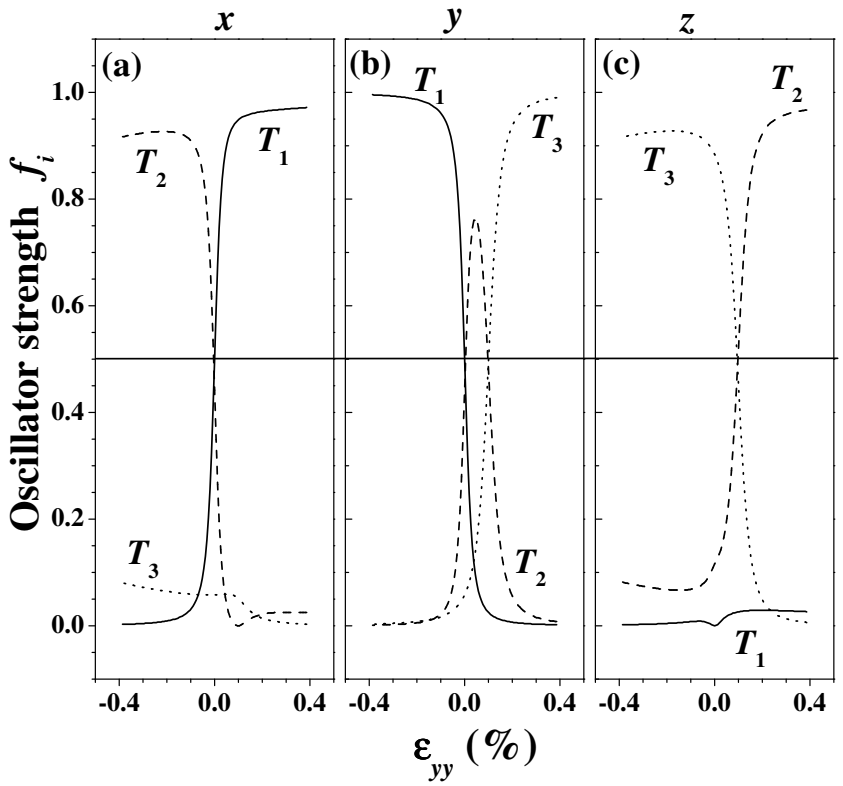

Figure 2.8: Relative (a) x, (b) y and (c) z components of the oscillator strength for the T_1 (solid line), T_2 (dashed line) and T_3 (dotted line) transition as a function of out-of-plane strain ϵ_{yy} calculated for the case when the in-plane strain is isotropic in nature, i.e., $\epsilon_{xx} = \epsilon_{zz}$, for a M-plane GaN film at 5 K. The oscillator strength does not show an abrupt transition as shown for C-plane GaN film shown in Fig. 2.4

larization properties arise essentially from the symmetry of the wave functions of the strain modified VB states. The anticrossing behavior is more evident in Fig. 2.8. For ϵ_{zz}=0%, the transition T_1 (solid line) changes from Y-like to X-like, while T_2 changes from predominantly x-like to partially Y-like with some Z-like character. However, for ϵ_{zz}=+0.0965%, the transition T_3 changes from predominantly Z-like to Y-like, while T_2 changes from partially Y-like to Z-like.

Normally, M-plane GaN films are not relaxed and also do not experience isotropic strain. It is therefore more interesting to study the general case when the strain is anisotropic and biaxial in nature. The $\mathbf{k}\cdot\mathbf{p}$ calculations are extended to determine the dependence of the transition energies and values of the oscillator strength on arbitrary values of individual in-plane strain components. The variation of the E_1, E_2 and E_3 transition energies with in-plane strain is shown by the contour plots in Figs. 2.9(a)-2.9(c) for in-plane strain values $|\epsilon_{xx}|$ and $|\epsilon_{zz}| \leq 0.6\%$. The calculations are done for the low temperature regime. The dependence of the transition energies on strain is significantly different for M-plane GaN than for C-plane GaN as can be seen by comparing Fig. 2.9 with Fig. 2.5. Figure 2.9(d) shows the dependence of the difference in the transition energy $E_2 - E_1$ on the in-plane strain for the transitions T_1 and T_2. The difference is significant also for the case of isotropic in-plane strain as previously discussed. For the M-plane strain values of ϵ_{xx}=0.04% and ϵ_{zz}=$-$0.24%, the separation $E_2 - E_1$ becomes approximately 0. For these in-plane strain values, the strain modified

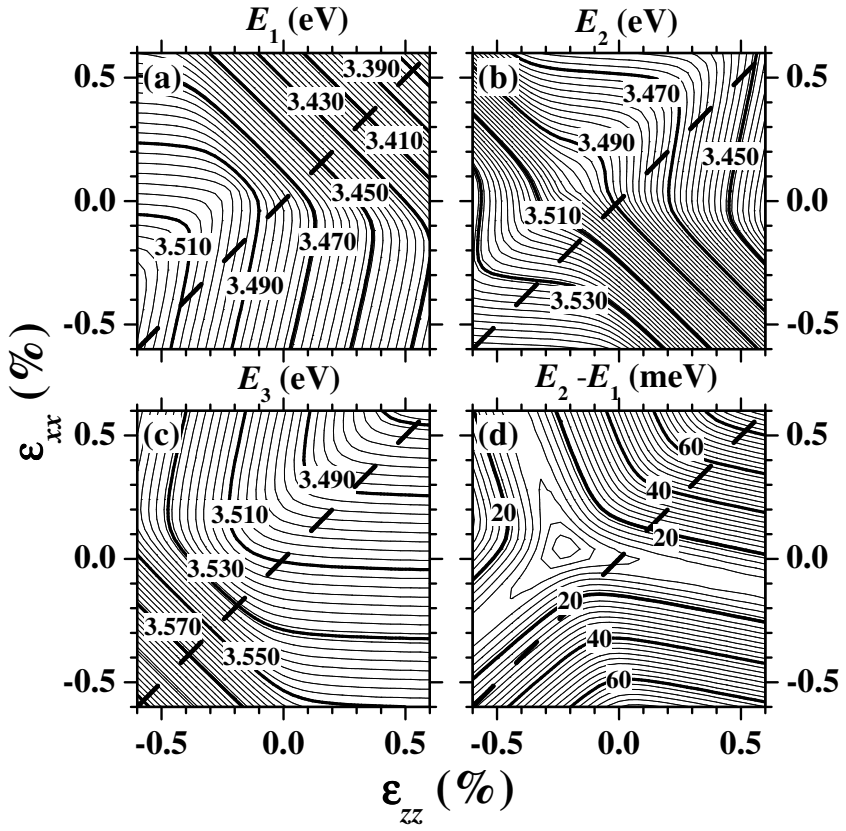

Figure 2.9: The calculated transition energies E_1, E_2 and E_3 as a function of in-plane strain ϵ_{xx} and ϵ_{zz} for a M-plane GaN film at 5 K. The energy difference $E_2 - E_1$ is also plotted as a function of in-plane strain. The dashed line denotes the condition for isotropic strain, i.e., $\epsilon_{xx} = \epsilon_{zz}$.

energies compensate the separation due to the spin-orbit and the crystal-field coupling. These in-plane strain values are significantly different from the case for C plane, where the difference was reduced to zero for isotropic strain values of 0.17%.

The relative values of the x, y, and z components of the oscillator strength $f_{i\beta}$ for the three transitions are shown by the gray scale contour plots in Fig. 2.10 for the M-plane strain in the range $|\epsilon_{xx}|$ and $|\epsilon_{zz}| \leq 0.6$ %. The relative oscillator strength has the magnitude of one when shown in black, and zero, when shown in white. Note that for the range of in-plane strain values ϵ_{xx} and $\epsilon_{zz} \leq -0.2\%$ the T_1, T_2 and T_3 transitions are predominantly x-, z-, and y-polarized, respectively. This region is marked by boxes. This is the region of interest because, as we will see in the course of the discussion, the in-plane strain values for our samples falls into this range. As expected, even for the case of isotropic strain along the line $\epsilon_{xx} = \epsilon_{zz}$, there exist a considerable amount of in-plane polarization anisotropy. However, as was the case for C-plane GaN, the oscillator strength for the T_2 transition f_z cannot be obtained by taking the mirror image of f_x for the T_1 transition about the line $\epsilon_{xx} = \epsilon_{zz}$, i.e., $f_x \neq f_z$ even for isotropic strain. Note that the conditions of Eq. (2.34) are satisfied for the oscillator strength in M-plane GaN, as revealed by Fig. 2.10. Therefore, anisotropic M-plane strain can lead to dominantly x-, y-, or z- polarized transitions. This is because for some range of in-plane strain, the individual components of the oscillator are equal to one suggesting the other components have negligible contributions.

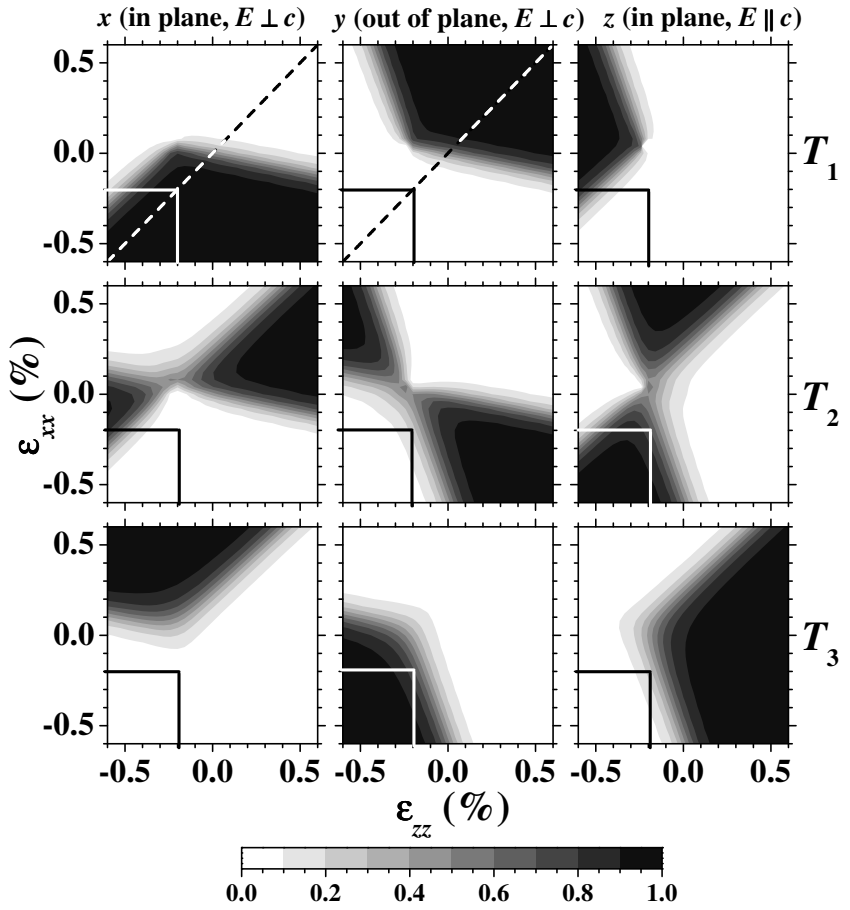

Figure 2.10: Relative x, y and z components of the oscillator strength of the T_1, T_2 and T_3 transitions as a function of in-plane strain ϵ_{xx} and ϵ_{zz} for a M-plane GaN film at 5 K. The dashed line denotes the condition for isotropic strain, i.e., $\epsilon_{xx} = \epsilon_{zz}$. For a certain range of in-plane strain shown by the boxes, the band-structure is so modified that the transitions T_1, T_2 and T_3 transitions are purely x, z and y polarized, respectively.

Strain-modified EBS of *A*-plane oriented films: Growth along $[11\bar{2}0]$

Since Bir-Pikus Hamiltonian for wurtzite GaN under biaxial strain is symmetric with respect to the interchange of x and y, we should be able to switch from M plane to A plane by exchanging x with y and vice versa in the calculations and the results. As was pointed out before, Poisson's relationship in M-plane GaN [cf. Eq. (2.10)] is same as the one for A-plane GaN [Eq. (2.11)] with an interchange of x and y. For M plane, the growth direction is along $y \parallel [1\bar{1}00]$, and x and z are in-plane. For A plane, the growth direction is along $x \parallel [11\bar{2}0]$, and y and z are in-plane. All three growth planes are perpendicular to each other. By extending the calculations for A-plane GaN, one can achieve the similar dependence of the transition energies on the in-plane strain. We performed the energy-band structure calculations for A-plane GaN to determine the transition energies and the values of the oscillator strength as a function of the in-plane strain. They are identical to the case for M-plane GaN films except for the exchange of the x and y axis. We will now show how one can go from the results for the M-plane GaN to A-plane GaN. For example, in Fig. 2.9 showing the variation of the transition

energy for M-plane case, ϵ_{xx} should be changed to ϵ_{yy}. The resulting graph will give the dependence of the transition energies for A-plane GaN as a function of in-plane strain. Similarly, in Fig. 2.10 for the oscillator strength, in addition to changing ϵ_{xx} with ϵ_{yy}, the first column of the gray-scale contour plots denotes the relative y component of the oscillator strength (instead of the x component for M-plane case), while the second column denotes the the relative x component of the oscillator strength (instead of the y component for M-plane case). The z component of the contour plots remains the same. On making the above changes, the resulting graph gives the energies and the oscillator strengths for A-plane GaN.

2.4 Summary

We show that one can separate the energies of the top two valence bands and change the optical response of the system by changing the strain state of the epitaxially grown nonpolar GaN films. This change is more difficult to achieve in case of C-plane GaN film as opposed to nonpolar films because of an inherent reduced symmetry of the wurtzite crystal. The two figures of merit are the separation between the two topmost VB states and the difference in the oscillator strength associated with the transition of these two valence band states with the conduction band. We surmise the results as follows: For unstrained C-plane GaN film, T_1 and T_2 transitions are equally $|X \pm iY\rangle$-like, while T_3 transition is $|Z\rangle$-like For most of the in-plane strain range, it is difficult to separate the energy for the top two VB states by applying isotropic strain and no in-plane polarization anisotropy exist. However, for M and A-plane GaN thin films, even for the case of zero in-plane strain, there is an anisotropy in the wave functional characteristics of the VB states. The anisotropy is further enhanced due to the application of biaxial, anisotropic in-plane strain. For a certain range of in-plane strain values, the band structure is modified in such a way that T_1 becomes $|X\rangle$- and T_2 becomes $|Z\rangle$-like, while the T_3 transition becomes $|Y\rangle$-like. This in-plane polarization anisotropy can be used in device applications, e.g., in polarization sensitive photodetectors (PSPD's) [22] or fast-response, high-contrast optical modulators. The large in-plane strain makes the optical response of M- and A-plane GaN dependent on the in-plane polarization of light. The details of the experimentally determined strain in epitaxially grown films in various orientations will be described in the next chapter.

Chapter 3

Structural properties of GaN thin films

This chapter deals with the x-ray diffraction (XRD) measurement of the various samples grown along different orientations for the accurate determination of the structural parameters. The purpose of the x-ray measurements, in addition to study the phase purity and crystal quality of the samples, is to quantify the strain in the layers as the optical properties studied in the later part of this work rely heavily on the accurate state of the strain in the layers. The out-of-plane strain can be easily determined from the high-resolution symmetric ω-2θ scan. However, we cannot determine the individual components of the in-plane strain, without resorting to grazing-incidence XRD, due to the absence of corresponding substrate peaks while measuring asymmetric ω-2θ scans. Symmetric x-ray ω-2θ scans were taken with a Philips X'Pert PRO triple axis diffractometer using a Cu-K_{α_1} radiation with a wavelength of 0.1540562 nm, a Bartels-type Ge(220) hybrid monochromator and Ge(220) three-crystal analyzer. In additon to the measurement of the strain state, a brief introduction about the synthesis of *C*-plane GaN on GaN template, *M*-plane GaN ($1\bar{1}00$) on γ-$LiAlO_2$, and *A*-plane GaN ($11\bar{2}0$) on *R*-plane sapphire substrates is given. We divide the chapter according to the various orientations (*C*, *M*, and *A* plane of GaN) and discuss their growth and structural properties.

3.1 *C*-plane GaN thin films on a GaN template

The thick GaN single crystals used as the substrate to grow GaN thin films were obtained from a commercial vendor (Samsung). These templates have a nominal thickness of 200 μm. The dislocation density for this template was around $7\times\ 10^6$ cm^{-2}. The growth was carried out in a custom-designed, solid-source three-chamber plasma-assisted molecular-beam-epitaxy (PAMBE) system equipped with a water-cooled rf plasma source (SVT) to provide the atomic nitrogen. The N source operates at plasma power of 300 W with N_2 flow of 1 sccm, yielding a growth rate of 450 nm/h. The base pressure in the growth chamber is held below 10^{-10} Torr by a cryopump, ion-getter pump, and a Ti-sublimation pump. During growth, the chamber is cryopumped and has a pressure of around 8×10^{-6} Torr for a typical N_2 flow of 1 sccm. The growth front is monitored in-situ by reflection high-energy electron diffraction (RHEED) using a 20 kV electron gun. The film used for the following analysis was 1 μm-thick.

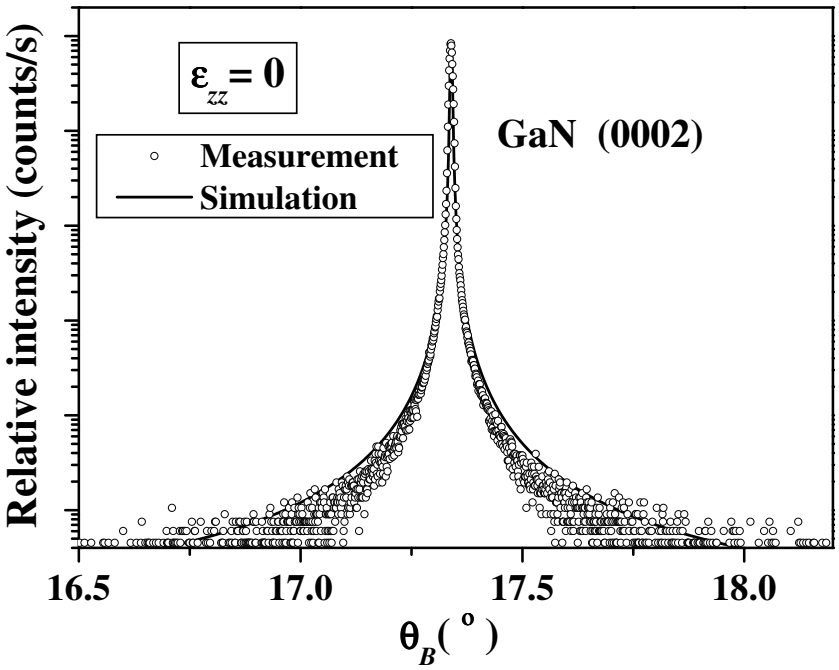

Figure 3.1: Experimental triple-axis ω-2θ scan across the symmetric (0002) reflection of a 1 μm-thick *C*-plane GaN film on a 200 μm-thick GaN substrate. The x-ray diffraction scan reveals that the layer is unstrained.

X-ray diffraction: High-resolution triple-axis XRD was carried out to verify the *C*-plane orientation and out-of-plane strain in the film. Figure 3.1 shows a symmetric XRD profile across the (0002) reflection of the sample grown on a thick GaN substrate. The GaN layer has a (0002) diffraction peak at the Bragg angle of θ_B=17.3°. This peak from the top layer overlaps with the one of the underlying thick substrate. This suggest that there is no angular separation between the thick relaxed substrate and top thin layer signifying that the top layer is unstrained with respect to the GaN substrate. We checked this result by using simulations based on the dynamical diffraction theory [44], which also reveal that the out-of-plane strain is zero.

3.2 *M*-plane GaN thin films on γ-$LiAlO_2$

In order to study the differences between *M*-plane and *C*-plane GaN film, we carried out similar structural measurements for *M*-plane GaN as for *C*-plane GaN. The growth of the *M*-plane layers on γ-$LiAlO_2$(100) substrate was carried out in a custom-designed, solid-source three-chamber MBE system equipped with a water-cooled rf-plasma source (EPI) to provide atomic nitrogen. The N source operates at a plasma power of 250–300 W with N_2 flow of 0.3–0.4 sccm, yielding a growth rate of 300–400 nm/h. The base pressure in the growth chamber is held below 10^{-10} Torr by an ion-getter pump and a Ti-sublimation pump. During growth, the chamber is cryopumped and has a pressure of around 1.5×10^{-5} Torr for a typical N_2 flow of 0.3 sccm. The growth front is monitored in-situ by RHEED using a 20 kV electron gun. The thickness of the *M*-plane GaN layers used in this study was measured by scanning electron microscopy (SEM). The unintentional background doping density was determined to

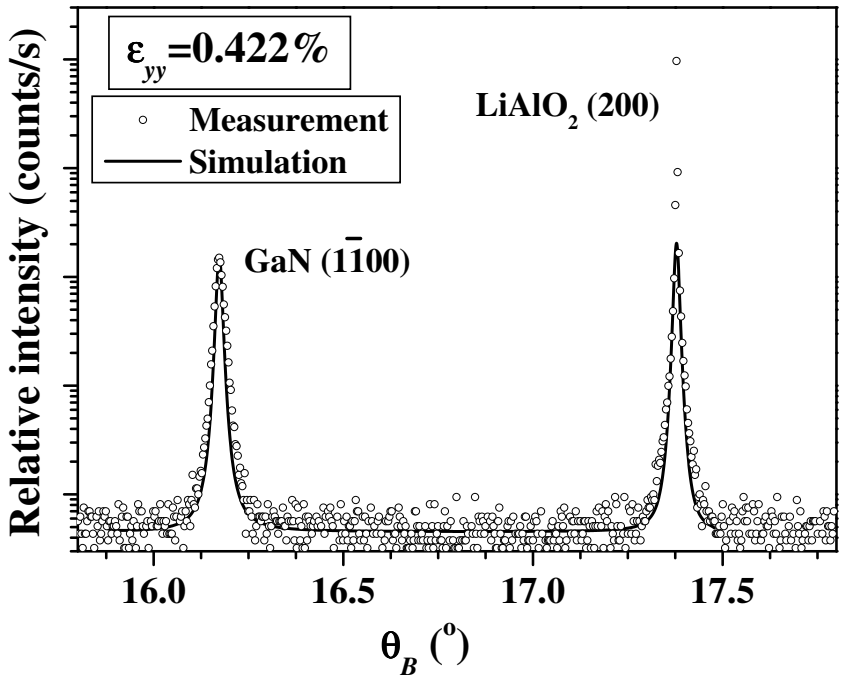

Figure 3.2: Relative ω-2θ symmetric x-ray scan for a 0.7 μm-thick M-plane GaN grown on $LiAlO_2$. The out-of-plane dilation measured by x-ray is ϵ_{yy}= 0.422%. The substrate peak is taken as a reference. The points denote the measurement, while the line denotes the simulation using kinematical theory.

be around 5×10^{17} cm^{-3} at 295 K. Further details of the growth of M-plane GaN on γ-$LiAlO_2$ substrates can be found in the work by Sun et al. [8] The study in Chapter 2 suggests that the polarization anisotropy depends on the in-plane strain in the film and one expects to see a maximum anisotropy in the optical response for a film with higher in-plane strain. It is therefore important to determine the strain as a function of film thickness. For this purpose, we have grown several films with different thicknesses ranging from 50 nm to 1.22 μm.

High-resolution XRD: The phase composition and the strain of the thin M-plane film is measured by utilizing x-ray diffractometry. Figure 3.2 shows the ω-2θ scan for the 700 nm M-plane GaN film grown on γ-$LiAlO_2$. The peaks at 17.3774° and 16.1814° corresponds to the γ-$LiAlO_2$ (200) and GaN ($1\bar{1}00$) reflections, respectively. No peaks related to the GaN (0002) C-phase is detected, which if present should be seen in the vicinity of the γ-$LiAlO_2$(200) diffraction peak, namely at θ= 17.28° (cf. Fig. 3.1)

We employ simulations based on the dynamical diffraction theory and vary the kinematically obtained parameters, until the intensities of the peaks match the experimental values in addition to their position. The value of the angular separation between the layer and the substrate peaks indicates a lattice dilation of ϵ_{yy}=0.422% along the growth direction. This expansion is a consequence of the thermal and/or the lattice mismatch between GaN and γ-$LiAlO_2$. Both factors contribute to a compressive, in-plane strain leading to a dilation along the growth direction. The simulations are shown by the solid line in Fig. 3.2. The width of the GaN($1\bar{1}00$) XRD-reflection peak is larger than theoretically expected one, indicating a certain inhomogeneity of the strain distribution. The epitaxial relationship between the substrate and the film is as follows: $[0001]_{GaN} \parallel [010]_{LiAlO_2}$ and $[11\bar{2}0]_{GaN} \parallel [001]_{LiAlO_2}$. Similar XRD measurements were

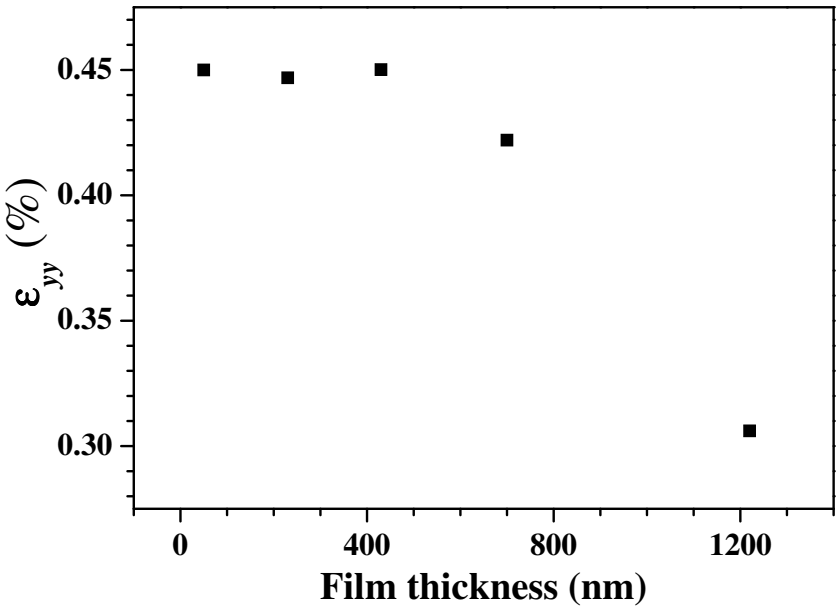

Figure 3.3: The variation of the out-of-plane strain ϵ_{yy} as a function of the film thickness. The strain remains constant up to film thicknesses of 0.4μm and start to decrease after that.

done for films with different thicknesses ranging from 0.5 nm to 1.22 μm in order to quantify the strain state. The results are shown in Fig. 3.3, where we plot the out-of-plane strain ϵ_{yy} as a function of film thickness. We find that ϵ_{yy} is constant with a value around 0.44% for film thickness up to 0.4 μm. However, the out-of-plane strain starts to decrease for thicker films and falls to ϵ_{yy}=0.29% for a film thickness of 1.22 μm. As we will see in the course of the discussion, the polarization anisotropy is a combined effect of the film thickness as well as the in-plane strain. We therefore expect that the *M*-plane GaN film with a thickness of 0.7 μm will exhibit a maximum in-plane polarization anisotropy because the strain is close to the maximum value for a rather thick film. Therefore, we chose this film for the detailed optical investigation of the in-plane polarization anisotropy.

3.3 *A*-plane GaN thin films on *R*-plane sapphire

The *A*-plane GaN film was grown by metal-organic vapor-phase epitaxy (MOVPE) on *R*-plane sapphire. The sample consists of a 0.2 μm-thick AlN nucleation layer followed by a 1 μm-thick, undoped GaN film. A detailed description of the growth conditions and the post-growth characterization of such films can be found in Ref. [9]. The *A*-plane orientation of the GaN film was verified using high-resolution triple-axis x-ray diffraction (XRD) and Raman spectroscopy. The room-temperature XRD measurements shown in Fig. 3.4, result in a Bragg angle of θ_B= 26.17° for sapphire (2$\bar{2}$04), while θ_B= 28.75° for GaN (11$\bar{2}$0). The x-ray measurement suggests that the GaN film has an overall biaxial, compressive in-plane strain with an out-of-plane dilatation ϵ_{xx} = 0.09%, where x, y, and z are parallel to the [11$\bar{2}$0], [$\bar{1}$100], and [0001] directions, respectively. A compressive in-plane strain is expected in the GaN film due to the large lattice mismatch in the y and z direction of -2.4% and -3.9%, respectively, relative to AlN and -16% and -1%,[46] respectively, relative to the sapphire substrate. However, due to

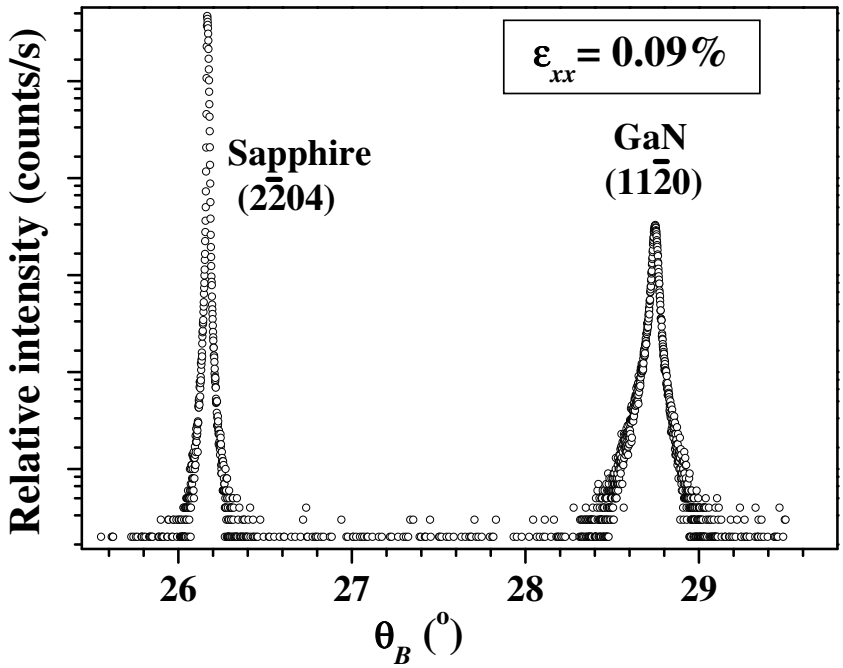

Figure 3.4: Relative ω-2θ symmetric x-ray scan for a 1 μm-thick *A*-plane GaN grown on *R*-plane sapphire. The out-of-plane dilation measured by x-ray is ϵ_{yy}= 0.09%. The substrate peak is taken as a reference.

the large lattice mismatch, the AlN and GaN films are probably relaxed at the growth temperature so that the strain is most likely due to the mismatch in thermal expansion coefficients. No simulations are done for this sample because the simulation software does not provide the fit parameters for *R*-plane sapphire substrate. The epitaxial relationship between the substrate and the film is as follows: $[0001]_{\text{GaN}} \parallel [\bar{1}101]_{\text{sapphire}}$ and $[\bar{1}100]_{\text{GaN}} \parallel [11\bar{2}0]_{\text{sapphire}}$.

3.4 Summary

In this chapter, we discuss the strain state and give a brief introduction to the growth conditions for *C*-, *M*-, and *A*-plane GaN grown on various substrates. The out-of-plane strain depends on the substrate and the thickness of the film. While, the *C*-plane GaN is unstrained and *A*-plane GaN has a small value of out-of-plane strain, the *M*-plane film remain fully strained up to film thickness of 0.4μm and starts to relax for thicker film.

Chapter 4

Optical processes in GaN semiconductors

In this chapter, we investigate the optical properties of the *C*-, *M*-, and *A*-planes GaN thin films. The transition energies and the polarization properties of the three transitions are measured using various optical techniques, and the results are explained using the theoretical calculations presented in Chapter 2.

4.1 Basics of optical properties and measurements techniques

4.1.1 The complex dielectric function in isotropic media

The radiation propagating through an uncharged, isotropic, homogeneous semiconductor having a permeability μ, a dielectric constant ϵ, and an electrical conductivity σ obeys Maxwell's equations (SI units): [75]

$$\begin{aligned} \boldsymbol{\nabla} \times \mathbf{H} - \frac{\partial \mathbf{D}}{\partial t} &= \mathbf{J}_f, \\ \boldsymbol{\nabla} \times \mathbf{E} + \frac{\partial \mathbf{B}}{\partial t} &= 0, \\ \boldsymbol{\nabla} \cdot \mathbf{D} &= \rho_f, \\ \boldsymbol{\nabla} \cdot \mathbf{B} &= 0, \end{aligned} \tag{4.1}$$

where **E** is the electric field, **D** the electric displacement, while **H** the magnetic field strength and **B** is the magnetic induction. ρ_f and J_f are the free charge and current density.

The constitutive equations are written as:

$$\begin{aligned} \mathbf{D} &= \epsilon_0 \mathbf{E} + \mathbf{P}, \\ \mathbf{B} &= \mu_0 \mathbf{H} + \mathbf{M}, \\ \mathbf{j} &= \sigma \mathbf{E}, \end{aligned} \tag{4.2}$$

P and **M** are the electric and magnetic polarizations, respectively. Eq. (4.2) defines the quantity **P** and **M**, from which the concept of the complex dielectric function can be developed for a linear medium, where $\mathbf{P} = \epsilon_0 \chi_e \mathbf{E}$ and $\mathbf{M} = \chi_m \mathbf{H}$. From Maxwell's equations and the constitutive equations, we obtain a wave equation for the field variables **E** and **H** :

$$\begin{aligned} \nabla^2 \mathbf{E} &= \epsilon\mu \frac{\partial^2 \mathbf{E}}{\partial t^2} + \sigma\mu \frac{\partial \mathbf{E}}{\partial t}, \\ \nabla^2 \mathbf{H} &= \epsilon\mu \frac{\partial^2 \mathbf{H}}{\partial t^2} + \sigma\mu \frac{\partial \mathbf{H}}{\partial t}. \end{aligned} \tag{4.3}$$

For optical fields, we must look for a sinusoidal solution to Eq. (4.3)

$$\mathbf{E} = \mathbf{E}_0 e^{i(\mathbf{K}\cdot\mathbf{r} - \omega t)}, \tag{4.4}$$

where **K** is a complex wavevector and ω is the frequency of the radiation. A solution similar to Eq. (4.4) is obtained for the **H** field. The substitution of the plane wave solution Eq. (4.4) into the wave equation Eq. (4.3) yields the following relation for **K**:

$$K^2 = \epsilon\mu\omega^2 + i\sigma\mu\omega. \tag{4.5}$$

If there are no losses (or attenuation), K is equal to

$$K_0 = \omega\sqrt{\epsilon\mu}, \tag{4.6}$$

and is real, but in general there are losses. So we define the complex dielectric function as

$$\epsilon_{\text{complex}} = \epsilon_1 + i\epsilon_2. \tag{4.7}$$

which gives rise to a complex wavevector

$$K = K_+ + iK_-, \tag{4.8}$$

The real part of **K** can be identified as the wavevector, while the imaginary part of **K** accounts for attenuation of the wave inside the solid. After substitution for **K** in Eq. (4.4), the solution to the wave equation [Eq. (4.3)] yields a plane wave. The solutions are shown for a wave travelling along the x-direction for simplicity.

$$\mathbf{E}(x,t) = \mathbf{E}_0 e^{-K_- x} e^{i(K_+ x - \omega t)}. \tag{4.9}$$

For the wave propagating in vacuum ($\epsilon = 1, \mu = 1, \sigma = 0$), Eq. (4.9) reduces to a simple plane wave solution. However, if the wave is propagating in a medium of finite electrical conductivity, the amplitude of the wave exponentially decays over a characteristic distance δ given by

$$\delta = \frac{1}{K_-} \tag{4.10}$$

Here δ is called the penetration depth. This means that the intensity of the electric field, $|E|^2$, falls to 1/e of its value at the surface in a distance $\frac{1}{\alpha_{abs}} = \frac{1}{2K_-}$ where α_{abs} is the absorption coefficient for the solid at frequency ω. A factor of two comes because the absorption coefficient is related to the intensity and not the amplitude of the electric field. Meanwhile, the real part of K determines the wavelength, the propagation speed, and the index of refraction in the usual way:

$$\lambda = \frac{2\pi}{K_+}, v = \frac{\omega}{K_+}, n = \frac{cK_+}{\omega}. \tag{4.11}$$

4.1.2 Relationship between optical constants

If we define the complex refractive index as:

$$N_{\text{complex}}(\omega) = \sqrt{\mu\epsilon_{\text{complex}}} = \frac{K}{\omega} = \sqrt{\epsilon\mu(1 + \frac{4\pi i\sigma}{\epsilon\omega})} = n(\omega) + ik(\omega), \tag{4.12}$$

the quantities n and k are collectively called the optical constants of a material, where n is the index of refraction and k is the extinction coefficient. For non-magnetic materials, we can take $\mu = 1$ and this will be done for all equations henceforth. We can relate the complex dielectric constant $\epsilon_{\text{complex}}$ to the complex index of refraction as follows:

$$\begin{aligned} \epsilon_{\text{complex}} = \epsilon_1 + i\epsilon_2 &= (n + ik)^2, \\ \epsilon_1 &= n^2 - k^2, \\ \epsilon_2 &= 2nk, \end{aligned} \tag{4.13}$$

where ϵ_1, ϵ_2, n, and k are all frequency dependent. The absorption coefficient is related to the extinction coefficient in the following way

$$\alpha = \frac{2\omega k}{c} \tag{4.14}$$

$$\Rightarrow \alpha = \frac{4\pi k}{\lambda}, \tag{4.15}$$

where λ is the wavelength of the light. Since light is described by a transverse wave, there are two possible orthogonal directions for the **E** vector in a plane normal to the propagation direction and these directions determine the polarization of the light. For cubic materials, the index of refraction is the same along the two transverse directions. However, for anisotropic media, the indices of refraction may be different for the two polarization directions, as is discussed in the next chapter.

The reflection and refraction of a plane wave at an interface between two media with different dielectric properties can be explained as follows: a plane wave incident on the interface will, in general, be split into two waves: a transmitted wave proceeding into the second medium and a reflected wave propagating back into the first medium. The existence of these two waves is a direct consequence of the boundary conditions on the field vectors, **E** and **B**. The treatment of an anisotropic medium, which has different dielectric constants for different polarizations of light, warrant a different analysis as opposed to an isotropic medium. We will deal with the detailed analysis of the transmittance and reflectance of both isotropic and anisotropic media in the next chapter and will focus on the general optical properties of GaN thin films in this chapter.

4.1.3 Absorption versus emission processes in semiconductors

In order to determine the absorption properties, the response of the semiconductor to the electromagnetic radiation has be determined. The Hamiltonian for an electron in a solid interacting with an electromagnetic wave is given by:[76]

$$\mathbf{H}(\mathbf{p},\mathbf{r},t) = \frac{(\mathbf{p}+e\mathbf{A})^2}{2m} + V(\mathbf{r}), \tag{4.16}$$

where $\mathbf{A}(\mathbf{r},t)$ denotes the vector potential. Choosing the Coloumb gauge, the electric field **E** and the magnetic field **B** of the light wave are given by $\mathbf{E} = -\partial\mathbf{A}/\partial t$ and $\mathbf{B} = \boldsymbol{\nabla}\times\mathbf{A}$, respectively. The Hamiltonian in Eq. (4.16) reduces to

$$\mathbf{H}(\mathbf{p},\mathbf{r},t) = \mathbf{H}_0(\mathbf{p},\mathbf{r}) + \frac{e}{m}\mathbf{A}\cdot\mathbf{p} + \frac{e^2}{2m}\mathbf{A}^2. \tag{4.17}$$

We will neglect in the first-order perturbation theory, the quadratic term in Eq. (4.17) and will only deal with the linear response of the system. The resulting perturbation consisting of the second term in Eq. (4.17) is referred to as the electron-radiation interaction Hamiltonian $\mathbf{H}_{er}$

$$\mathbf{H}_{er} = \frac{e}{m}\mathbf{A}\cdot\mathbf{p}. \tag{4.18}$$

Assuming a plane wave for light, the vector potential and the electric field are related through

$$\mathbf{A}(\mathbf{r},t) = \frac{\hat{e}\mathbf{E}}{2\omega}\{\exp[i(\mathbf{K}\cdot\mathbf{r}-\omega t)] + \text{complex conjugate}\}, \tag{4.19}$$

where $\hat{e}$ denotes the polarization vector, ω the frequency of the light wave, and **K** the wavevector. Using Fermi's golden rule as the approach to the time-dependent perturbation theory, the transition probability, R, for absorption is given by

$$R(\hbar\omega) = \frac{2\pi}{\hbar}\sum_{\mathbf{K}_C,\mathbf{K}_V}|\langle C|H|V\rangle|^2[\delta(E_C(K_C)-E_V(K_V)-\hbar\omega)+\delta(E_C(K_C)-E_V(K_V)+\hbar\omega)]. \tag{4.20}$$

The delta function ensures energy conservation. The term with the minus sign in front of the photon energy corresponds to the absorption signal, the term with the plus sign describes stimulated emission, i.e., emission in the presence of an external field.

We will consider only the absorption term in the discussion below. Since a photon carries a very small momentum compared to a typical wavevector of the first Brillouin zone of the solid, the optical transitions are almost vertical in **K**-space. The expectation value of the perturbation operator can be written as

$$|\langle C|H_{er}|V\rangle|^2 = (\frac{e}{m\omega})^2|\frac{E}{2}|^2|P_{CV}|^2, \tag{4.21}$$

where the momentum matrix element $P_{CV} = \langle C|\hat{e}\cdot\mathbf{p}|V\rangle$ is assumed to be independent of the wavevector. The transition rate per unit volume is then given by

$$R(\hbar\omega) = \frac{2\pi}{\hbar}(\frac{e}{m\omega})^2|\frac{E}{2}|^2|P_{CV}|^2\sum_{\mathbf{K}}[\delta(E_C(\mathbf{K}) - E_V(\mathbf{K}) - \hbar\omega). \tag{4.22}$$

This transition rate per unit volume multiplied by the photon energy $\hbar\omega$ is simply the power loss of the incident light due to absorption in the unit volume and depends on the absorption coefficient α. The incoming light intensity is related to the electric field by $I = \frac{\epsilon_0}{2}cn|E|^2$, where n denotes the index of refraction. The power loss R$\times\hbar\omega$ is given by the change in intensity

$$\frac{c}{n}R\times\hbar\omega = -\frac{dI}{dt} = -\frac{dI}{dx}\frac{dx}{dt} = \frac{c}{n}\alpha I. \tag{4.23}$$

The absorption coefficient can therefore be expressed as

$$\alpha(\hbar\omega) = \frac{\hbar\omega}{I}R(\hbar\omega). \tag{4.24}$$

Using Eqs. (4.22) and (4.24), we obtain for the absorption coefficient

$$\alpha(\hbar\omega) = \frac{\pi e^2}{\epsilon_0 m^2 cn\omega}|P_{CV}|^2\times\sum_{\mathbf{k}}[\delta(E_C(\mathbf{k}) - E_V(\mathbf{k}) - \hbar\omega). \tag{4.25}$$

The coefficient in front of the sum $\frac{\pi e^2}{\epsilon_0 m^2 cn_r\omega}|P_{CV}|^2$ can be written in terms of the oscillator strength f_{VC} of the optical transition, which is determined by the momentum matrix element

$$f_{VC}(\hbar\omega) = \frac{2|P_{CV}|^2}{m\hbar\omega}. \tag{4.26}$$

For semiconductors with a direct fundamental energy gap, the optical transitions take place near the centre of the Brillouin zone. In this case, the absorption coefficient is given by:[76]

$$\alpha(\hbar\omega) = \frac{\sqrt{m}e^2}{\sqrt{2}\pi\epsilon_0 cn_r\hbar^2}(\frac{\mu^*}{m})f_{VC}\times\sqrt{\hbar\omega - E_G}\Theta(\hbar\omega - E_G), \tag{4.27}$$

where $\mu^*$is the reduced effective mass, which is defined as $\mu^{*^{-1}} = m_e^{*^{-1}} + m_h^{*^{-1}}$, while m_e and m_h are the effective masses of the electron and holes, respectively.

The oscillator strength was discussed in great detail as a function of in-plane strain in Chapter 2. Eq. (4.27) suggests that the oscillator strength is related to the absorption

coefficient, hence one expects to see a similar dependence of absorption coefficient on strain. Due to the reduced crystal symmetry of GaN, the dielectric constant depends on the polarization of the incoming light. The case of nonpolar GaN is especially interesting because one expects to see in-plane polarization anisotropy in the optical response. Therefore the reflectance, transmittance and photoluminescence should be different for probe light with different linear polarization.

Using Eqs. (4.26) and (4.27) we have for direct semiconductors $(\alpha \times \hbar\omega)^2 \propto (\hbar\omega - E_G)$. In order to determine the energy gap of a semiconductor, one can determine the absorption coefficient as a function of energy from the measured reflectance and transmittance. One normally measures the reflectance R and the transmittance T of the respective material as a function of energy. The absorption coefficient can be obtained from the absorbed intensity. Neglecting interference effects, the absorbed intensity normalized to the incident intensity is given by $(1-R)[1-exp(-\alpha d)]$, where d denotes the film thickness. Due to the conservation of the energy flux and neglecting scattering, the sum of the reflected, transmitted, and absorbed intensity should be equal to the incident intensity, i.e.,

$$R + T + (1 - R)[1 - \exp(-\alpha d)] = 1. \tag{4.28}$$

Solving this equation for α, one obtains $\alpha = \frac{1}{d}\ln(\frac{1-R}{T})$. The calculated absorption coefficient is then fitted to determine the band gap.

In addition to measuring the reflectance and the transmittance, to calculate the absorbing coefficient giving the band gap energy, there are other optical techniques, such as photoluminescence and photoreflectance, to measure the band gap more directly. We give a brief introduction to these techniques.

4.1.4 Photoreflectance spectroscopy

The photoreflectance (PR) technique is a modulation spectroscopy based in which instead of directly measuring the optical spectrum (reflectance or transmittance), the derivative with respect to some parameter such as electric field is evaluated. This can be accomplished by modulating some property of the sample or perturbing a system in a periodic fashion and measuring the corresponding change in the reflectance or transmittance. Examples of the perturbations, which correspond to different modulation methods, are for, e.g., changes in the electric or magnetic field, heat pulse, or uniaxial stress. Such repetitive perturbations modify the spectral response of the sample, giving rise to differential-like spectra in the region, where optical transitions occur. Because of this derivative-like nature, a large number of sharp spectral features can be observed in modulated reflectance spectra of semiconductors even at room temperature. With these sharp, well-resolved spectra, it is possible to analyze and yield the properties such as transition energy or lineshape, of the material under study. Changes in reflectance as small as $10^{-6} - 10^{-7}$ can be observed using phase-sensitive techniques. The ability to perform a lineshape fit is one of the great advantages of photoreflectance modulation spectroscopy. Since, for the modulated signal, the features are localized in energy, it is possible to account for the lineshapes to yield accurate values of important parameters such as energies and broadening functions of interband (intersubband) transitions. For example, even at 300 K it is possible to obtain the energy of a particular feature to within a few meV. The extensive fundamental experimental and theoretical

work in the area of modulation spectroscopy during the last 25 years, particularly the electroreflectance and photoreflectance methods, have provided the necessary framework to develop the technique into a powerful tool for material and device characterization.

In the photoreflectance technique, a modulated laser beam with an energy above the band gap of the GaN thin film being studied creates a photoinduced variation in the built-in surface electric field. Because of the pinning of the Fermi energy at the surface, there exists a space-charge layer. The occupied surface states contain electrons from the bulk. Photoexcited electron-hole pairs are separated by the built-in field, with the minority carrier (holes for n-type semiconductor) being swept toward the surface. At the surface, the holes neutralize the trapped charge, reducing the built-in field. The surface field modulation is resolved in the reflection spectra, and it has been shown to be sensitive to critical point transitions in the Brillouin zone with the resulting spectrum exhibiting sharp derivative-like features and typically a featureless background. In addition, weak features that may be difficult to observe in the reflectance or absorption spectrum can be enhanced. For well-known critical points in the Brillouin zone, it is possible to account for the lineshapes in a modulation spectrum. A drawback of PR is the spurious modulated background signal reaching the detector because of (a) photoluminescence from the sample and/or (b) scattered light from the pump source. The PR technique has been demonstrated [77, 78] to be a valuable method for the characterization of compound semiconductors, heterostructures, and multiple quantum wells.

In this work, we will focus on determining the transition energies of the free excitons using PR. The experimental details are as follows. The modulation of the built-in electric field of the sample is caused by photo-excited electron-hole pairs generated by the pump source, which is chopped/modulated at a certain frequency. Light is focused on the sample having an intensity of $I_0(\lambda)$. The reflected light is then focused on to the photodetector. The light striking the detector contains two signals: the unmodulated signal given by $I_0(\lambda)R(\lambda)$, where $R(\lambda)$ is the reflectance of the material, and the modulated signal $I_0(\lambda)\Delta R(\lambda)$, where $\Delta R(\lambda)$ is a change in the reflectance produced by the modulation source. This signal is measured by a lock-in amplifier, which is set to the frequency of the modulated pump light source. The value of interest is the ratio of these two quantities, i.e., $\Delta R/R$ which is the relative change in the reflectance due to the pump beam. The signal $\Delta R/R$ is then fitted using various lineshapes to determine the quantities of interest such as transition energy and linewidths. In most PR experiments, the critical point energy is determined by fitting the shape of the signal at the band edge with a first- or third-derivative functional form for low electric fields. Gaussian functions are used to fit the experimental data measured at high temperatures, because this form describes high exciton-phonon coupling and inhomogeneous perturbation of a system with a Gaussian absorption profile of excitonic transitions. [79] Alternatively Lorentzian line shapes functions can be used, where the fit exponent is a characteristic parameter, which depends on the type of critical point in the Brillouin zone and the order of the derivative. While a PR spectrum exhibits sharp derivative-like structures on a featureless background due to the optical modulation, the order of the derivative is not immediately clear. One can choose a different exponent in the fit function depending on the type of the transition [80] to fit the PR spectral structures

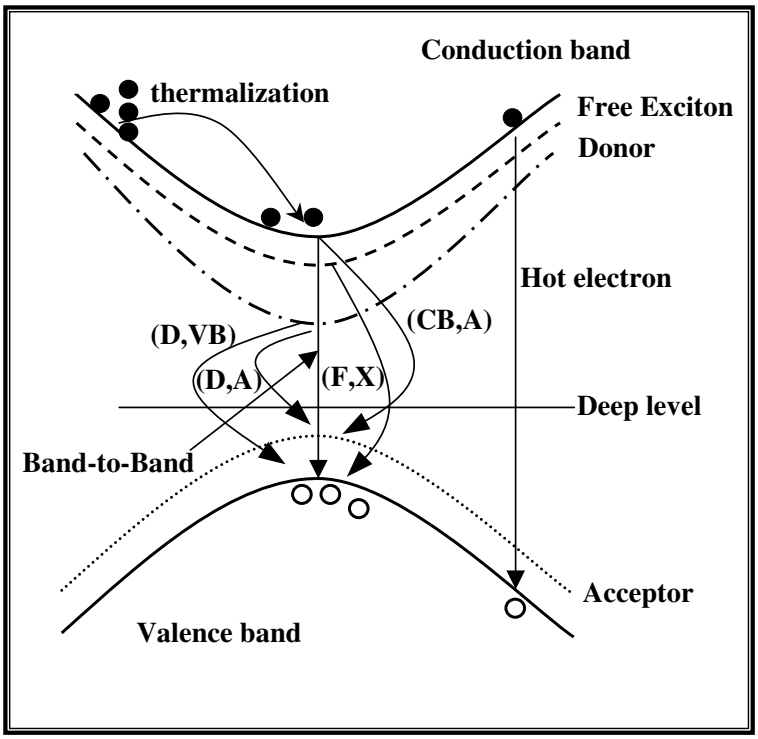

Figure 4.1: Illustration of several possible radiative recombination mechanisms. See text for explanation.

associated with fundamental band-gap transitions in bulk materials.

4.1.5 Photoluminescence spectroscopy

In an emission process, an electron occupying a higher energy state makes a discrete transition to an empty lower-energy state. For a radiative transition, the energy difference between these two states is emitted as photons, whereas for non-radiative transition this energy difference is emitted in form of heat, i.e., phonons. The radiation rate is determined by the product of the density of carriers in the final lower states with the density of carriers in the higher energy initial state. This is similar to rate of absorption according to the van Roosbroeck-Shockley relation. It can be shown that the PL signal is confined to a small energy due to the Fermi-Dirac distribution of carriers, which make it strongly dependent on the temperature. Emission processes only occur between a narrow band of states occupied by thermalized electrons with a narrow band of empty states containing the holes at the top of the valence band. This commonly yields a spectrum much narrower than that for absorption. When the excitation is optical in nature, the emission process is called photoluminescence (PL). PL from a semiconductor involves measuring of the energy distribution of emitted photons after optical excitation. This energy distribution is then analyzed in order to determine properties of the material, including defect species, defect concentrations, possible stimulated emission, etc. PL can be used to determine (1) optical emission efficiencies, (2) composition of material (e.g., alloy composition), (3) impurity content, (4) layer thicknesses (e.g., quantum well thicknesses), etc.

Radiative recombination in a semiconductor may occur by several mechanisms.

The lowest energy state in an ideal crystal is the free exciton-polariton, which in principle, does not decay because of momentum conservation. The actual exciton-polariton lifetime is thus determined by scattering with phonons, impurities, and surfaces. At low temperatures, however, the exciton may instead be captured by the impurities giving rise to bound exciton transitions which then dominate the spectrum. At higher temperatures, the polariton character of the exciton is gradually washed out, and it becomes as active in recombination as expected from the semiclassical theory. However, band-to-band transitions now compete with exciton recombination and gradually take over for thermal energy, $k_B T$, exceeding the exciton binding energy.

There are many possible radiative recombination mechanisms in a semiconductor, and Fig. 4.1 illustrates a few. Band-to-band recombination is the across-bandgap transition of a free electron in the conduction band to a free hole in the valence band. As a result, this emission occurs at energies equal to or larger that the band gap. Recombination at energies greater than the band gap is due to the recombination of "hot carriers" which have not fully relaxed to the bottom (top) of the conduction (valence) band prior to recombination. Free electrons and holes may become bound via the Coloumb interaction to form free excitons (F,X), which are ground state, quasi-particles in a semiconductor. Free-to-bound transitions involve the radiative recombination of a free-carrier with a carrier bound to an impurity, for example, donor-to-valence band (D,VB) or conduction-band-to-acceptor (CB,A). This emission always occurs at energies less than the bandgap. Excitons may also become bound to impurities [either donors (D,X) or acceptors (A,X)] and give rise to sub-bandgap radiation. Donor-acceptor pair (DAP) emission involves the radiative recombination of an electron bound to a donor and a hole bound to an acceptor. This emission occurs below the bandgap and is sensitive to the relative distance between the donor and acceptor impurity pair. Recombination via an intermediary state (i.e., deep level) has been termed as Shockley-Read-Hall recombination and is primarily non-radiative in nature. Excitonic recombination usually gives rise to narrow emission lines in contrast to other recombination explained above. There are specific spectral signatures of various recombination processes, which in conjunction with the information about the structural properties, makes it possible to identify the recombining species and will be discussed wherever relevant.

PL spectroscopy is widely used to characterize GaN and its alloys. For example, estimations of the acceptor concenteration in n-type GaN have been obtained by making a comparison of the ratio of defect and near band-edge PL intensities. [81, 82] The temperature-dependent defect-related PL intensity is typically used to determine the nature of an optical transition. For example, one would differentiate between DAP transition and (CB,A) transition by the temperature behaviour of the PL. [83, 84] Additionally, the complex dependencies of the PL spectrum on temperature and excitation intensity can provide important information on the characteristics of point defects and carrier kinetics in semiconductors.

We now carry out the optical characterization of GaN thin films using the techniques discussed above. The primary aim is to determine the excitonic transition energies and to compare the experimental results with the results of the theoretical calculations given in Chapter 2. The optical response of GaN grown along different orienta-

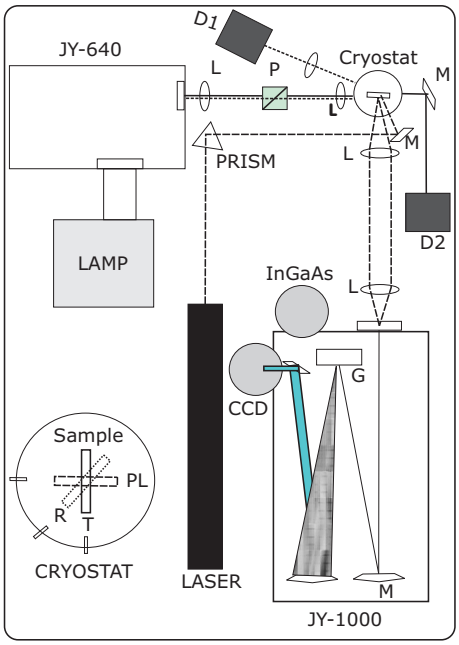

Figure 4.2: Setup for the measurement of optical properties such as Reflectance (R), Photoreflectance (PR), Transmittance (T) and Photoluminescence (PL). JY-640 is a 0.64 m monochromator, L denotes Lenses, P is Glan-Taylor Polarizer, M is Mirror, JY-1000 is a 1 m monochromator. D1 denotes a Si-photodetector for reflectance while D2 is used for transmittance. LAMP is a 75 W Xenon-arc Lamp while LASER is a 325-nm He-Cd Laser with maximum power of 50 mW. The beam path for R is shown by dotted line, whereas T is shown by solid line. The dashed line shows the beam path for PL. The cryostat configuration can be changed accordingly, to measure R, T and PL as shown in the figure.

tion is measured. We will briefly discuss the polarization properties of the *M*- and the *A*-plane GaN thin films.

4.2 Optical characterization of GaN semiconductor thin films

We have performed spectrally resolved reflectance, transmittance, photoreflectance (PR) and photoluminescence (PL) measurement on the GaN samples grown along various orientations. The optical setup for the measurement is shown in Fig. 4.2. The probe beam for reflectance, transmittance and PR is achieved by dispersing white light from a 75 W Xenon lamp (marked LAMP in Fig. 4.2) using a 0.64 m monochromator (JY-640) having a grating with 1200 lines/mm supplied by Jobin Yvon. The polarization of light is controlled by using a Glan-Taylor prism (P), and the signal is detected using an UV-enhanced Si photodetector (D1 for reflectance and D2 for transmittance). The sample is kept in a cryostat and the temperature can be controlled from 5 to 300 K. Liquid He is used to cool the samples. The angle of the incident beam with respect to the surface normal to the sample is changed for different experiments. This is marked in Fig. 4.2 by *R*, *T*, PL (in the cryostat sketch) in order to measure reflectance, transmittance and photoluminescence, respectively. The measurement is done at normal incidence for transmittance and at an oblique angle of 10° for reflectance. The spot size on the sample is 3 mm $\times$ 1 mm.

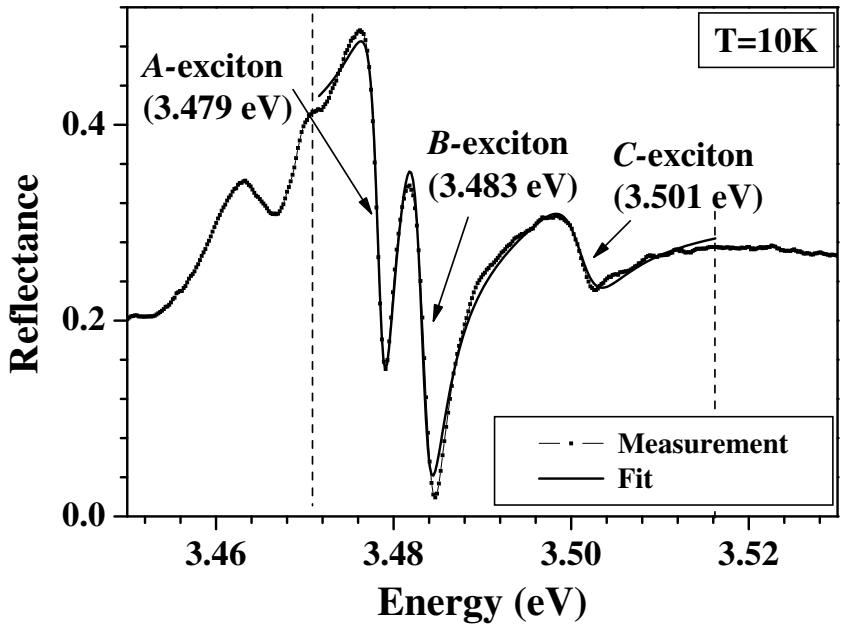

Figure 4.3: Reflectance of a 1 μm-thick *C*-plane GaN film grown on a 200 μm-thick GaN substrate measured at 10 K. The reflectance spectra is fitted using a damped-oscillator model as presented in Eq. (4.29). The point denotes the measurement, while the line denotes the fit. The dashed lines mark the range of the experimental data used for fitting.

The excitation source for the PL and PR is a 325-nm He-Cd laser with the maximum power of 50 mW. The excitation density of the laser can be controlled by using neutral-density filters (NDF). The PL spectrum is collected using lenses and dispersed into a 1 m monochromator, JY-1000, (Jobin Yvon) with a grating of 600 lines/mm. The slit width of 50 μm is used which gives an experimental resolution of $\approx$ 1 meV. The PL measurement is done in a front-face excitation geometry, and the PL spectrum is collected using a liquid-Nitrogen (LN_2)-cooled charged-coupled device (CCD) camera which consists of an array of Si-photodetectors. The spot size for the laser beam used for excitation is 200 μm. The measured reflectance, transmittance, PR and PL spectra are corrected for the spectral characteristics of the lamp and the complete spectrometer. The monochromator was calibrated using specific lines from a Xenon calibration lamp. A mechanical chopper with the frequency of 180 Hz is used in conjunction with a lock-in amplifier for better signal-to-noise ratio, to modulate the probe beam in reflectance and transmittance and the pump beam in PR.

4.2.1 *C*-plane GaN films

In reflectance and photoluminescence spectra of GaN layers, the built-in stress and the crystal quality plays an important role: The linewidths and the lineshapes are determined by the inhomogeneous strain distribution. The position of the PL emission line largely depends on the homogeneous strain, which exist in the layers due to the different lattice constants and thermal expansion coefficients of the layer and the substrate. Additionally, an uncontrolled incorporation of intrinsic and extrinsic defects also contributes to the linewidth broadening and gives rise to additional lines in the optical

spectra. To overcome these problems and to obtain reliable data on physical properties of "ideal" GaN, it is necessary to perform spectroscopy on GaN epitaxial layers grown on thick GaN. This would inhibit the creation of defects, which are related to lattice mismatch and thermal expansion coefficient mismatch between the substrate and the film. The optical properties of a *C*-plane GaN layer grown on bulk GaN were investigated near the band gap region in order to determine the excitonic transition energies.

Reflectance: Spectrally resolved reflectance spectroscopy was carried out at near-normal incidence. The experimental resolution for the reflectance experiment is 1 meV in the wavelength range 350–360 nm. The reflectance spectrum at 10 K is plotted in Fig. 4.3. It shows well resolved, very sharp resonances from the free excitons X_A, X_B, and X_C associated with the threefold-split valence band, the details of which were discussed in Chapter 2. The minima of the resonances are sharp indicating an exceptionally low damping. The following curves are fitted to the reflectance spectrum:[85]

$$R(E) = R_0 + R_X \mathfrak{Re}\left(\frac{E_X - E + i\Gamma_X}{\Gamma_X^2 + (E - E_X)^2} e^{i\Theta_X}\right), \tag{4.29}$$

where $\mathfrak{Re}$ is for the real part of the function, R_x is the reflectance, E_X is the transition energy and γ_X a broadening parameter of the exciton X. Θ_X is the phase factor, which accounts for the influence of non-uniform electric fields and interference and electron-hole interaction effects, while R_0 is the background. We use the summation of three Lorentzian functions to fit the experimental data as was done by Korona *et al.* [85] The parameters achieved by fitting the above function to the experimental data are shown in Table 4.1. The transition energies of the free excitons formed with the electrons in the CB and the holes in the crystal-field and spin-orbit split valence bands. The broadening parameters for the *A*- and *B*-exciton are nearly equal i.e, $\Gamma_A = \Gamma_B$. Narrow linewidths suggest that the sample is of good quality. The three excitonic transition energies E_A, E_B and E_C are the same within the experimental error as obtained from luminescence spectra which are shown later.

The transition energies for our samples are compared with the values obtained by other groups as shown in Table. 4.2. The excitonic transition energies for the *A*-, *B*-, *C*- excitons vary considerably for the samples grown on different substrates. As previously explained, the in-plane strain, which is isotropic for the *C*-plane GaN, modifies the band gap and shifts its energy. The energies obtained for our unstrained GaN film can be directly compared to the transition energies for samples grown on GaN substrates (cf. rows 2 and 3 in Table. 4.2). It is found that the thick GaN has typically the

Table 4.1: Parameters achieved by fitting the experimental data for reflectance measured for 1 μm-thick *C*-plane GaN film at 10 K. The measured data and the fit are shown in Fig. 4.3.

Exciton X	E_X (eV)	Γ_X (meV)	Θ_X
A	3.479	1.3	0.64
B	3.483	1.5	0.23
C	3.501	3	0.12

Table 4.2: Comparison of bound and free exciton peak positions reported by other groups and present values recorded at low temperatures ($T < 10$ K). The energies for the free exciton were taken from damped oscillator fits to the reflectance spectra.[87] The energy for D^0-X_A is determined by PL measurements.

Substrate material	Layer thickness	D^0-X_A (eV)	X_A (eV)	X_B (eV)	X_C (eV)
GaN (Our Studies)	1 μm	3.471	3.479	3.483	3.501
GaN Ref. [88]	0.4 μm	3.471	3.479	3.483	3.499
GaN Ref. [87]	1.5 μm	3.471	3.477	3.482	3.499
Sapphire Ref. [89]	100-250 μm	3.466-3.468	3.474	3.480	3.501
Sapphire Ref. [90]	> 100 μm	3.469	3.475	3.482	3.493
Sapphire Ref. [91]	400 μm	3.473	3.480	3.486	3.503
Sapphire Ref. [86]	4 μm	-	3.485	3.493	3.518

same transition energies among each other within the experimental error, while the thin films grown on substrates other than GaN show large differences (cf. Ref. [86] in Table. 4.2). These differences are an indication of the strain existing in the heteroepitaxial GaN layers.

As was discussed in Chapter 2, the energy parameters such as deformation potentials, Luttinger parameters, and crystal field as well as spin-orbit splitting obtained for GaN show a large variation. Experimentally determined values differ among each other due to films grown on different substrates with different lattice mismatch leading to various underlying strain. We have calculated the spin-orbit coupling Δ_{so} and crystal-field splitting Δ_{cr} for GaN using the energy obtained for the excitonic transitions for our sample. To obtain the spin-orbit parameter Δ_{so} and the crystal-field parameter Δ_{cr} for GaN, we apply Hopfield's quasicubic model developed for wurtzite crystal structure.[92] The relation between the excitonic energy and the energy parameters is described by the following equation:

$$E_{B,C} - E_A = \frac{\Delta_{so} + \Delta_{cr}}{2} \pm [(\frac{\Delta_{so} + \Delta_{cr}}{2})^2 - \frac{2}{3}\Delta_{so}\Delta_{cr}]^{1/2}. \tag{4.30}$$

Inverting the above equation, we can achieve

$$\Delta_{so}; \Delta_{cr} = \frac{1}{2}[\Delta_{C,A} + \Delta_{B,A} \pm (2\Delta_{C,B}^2 - \Delta_{B,A}^2 - \Delta_{C,A}^2)^{1/2}], \tag{4.31}$$

where $\Delta_{X,Y} = E_X - E_Y$. In order to find the energies Δ_{so} or Δ_{cr} from Eq. (4.31), we only need the differences of excitonic energies. Using the excitonic transition energies listed in Tab. 4.1, we calculate: Δ_{so}= 18.9 meV and Δ_{cr} = 9.2 meV. For comparison, the values of the energy parameters Δ_{so} and Δ_{cr} obtained by various groups using experimental and theoretical studies, are collected in Table 4.3. Predictably, the values show large differences among them indicating that these parameters are sensitive to the strain in the film. However, for the case of the spin-orbit splitting, there is good agreement among all results. There is a wide variation in the values obtained for the crystal-field splitting, since these values are more strongly affected by strain. Our results agree well with the energy parameters obtained for homoepitaxial GaN as given by Stepniewski

Table 4.3: Comparison of the crystal-field splitting and spin-orbit splitting parameters, Δ_{cr} and Δ_{so}. The following relations hold using quasicubic approximations: $\Delta_{cr} = \Delta_1$ and $\Delta_{so} = 3\Delta_2 = 3\Delta_3$

Δ_{cr} (meV)	Δ_{so} (meV)	Methods	References
9.2	18.9	Experiment	Our Results
22	11	Experiment	Ref. [89]
72.9	15.6	Calculation	Ref. [51]
35	18	Calculation	Ref. [91]
11	17	Experiment	Ref. [91]
10	17.6	Experiment	Ref. [94]
22	15	Experiment	Ref. [63]
8.8	17.9	Experiment	Ref. [93]

et al. [93]

Photoluminescence: The luminescence spectrum measured near the bandgap at 10 K is shown in Fig. 4.4. In order to make sure that the contribution is coming from the top layer and not the thick underlying GaN template, PL measurements under identical conditions are done for the template alone. The excitonic transition peaks were not so clearly seen in the luminescence spectrum measured for the template. This may be due to the higher carrier concentration in the GaN substrate grown by HVPE as compared to the layer grown on top of it, which is grown by MBE. The higher background carrier concentration introduces damping of the excitonic resonances.

The low-temperature spectrum in Fig. 4.4 is dominated by two peaks, which are labelled as (D^0,X_A) and *A*-exciton. Other peaks are also seen in the vicinity of the main peaks and are labelled as *B*- and *C*-excitonic transitions, respectively. The (D^0,X_A) line is assigned to the exciton bound to neutral donors. The excitons are formed with the participation of a hole from the top-most valence band. The energy for this transition is E_{D^0,X_A}=3.471 eV. It is the narrowest line observed in the layer. The line labelled *A*-exciton is the free excitonic transition involving the electrons in the CB and the holes in the top-most VB of unstrained GaN. The energy of this line is E_A=3.478 eV. The *B*- and *C*- excitonic transitions arise from electrons in the CB and holes in the second highest VB for the *B*-exciton and in the third highest VB for the *C*-exciton, respectively. The transition energies for these lines are E_B=3.483 eV and E_C=3.501 eV, respectively. The lines are at the same energy as observed in reflectance within the experimental error. A comparison of the transition energy for the (D^0,X) transition obtained by PL, for samples grown on different substrates and of different thicknesses is shown in Table 4.2. Again, the defect-related transition energy depends on the substrate and the thickness of the film.

In addition to the dominant lines mentioned above, another weak line labeled as (D^0,X_B) is observed at E_{D^0,X_B}= 3.475 eV. The origin of this line can be associated with the neutral-donor bound exciton when the excitons are formed with the participation of holes from a second-highest valence band. Its presence may be due to the small splitting of the valence band well below the optical phonon energy, which is around

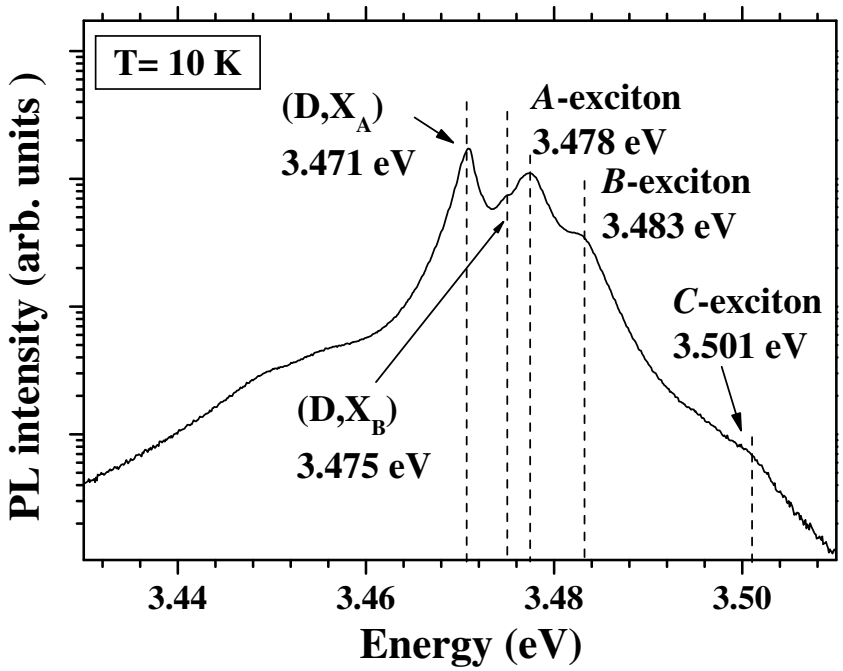

Figure 4.4: Photoluminescence (PL) for 1 μm-thick C-plane GaN film grown on 200 μm-thick GaN template measured at 10 K and plotted in a semi-logarithmic representation. Several peaks can be seen near the band gap, but the spectra are dominated by the donor-bound exciton peak (D,X_A) at 3.471 eV and the free excitonic transition peak for A-exciton at 3.748 eV. The transition energies for the B-exciton is 3.483 eV, while for C-exciton it is 3.501 eV. A small peak at 3.475 eV is also visible and attributed to excitons from a higher level bound to a donor, (D,X_B). The dashed lines denotes the peak-energy positions for various transitions.

90 meV at 300 K. Therefore, the nonradiative relaxation from this state is strongly suppressed.

Discussion: The XRD measurements reveal that the C-plane film is unstrained. Low-temperature reflectance and PL measurements can be used to exactly determine the energy of the excitonic transitions. Using these measurements, we determine the transition energy for the A-exciton to be 3.479 eV, B-exciton to be 3.483 eV and for the C-exciton to be 3.501 eV. In Chapter 2, we have calculated the dependence of the excitonic transition energies on the in-plane strain. This dependence is shown for the specific case of C-plane GaN in Fig. 4.5(a). The unstrained case, for which the in-plane strain values $\epsilon_{xx} = \epsilon_{yy}$ are identically 0, is denoted by black dots in the figure. The energy value obtained at these strain coordinates are as follows: For A-exciton = 3.478 eV, B-exciton = 3.485 and C-exciton = 3.508 eV. The A and B excitonic energy values match very well with the experimentally determined values within the experimental error of ± 1 meV. Figure 4.5(b) shows the oscillator strength, where the dots denote the case for unstrained GaN. It shows that the A- and B-exciton are equally $|x\rangle$- and $|y\rangle$-polarized, while the C-exciton is mostly $|z\rangle$-polarized. In the experimental configuration, when the light is propagating parallel to the z direction, the light polarization is in the x-y plane. We are able to detect finite C-exciton transition (T_3 transition in Fig. 4.5) because there is small but finite contribution for $|x\rangle$- and $|y\rangle$-polarization. When the light polarization lies in the $x - y$ plane, these non zero contributions add up to give finite transition for C-exciton in PL and reflectance measurements.

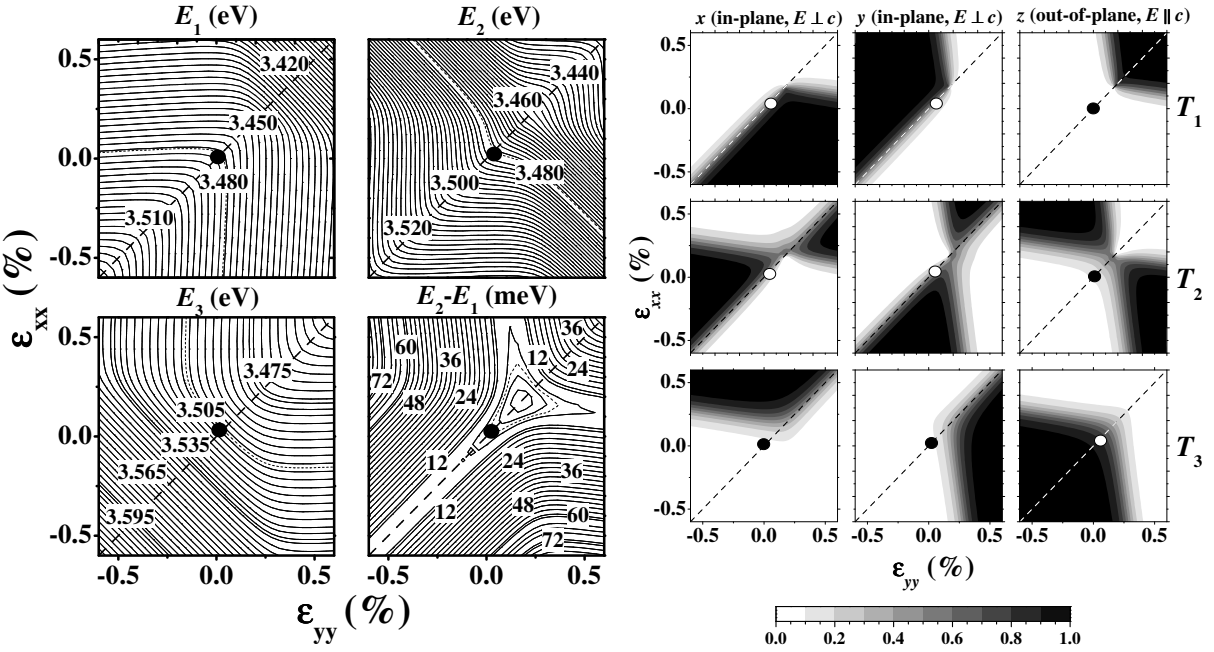

Figure 4.5: (a) Transition energy for T_1, T_2 and T_3 and the separation between the top two VB states, i.e., $E_2 - E_1$ as a function of in-plane (*C* plane) strain values. (b) x, y, and z components of the oscillator strength for the three transitions T_1, T_2 and T_3 as a function of in-plane strain for *C*-plane GaN. Dots denotes the in-plane strain values ($\epsilon_{xx} = \epsilon_{yy} = 0$) for the case of 1 μm-thick GaN film grown on thick GaN template.

In summary, GaN (0001) homoepitaxial layers have been grown using MBE on a single crystal GaN template. The low-temperature reflectance and PL spectra show narrow transition lines in the exciton region. These indicate that the homoepitaxial GaN layers have a good structural and optical properties. The experimentally determined transition energies can be explained by the calculations done in Chapter 2 taking into account that the film is relaxed.

4.2.2 *M*-plane GaN films

In an isotropic medium, one expects to see a similar optical response irrespective of the polarization of incoming light. The reflectance and transmittance of such a medium also remains invariant with the polarization direction. However, the optical properties are dissimilar for anisotropic media, where the material responds differently to various incoming polarization directions of light. The *M*-plane GaN film is clearly an anisotropic medium, since the oscillator strengths for the interband transitions depends on the in-plane polarization angle [cf. Chapter 2]. Theoretical calculations and results of the strain dependence of the interband energies as well as oscillator strengths reveal that for anisotropically strained *M*-plane GaN, with sufficiently large strain values, the VBs is modified in such a way that corresponding excitonic transitions involving the electrons in the conduction band with holes in the top three valence bands, i.e., T_1, T_2 and T_3, can be fully x-, z- and y- polarized, respectively. A schematic diagram of the band structure for such a situation is shown in Fig. 4.6. For an *M*-plane GaN film,

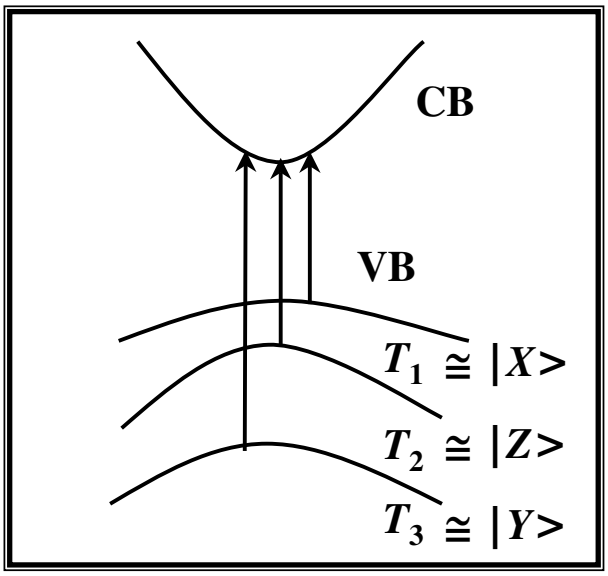

Figure 4.6: A schematic diagram showing the case, when the high in-plane strain modifies the band structure in such a way that the top three transitions T_1, T_2, and T_3 are purely x, z, and y polarized, respectively.

the unique c axis of the wurtzite crystal structure lies in the film plane. For light polarized in the M plane, only two transitions T_1 and T_2 have to be considered. These two transitions occur for light linearly polarized parallel to the z axis ($\boldsymbol{E} \parallel \boldsymbol{c}$) and parallel to the x axis ($\boldsymbol{E} \perp \boldsymbol{c}$).

Photoluminescence: We measure the PL spectra of M-plane GaN layers in order to determine the excitonic or band-to-band transition energies and to characterize the impurity states in the films. Figure 4.7 shows the PL spectra of the sample at 5 K. The spectra are dominated by strong near-band-edge transitions with the peak position for one of them at 3.484 named as (D^0,X) and at 3.350 eV (SF,X) for the other. No free excitonic transitions are visible in PL even at low temperatures. There are several possibilities for the absence of free exciton transition lines in PL for M-plane GaN sample. We list a few of them:

a) The unintentional background doping density in our films was measured to be around $5\times\ 0^{17}$ cm^{-3} at 295 K. Such high carrier concentration may screen the excitons. It is well known that as the doping density is increased the features in the PL spectra broaden. [95]

b) As revealed by the x-ray scan in Fig. 3.2, the reflection peak is larger than theoretically expected indicating a certain inhomogeneity in the strain distribution. This inhomogeneous strain distribution leads to high damping parameters for excitons as suggested by Syrbu *et al.* [96] Furthermore, the damping parameters in strained GaN are higher than the ones of unstrained layers. [95, 97, 98] It is, therefore, more difficult to resolve the free excitonic transition peaks for M-plane GaN.

Figure 4.7 also shows the PL spectra for two polarization directions for the luminescence. The spectra are measured for light polarized parallel to c ($\boldsymbol{E} \parallel \boldsymbol{c}$) and for perpendicular to c ($\boldsymbol{E} \perp \boldsymbol{c}$). For these measurements, the polarizer is kept between the monochromator and the sample. The intensity for $\boldsymbol{E} \perp \boldsymbol{c}$ is an order of magnitude

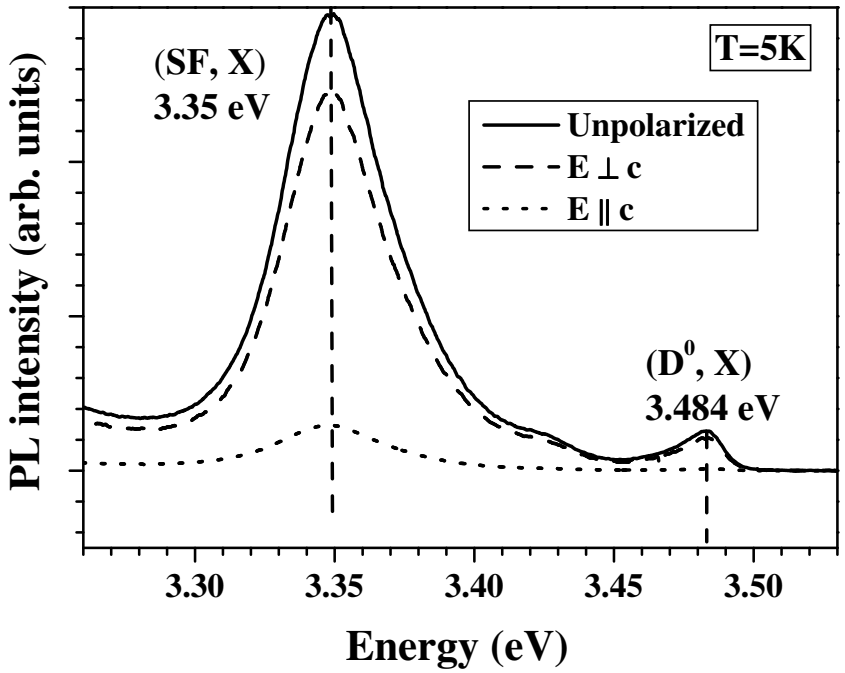

Figure 4.7: Photoluminescence spectrum of the 0.7 μm-thick *M*-plane GaN shown at 5 K using a He-Cd laser at 325 nm as the excitation source at 50 mW power. The near bandgap spectrum is dominated by two peaks, one at 3.350 eV, which is labelled as (SF,X), while the other is at 3.484 eV (D,X). The figure also shows the spectra for light polarized parallel ($\boldsymbol{E} \parallel \boldsymbol{c}$) and perpendicular to c ($\boldsymbol{E} \perp \boldsymbol{c}$). The polarizer for this measurement is kept between the monochromator and the sample collecting the luminescence and is rotated by 90° for the two polarizations. The dashed vertical lines show the peak positions of the two transitions.

higher than the one for $\boldsymbol{E} \parallel \boldsymbol{c}$. This can be explained as follows: At relatively low temperatures, the lower energy valence band state, which gives rise to the T_2 transition (cf. Fig. 4.6) will have lower occupation than the higher valence band state, which gives rise to the T_1 transition. Hence, the PL spectrum for $\boldsymbol{E} \perp \boldsymbol{c}$, giving rise to the T_1 transition, will have higher intensity as compared to the case when $\boldsymbol{E} \parallel \boldsymbol{c}$.

The higher energy band near 3.484 eV is attributed to donor-bound exciton (D^0,X). The blue shift of the (D^0,X) peak energy compared to relaxed GaN shown in Fig. 4.4, evidences the comparatively large compressive strain in the layers, [87, 97] consistent with the XRD results. A bound-state related emission located roughly 12 meV below the free exciton has been identified as neutral-acceptor bound exciton (A^0,X) [99, 100] or a neutral donor-bound exciton (D^0,X) [101] and more recently was assigned to an ionized donor-bound exciton (D^+,X). [102] The identification of donor-bound excitons is essential for the understanding of the role of defects in light emission. It is also important for the improvement of the device performance via shallower dopants and more efficient luminescence. The temperature dependence of the PL intensity of a bound exciton complex can be used to identify the kinetics of its thermal dissociation and thus provide a valuable insight into the origin of this complex. The main channel of thermal decay is the one with the least activation energy, E_A. In the case of a neutral donor-bound exciton complex in GaN, the exciton delocalization from neutral donors is likely to be the smallest energy dissociation channel of that complex. Temperature-dependent PL studies have been previously employed to investigate neutral donor-

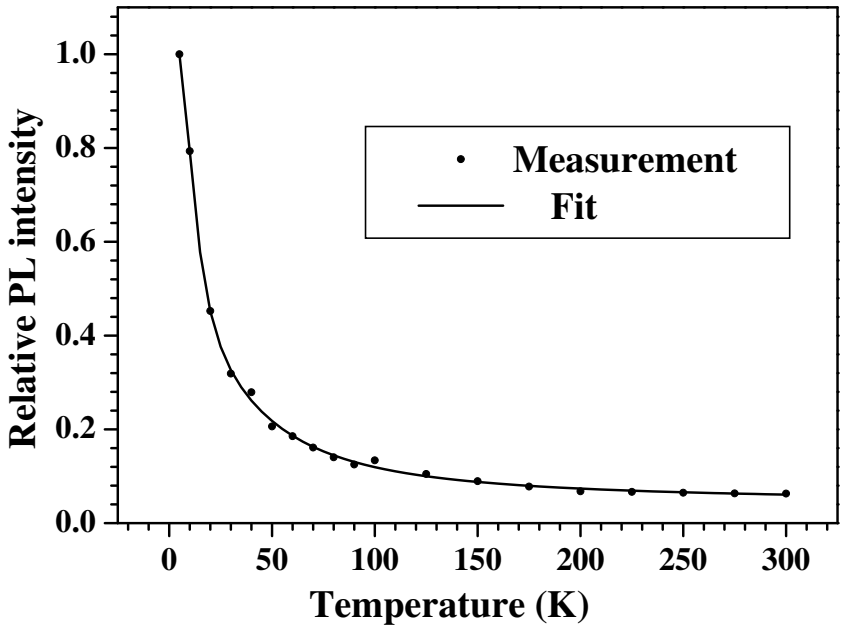

Figure 4.8: Temperature dependence of the PL intensity for donor-bound excitonic transition from 5 K to 300 K for the 0.7 μm-thick *M*-plane GaN film. The integrated intensity of the PL line is achieved by fitting a Gaussian line shape to the experimental data which are indicated as dots. The data is then fitted using an Arrhenius Model as outlined in Eq. (4.32) which is marked by solid line.

bound exciton emission in GaN and other materials. [103]

To access the temperature variation of the integrated intensity of the (D^0,X), all strong near-band edge lines corresponding to unpolarized emission have been fitted with Gaussian lineshapes. The low-energy tails of the (D^0,X) emission are disregarded during fitting. A two channel dissociation Arrhenius model is used to fit the temperature dependence of the PL integrated intensity of the (D^0,X) emission in the sample. The model is:

$$I(T) = \frac{I(0)}{1 + C_1 \exp\left(-E_1/kT\right) + C_2 \exp\left(-E_2/kT\right)}, \tag{4.32}$$

where E_1 and E_2 are activation energies for two dissociation processes, while C_1 and C_2 are constants. The results are shown in Fig. 4.8. The parameters achieved by fitting are as follows: E_1= 2.6 meV and E_2 = 14.8 meV. The results for the activation energy E_1 does not agree with the energy of exciton localization on a shallow donors, which should be E^X_{Loc} = 6 meV. [104] At higher temperatures, the other thermal dissociation channel with an activation energy of E_2 = 14.8 meV is observed. This second channel may be due to the decay of the (D^0,X) complex via simultaneous exciton delocalization and exciton dissociation. However, the energy for such a process should be around 30 meV. [104] A more detailed analysis of the exciton dynamics is required to determine, which channel governs the temperature dependence of the (D^0,X) emission at higher temperatures.

In addition to the (D^0,X) transitions, the spectra in Fig. 4.7 exhibit a lower energy line at 3.350 eV [named as (SF,X)]. Several groups have reported a weak PL line around 3.36 eV at low temperatures from *C*-plane GaN samples grown by different techniques

and on different substrates. [105, 106, 107, 108, 109, 110] The origin of this transition has mostly been attributed to excitons bound to structural defects such as stacking faults [108] or dislocations. [106, 107] Sun *et al.* [7] have done a detailed analysis of the origin of such a transition at around 3.356 eV in *M*-plane GaN in the low-temperature regime. They made use of SEM, cathodoluminescence, and transmission electron microscopy (TEM) to correlate the structural properties of these layers with the optical properties and came to the conclusion that the line (SF,X) is due stacking faults. One has to identify, whether the emission originates from point defects and impurities accumulated in the vicinity of SFs or an intrinsic emission such as related to exciton bound to SF. To determine the exact origin of the (SF,X) line, further analysis has to be carried out.

Figure 4.9 shows the excitation-density-dependent PL spectra for the 0.7 μm-thick *M*-plane GaN sample at 10 K in the near-bandgap spectral region. The (D^0,X) transition energy, as expected, is independent of the excitation density. Similarly, the peak position of the (SF,X) line does not change its energy position over 3 orders of magnitude of excitation intensity. This line thus exhibits the characteristics of an intrinsic transition. Grieshaber *et al.* [111] suggested a theoretical model for the dependence of the PL intensity of various transition channels as a function of the generation rate. The results exhibit power law dependency of the luminescence intensities I on the carrier generation rate G such that $I \propto G^i$, where i assumes the value of one for band-to-band transition for n-type semiconductor both in low-excitation and high-excitation regimes. This means that the luminescence intensity rises linearly with the excitation intensity. As pointed out by Sun *et al.*, [7] the intensity of the (SF,X) transition rises linearly with an increase in excitation intensity thus suggesting that this transition is intrinsic in nature. It is also noted that the (SF,X) transition quench rapidly, when the temperature is increased above 50 K. [5] At room temperature, this transition is hardly resolved. We can thus come to the conclusion that the PL line around 3.350 eV at 6 K is due to excitons bound to stacking faults.

Similarly, a further analysis of the spectra related to the donor-bound excitonic transition is necessary in order to obtain more insight into the nature of the transition. The peak energy position of the donor-bound excitonic transition ($E_{(D^0,X)}$) as a function of temperature is plotted in Fig. 4.10. The difference in the energy position of this transition between 6 K and 300 K, i.e., $E_{(F,X)}$(300 K)$-$ $E_{(D^0,X)}$(6 K) = 3.484 eV - 3.409 eV = 75 meV. This energy difference is larger than the one between the free excitonic transitions, where the difference is 68 meV [112], by around 7 meV. The donor-bound exciton dissociates around 100 K giving rise to a donor and a free exciton. Thus, at higher temperatures, one tends to see the free excitonic transitions. Furthermore, the strain, which changes the peak position for (D^0,X), is different at low temperatures as compared to 300 K due to difference in the thermal expansion coefficients. This may also be responsible for the higher difference.

An analytical expression, which has been frequently used for fitting the transition energy as a function of temperature for various semiconductors was first suggested by Varshni. [113] This takes the form

$$E(T) = E(0) - \frac{\alpha T^2}{\beta + T}. \tag{4.33}$$

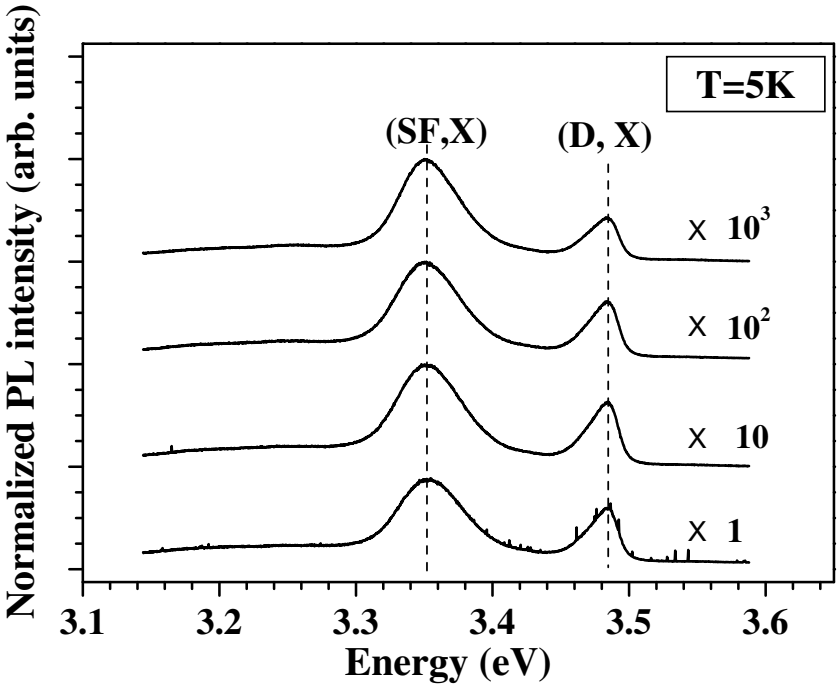

Figure 4.9: Excitation-density dependent PL spectra for the 0.7 μm-thick *M*-plane GaN film measured at 5 K. The peak position of both the (D,X) at 3.484 eV and (SF,X) at 3.350 eV does not change, when the excitation density is changed over 3 orders of magnitude.

In this model, the parameter α represents the magnitude of the limiting slope of the corresponding energy curve $E(T)$, and β is a physically undefinable parameter. Recently however, Pässler [114, 115, 116, 117] suggested a relatively simple, analytical, three-parameter expression of the form

$$E(T) = E(0) - \frac{\alpha\Theta}{2}[\sqrt[4]{1 + \frac{\pi^2}{6}(\frac{2T}{\Theta})^2 + (\frac{2T}{\Theta})^4} - 1]. \tag{4.34}$$

Here $\Theta = \hbar\omega/k_B$ is the effective (average) phonon temperature and the parameter α denotes the limiting slope, such that, $\alpha = -\frac{dE}{dT|_{T\to\infty}}$. We used this relation to fit the temperature dependence of the (D^0,X) line. Figure 4.10 shows the fit to the temperature dependence of energy, ($E_{(D^0,X)}$), using the Pässler relation [cf. Eq. (4.34)]. For comparison, a fit using the Varshni relation was also performed but it is not shown in the figure. The parameters thus achieved, using Eq. (4.34), are shown in Table 4.4. For comparison, we also provide the fit values achieved by Pässler [116], who analyzed a series of data sets available from published literature for the temperature dependence of the *A*- and the *B*- exciton peak positions associated with the fundamental band gap of *C*-plane GaN layers grown on sapphire. These values look similar except for the transition energy E_0 because we are fitting the energy dependence of bound excitons as opposed to free excitons in the case of Pässler. This transition energy depends on the strain in the film and is expected to be different for different samples depending on the substrate used and the film thickness. However, the application of the conventional model by Varshni, especially for temperatures $\leq$300 K, leads to large variation of the fit parameters, as shown by last two columns in Table 4.4. It is, therefore, advantageous to use Pässler's relation [Eq. (4.34)] as opposed to the empirical relation proposed by

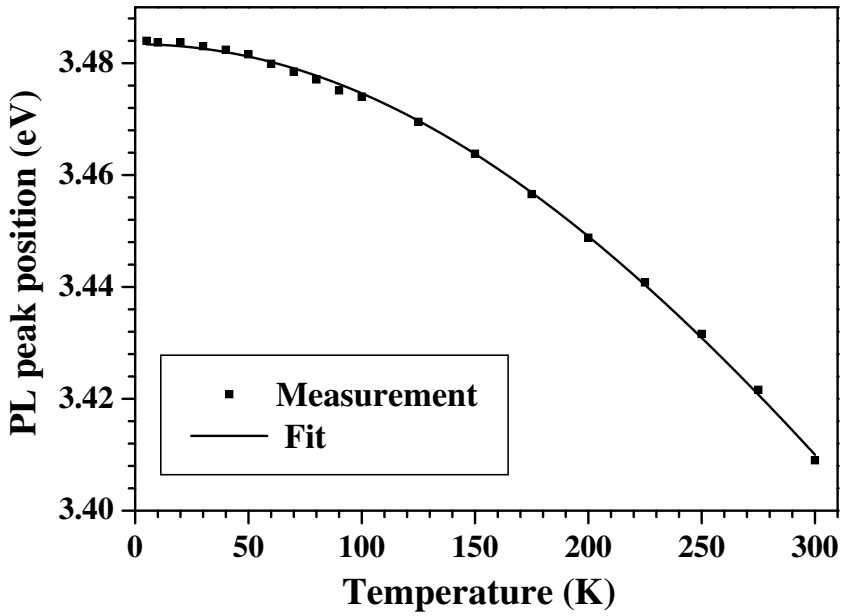

Figure 4.10: Temperature dependence of the peak position of the donor-bound exciton (D,X) peak measured for a 0.7 μm-thick M-plane GaN film. Eq. (4.34) is used to fit this temperature dependence to extract physically relevant parameters, which are $E(0)$=3.484 eV, $\alpha = 6.3 \times 10^{-4}$ eV/K, and Θ = 592 K. The measured peak positions are shown as points while the fit is indicated by a line.

Varshni [Eq. (4.33)]. The advantages of using Eq. (4.34) are discussed in detail in work by Pässler. [116]

Transmittance and Reflectance: Figure 4.11 displays the transmittance T at normal incidence and the reflectance R at near normal incidence for the wavelength range 350–650 nm measured at 295 K. Both quantities were measured for in-plane light polarization, $\boldsymbol{E} \parallel \boldsymbol{c}$ and $\boldsymbol{E} \perp \boldsymbol{c}$. Clear interference oscillations can be seen in reflectance and transmittance spectra in transparent regime below 3.4 eV. The shift between the interference oscillations seen for the two orthogonal polarizations is due to the difference between the value of the ordinary n_o (for $\boldsymbol{E} \perp \boldsymbol{c}$) and the extraordinary n_e (for $\boldsymbol{E} \parallel \boldsymbol{c}$) refractive index of GaN. Thus, the M-plane orientation of the film enables a measurement of n_e, which is more intricate for C-plane samples. This is because the c axis

Table 4.4: Empirical parameter values resulting from the fit to Eq. (4.34) of the data sets representing the temperature dependence of the exciton peak positions (associated with fundamental band gap) of hexagonal GaN layers. As a comparison, the values of the parameters obtained by the fit to Varshni's formula [Eq. (4.33)] is also given.

Reference	T_{range} (K)	$E(0)$ (eV)	$\alpha \times 10^4$ (eV/K)	Θ (K)	$\alpha_{varshni} \times 10^4$ (eV/K)	$\beta_{varshni}$ (K)
Our Results	10 to 300	3.484	6.3	592	15	1531
Ref. [118]	10 to 626	3.476	6.77	602	9.37	772
Ref. [119]	15 to 300	3.485	4.82	487	9.96	1072
Ref. [120]	110 to 300	3.490	6.24	630	24.3	2866
Ref. [121]	4 to 300	3.479	4.84	479	11	1200
Ref. [112]	15 to 475	3.482	6.39	569	9.77	842

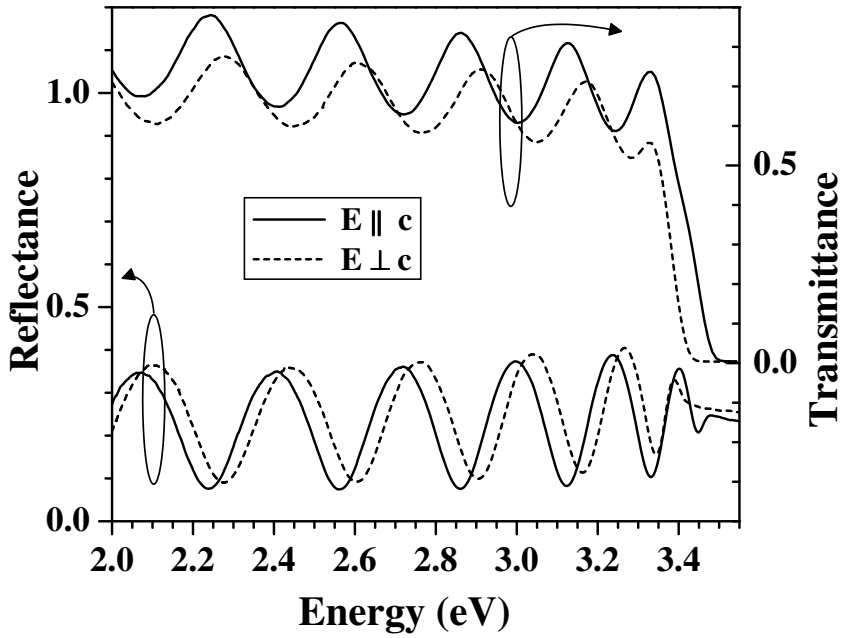

Figure 4.11: Polarization dependent near-normal incidence reflectance and normal incidence transmittance of a 0.7 μm-thick *M*-plane GaN film measured at 295 K for both the transparent and absorbing regime. The measurement is done for $\boldsymbol{E} \parallel \boldsymbol{c}$ and for $\boldsymbol{E} \perp \boldsymbol{c}$.

for *C*-plane GaN film is parallel to the growth direction and parallel to the direction of light propagation at normal incidence. [122, 123] For each polarization direction, the maxima (minima) of the fringe pattern in transmittance coincide with the minima (maxima) in reflectance indicating a phase change of 180° between them.

In addition to different refractive indices for two orthogonal polarization for *M*-plane GaN, the absorption coefficients are also different leading to different band gaps. This can be clearly seen in the *R* and *T* measured at 6 K as shown in Fig. 4.12 in the energy regime near the band gap. It shows a polarization-dependent shift in the damping of the interference oscillations in the reflectance spectra, which is associated with the onset of absorption. This onset is more pronounced in the transmittance spectra shown in the same figure. We observe a significant shift of the effective energy gap toward higher energies, when the light polarization is rotated from $\boldsymbol{E} \perp \boldsymbol{c}$ to $\boldsymbol{E} \parallel \boldsymbol{c}$. The results are similar for room temperature. The bandgap increases by 60 meV (50 meV) at 6 K (295 K). The larger separation at low temperatures may be due to a higher in-plane strain because of the larger thermal expansion coefficient mismatch between the substrate and the GaN layer at lower temperature as compared to room temperature. The nearly temperature-independent line shapes and the absence of sharp excitonic resonances in the absorption spectra is likely due to the dominance of inhomogeneous broadening related to the inhomogeneous strain distribution and the background doping density mentioned above. Therefore, the absence of free excitonic resonances in either reflectance or transmittance spectra is consistent with the PL measurements.

A polarization dependent refractive index for GaN suggest that the film exhibits linear birefringence (LB) . Additionally, different absorption coefficients α_e and α_o imply that the film exhibits linear dichroism (LD). Both linear birefringence and linear dichroism are expected because GaN is an anisotropic medium. A detailed study of

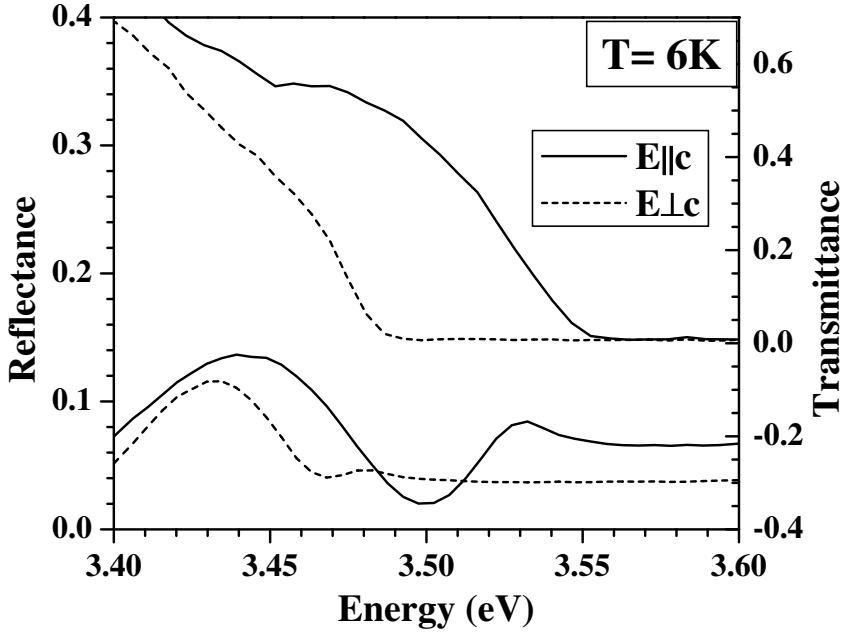

Figure 4.12: Near-normal incidence reflectance and normal incidence transmittance measured at 6 K for the 0.7 μm-thick *M*-plane GaN film. The experimental results are shown for $\boldsymbol{E} \parallel \boldsymbol{c}$ and $\boldsymbol{E} \perp \boldsymbol{c}$ for energy region near the bandgap of GaN.

both properties will be carried out in the next chapter.

Photoreflectance: Figure 4.13 displays PR spectra of the sample for both polariza-

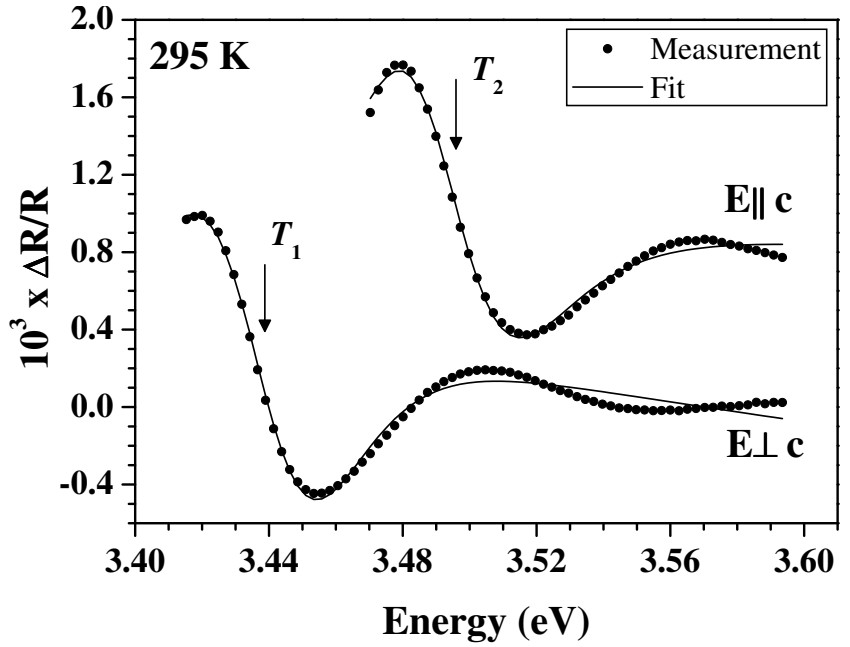

Figure 4.13: Photoreflectance spectra measured at 295 K for a 0.7 μm-thick *M*-plane GaN film for polarization of the probe beam $\boldsymbol{E} \parallel \boldsymbol{c}$ and $\boldsymbol{E} \perp \boldsymbol{c}$. The curve for $\boldsymbol{E} \parallel \boldsymbol{c}$ is shifted by 7×10^{-4} for clarity. The PR spectrum is fitted using the Aspnes' lineshape function with redefined parameters [55], to determine the corresponding transition energies yielding 3.437 eV, which corresponds to T_1 and 3.491 eV, which corresponds to T_2 transition. A clear shift in the transition energy can be seen going from $\boldsymbol{E} \parallel \boldsymbol{c}$ to $\boldsymbol{E} \perp \boldsymbol{c}$.

tions at 295 K. For each polarization, the spectra consist of a single resonance, whose energy depends on the polarization direction, just as in case of the absorption spectra (R and T). The nearly temperature-independent line shapes and the absence of sharp excitonic resonances in the absorption spectra is likely due to the reasons discussed above. To obtain the transition energies, we fit the spectra using Aspnes' line shape function.

$$\frac{\Delta R}{R} = \Re e[\frac{A\exp(i\Theta)}{(E - E_j + i\gamma)^m}], \tag{4.35}$$

with the exponent $m = 3$ representing a Gaussian-broadened excitonic transition. The fitting parameters A, E_j, γ, and Θ denote the amplitude, transition energy, broadening parameter, and phase factor, respectively. The energy achieved by fitting the above lineshape to the experimental data is E=3.437 eV for $\boldsymbol{E} \perp \boldsymbol{c}$, while E= 3.491 eV for $\boldsymbol{E} \parallel \boldsymbol{c}$. The difference in the energy is around 54 meV, which is consistent with the transmittance results.

Discussion: The XRD measurement show that the M-plane GaN film is under compressive strain with ϵ_{yy}= 0.422% [cf. Fig. (3.2)]. Keeping this in mind and comparing the PR results depicted in Fig. 4.6 with the calculated oscillator strength components in Chapter 2, we identify the lowest energy PR feature seen for $\boldsymbol{E} \perp \boldsymbol{c}$ as the T_1 transition associated with a predominantly $|X\rangle$-like VB state. The high energy feature seen for $\boldsymbol{E} \parallel \boldsymbol{c}$ is identified as the T_2 transition associated with the $|Z\rangle$-like VB state. The in-plane strain components ϵ_{xx} and ϵ_{zz} of the sample, for which E_1= 3.437 eV and E_2= 3.491 eV, are ϵ_{xx}=−0.77% and ϵ_{zz}=−0.47%. These in-plane strain values are used to calculate the out-of-plane strain and give the value ϵ_{yy}=0.41% using Poisson's relation. This value of ϵ_{yy} is nearly the same as the one obtained from the XRD measurement. However, these in-plane strain values are inconsistent, because the maximum value of the in-plane strain along the c axis is the lattice mismatch between GaN and $LiAlO_2$ which should be −0.31% according to:

$$\frac{a_{\mathrm{LiAlO_2}} - c^r_{\mathrm{GaN}}}{c^r_{\mathrm{GaN}}} = \frac{5.1687\text{Å} - 5.1846\text{Å}}{5.1846\text{Å}} = -0.31\%, \tag{4.36}$$

where c^r_{GaN} denotes the relaxed lattice constant of GaN along the c-direction while $a_{\mathrm{LiAlO_2}}$ is the lattice constant of γ-$LiAlO_2$ along this direction (cf. Tab. 2.1). Negative sign for the mismatch denotes compressive strain. The lattice mismatch is calculated taking the lattice constants for $LiAlO_2$ from Ref. [45].

Although the maximum of the strain along the z axis is ϵ_{zz}=$|-0.31\%|$ comparing the values of the lattice constant for GaN and $LiAlO_2$ from literature, we find that this value is −0.47% by calculating the in-plane strain from the transition energies at 295 K. Let us suppose that the maximum value of ϵ_{zz} is $|-0.5\%|$ instead of $|-0.31\%|$. We chose the value of the compressive strain to be 0.5% so as to be consistent with the result achieved using the transition energies. We calculate the lattice constant for the substrate using this strain value:

$$\begin{aligned} \frac{a_{LiAlO_2} - c^r_{\mathrm{GaN}}}{c^r_{\mathrm{GaN}}} &= \frac{a_{LiAlO_2} - 5.1846\text{Å}}{5.1846\text{Å}} = -0.5\% \\ \Rightarrow a_{\mathrm{LiAlO_2}} &= 5.1587\text{Å}. \end{aligned} \tag{4.37}$$

The difference between the lattice constant calculated above with the value in literature, [45] amount to an error of 0.2% [(5.1687-5.1587)/5.1687]. One suspects that such an error can easily occur in the measurement of the lattice coefficient of γ-$LiAlO_2$. Unfortunately, we cannot independently measure the lattice constant of the substrate. We attribute the ambiguity in the results to this fact. Additional source of error can be the deformation potential for GaN which has a large scatter in literature and more consistent values of deformation potential D_5 is needed. In order to resolve the inconsistency, we need to do PR measurements at low temperatures to determine the exact transition energies of *M*-plane GaN.

Although a polarization-dependent, effective band-gap change is in principle possible for unstrained GaN as discussed before in Chapter 2, the polarization properties of the features seen here together with their energies can only be explained by including the effect of *M*-plane biaxial compressive strain on the EBS of GaN. Also note that for unstrained GaN or for compressively strained *C*-plane GaN the band-gap change would involve the lowest (*A*-exciton) and highest (*C*-exciton) energy transitions, while here it involves the lowest (T_1) and next higher (T_2) energy transition. In our case for PR, it is not possible to observe the highest energy (E_3) transition to the $|Y\rangle$-like VB (expected at 3.58 eV), since a sizeable $\boldsymbol{E}\|\boldsymbol{y}$ polarization is not achievable with an *M*-plane film under normal incidence. We find that with the values of in-plane strain as observed in our samples the transition T_1 is completely $|x\rangle$-polarized while T_2 is completely $|z\rangle$-polarized. The oscillator strength contribution to the T_3 transition is negligible.

4.2.3 *A*-plane GaN films

We now focus on the optical characterization of *A*-plane GaN grown on *R*-plane sapphire. Both the transmittance and photoreflectance measurements are done at 295 K.

Transmittance: The polarized transmittance of the *A*-plane GaN film recorded at 295 K, is shown in Fig. 4.14 for the electric vector $\boldsymbol{E}$ oriented $\|$ and $\perp$ to $\boldsymbol{c}$. The transmittance spectrum for $\boldsymbol{E} \parallel \boldsymbol{c}$ is clearly shifted to higher energies by about 10 meV in comparison to the spectrum for $\boldsymbol{E} \perp \boldsymbol{c}$. The transmittance spectra shows that *A*-plane GaN on *R*-plane sapphire is also an anisotropic medium, since the transmittance depends on the polarization of light. The optical response of *A*-plane GaN is similar to *M*-plane GaN film on $LiAlO_2$, where the bandgap for $\boldsymbol{E} \parallel \boldsymbol{c}$ is also larger than for $\boldsymbol{E} \perp \boldsymbol{c}$. However, the difference in the energy gap, estimated from the transmittance, is much less than that for *M*-plane GaN film on γ-$LiAlO_2$. For the *M*-plane case, this difference was around 50 meV at room temperature compared to 10 meV in this case. This is because, the in-plane strain for this *A*-plane film is much smaller than the *M*-plane film studied above. We discuss the effect of strain on the band gap for *A*-plane film in detail below.

Photoreflectance: The polarized PR spectra of the *A*-plane GaN film recorded at 295 K are shown in Fig. 4.15 for the electric vector $\boldsymbol{E}$ oriented $\|$ and $\perp$ to $\boldsymbol{c}$. The PR spectra in Fig. 4.15 have been fitted using Aspnes' lineshape function [124] with Gaussian-broadened excitonic transitions, which are expected at higher temperatures.

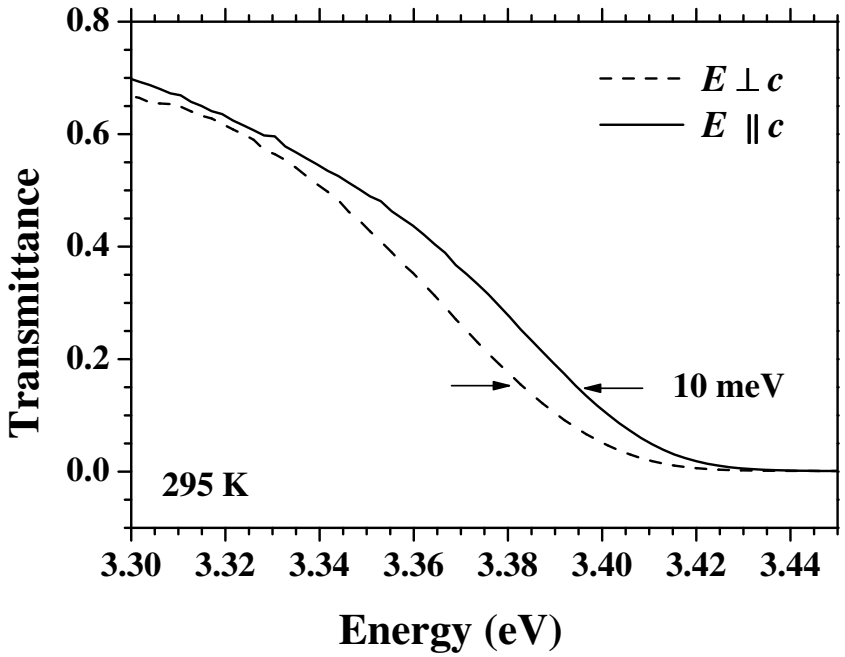

Figure 4.14: Measured transmittance for a 1 μm-thick A-plane GaN film for $\boldsymbol{E} \perp \boldsymbol{c}$ and $\boldsymbol{E} \parallel \boldsymbol{c}$ measured at 295 K.

The PR spectrum for $\boldsymbol{E} \perp \boldsymbol{c}$ in Fig. 4.15 can be fitted with a single feature. If we fit the PR spectrum for $\boldsymbol{E} \parallel \boldsymbol{c}$ to a single transition, the line width is about 60% larger than the one for the transition observed for E $\perp$ c. At the same time, in order to obtain a good fit to the observed PR spectrum for $\boldsymbol{E} \parallel \boldsymbol{c}$, we have to use two transitions with energies higher than the one for $\boldsymbol{E} \perp \boldsymbol{c}$. We therefore conclude that the PR spectrum for $\boldsymbol{E} \perp \boldsymbol{c}$ can be described by a single transition, while for $\boldsymbol{E} \parallel \boldsymbol{c}$ two transitions are necessary. The obtained transition energies are 3.432 eV for $\boldsymbol{E} \perp \boldsymbol{c}$ and 3.441 as well as 3.457 eV for $\boldsymbol{E} \parallel \boldsymbol{c}$ with an error of $\pm$3 meV. Thus, the effective energy gap of the A-plane GaN film increases by about 9 meV, when the polarization of the light is rotated by 90°. from $\boldsymbol{E} \perp \boldsymbol{c}$ to $\boldsymbol{E} \parallel \boldsymbol{c}$. This shift agrees with the one observed in the transmittance spectra.

Discussion: We would like to discuss the experimental results in conjunction with the energy dependence on in-plane strain calculated in Chapter 2 using the $\mathbf{k}\cdot\mathbf{p}$ perturbation technique. Figure 4.16(a) presents the out-of-plane strain ϵ_{xx}, calculated as a function of the in-plane strain ϵ_{yy} and ϵ_{zz} using Poisson's relation. (cf. Chapter 2) The dotted line in Fig. 4.16(a) denotes the out-of-plane strain ϵ_{xx}= 0.09%, calculated by high-resolution XRD, the results of which were presented in the last chapter. Figures 4.16(b), 4.16(c), and 4.16(d) present the calculated energies vs. ϵ_{yy} and ϵ_{zz} for the three transitions T_1, T_2, and T_3, respectively. The contours marked by the dotted line correspond to the measured PR transition energies. Using these figures we interpret the PR results in the following way. If we identify the PR feature lowest in energy at 3.432 eV with the T_1 transition, we derive from Figs. 4.16(a) and 4.16(b) that the value of our measured out-of-plane strain component ϵ_{xx} = 0.09% intersects the energy E_1 = 3.432 eV for two in-plane strain coordinates ϵ_{yy} = 0.05% and $\epsilon_{zz} = -0.39\%$ as well as $\epsilon_{yy} = -0.05\%$ and $\epsilon_{zz} = -0.26\%$. For the first set of strain coordinates, the calculated energies for the transitions T_2 and T_3 are E_2 = 3.444 eV and E_3 = 3.457 , while for the

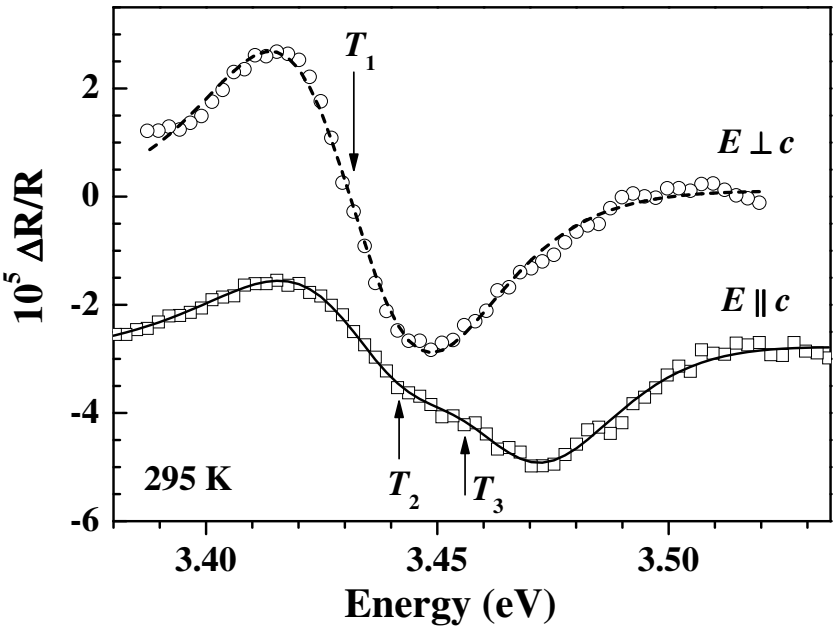

Figure 4.15: Measured PR spectra (circles and squares) of the 1 μm-thick A-plane GaN film for $\boldsymbol{E} \perp \boldsymbol{c}$ and $\boldsymbol{E} \parallel \boldsymbol{c}$ measured at 295 K. The curve for $\boldsymbol{E} \parallel \boldsymbol{c}$ is shifted by -3×10^{-5} for clarity. The dashed line for $\boldsymbol{E} \perp \boldsymbol{c}$ represents a fit to a single transition with an Aspnes' lineshape function at 3.432 eV, which corresponds to T_1. The solid line for $\boldsymbol{E} \parallel \boldsymbol{c}$ is obtained by fitting two transitions with Aspnes' lineshape functions at energies 3.441 and 3.457 eV, which correspond to transitions T_2 and T_3.

second set they are E_2 = 3.438 eV and E_3 = 3.454 eV. From these energy values alone, we cannot distinguish between the two sets of in-plane strain components. In order to unambiguously identify the strain values, we have to determine the oscillator strength of the three transitions T_1, T_2, and T_3.

As discussed above, we should be able to take the calculated oscillator strength from Ref. [55] and exchange x and y assuming that the oscillator strength is only weakly temperature dependent. We have checked this symmetry by performing the calculation for A-plane GaN films. The relative oscillator strength components $f_{i\beta}$, where i = 1, 2, 3, correspond to the three transitions T_1, T_2, and T_3, while $\beta = x$, y, and z are the three components along the x, y, and z direction that determine the optical polarization selection rules, are plotted in Fig. 4.17 as a function of A-plane strain. The energy and polarization properties of T_1, T_2, and T_3 at zero strain are identical to the ones of the A-, B-, and C-excitons. Note that the x-polarization is not accessible with a normally incident beam on an A-plane film. These plots clearly demonstrate that only for the in-plane strain values $\epsilon_{yy} = -0.05\%$ and $\epsilon_{zz} = -0.26\%$ the oscillator strength of the T_1 transition is significant for y polarization ($\boldsymbol{E} \perp \boldsymbol{c}$) and negligible for z-polarization ($\boldsymbol{E} \parallel \boldsymbol{c}$). In addition, the T_2 and T_3 transitions exhibit appreciable oscillator strengths only for the z polarization and not for the y polarization, in agreement with the measured polarization dependence of the PR spectra. Therefore, only the calculated transition energies together with the calculated oscillator strengths allow for an unambiguous identification of the in-plane strain components for the A-plane GaN film. Note that the exact values of the deformation potentials are still under investigation. Hence, the values of the calculated transition energies and oscillator strengths

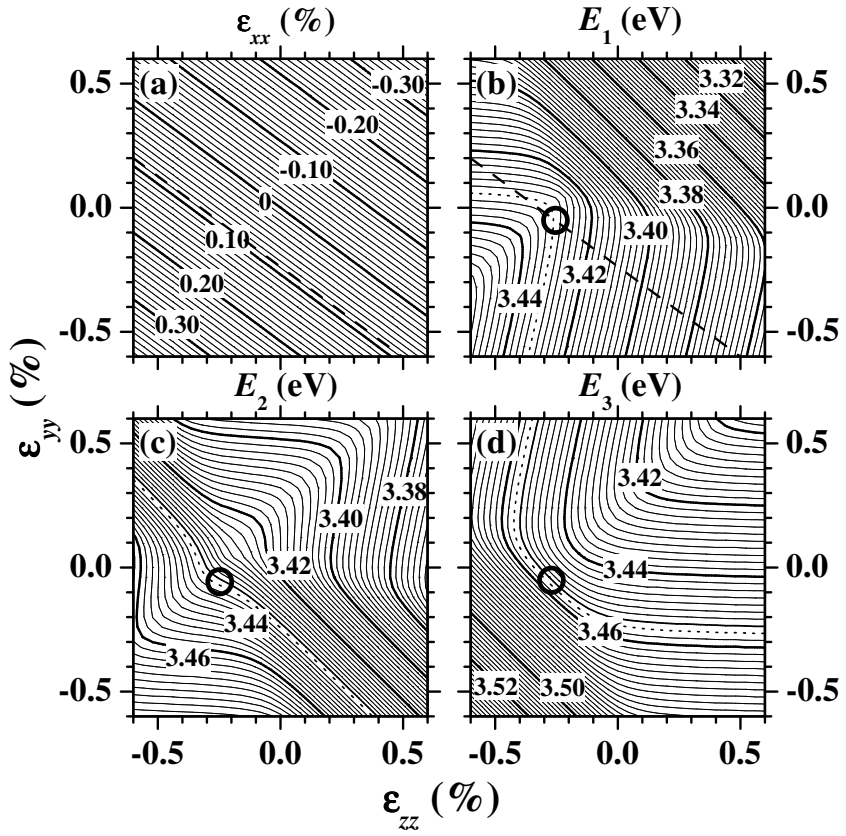

Figure 4.16: Contour plots showing the variation (a) in the out-of-plane strain ϵ_{xx}, (b) in the energy E_1 of the transition T_1, (c) in the energy E_2 of the transition T_2, and (d) in the energy E_3 of the transition T_3 as a function of in-plane strain ϵ_{yy} and ϵ_{zz} in the A plane of GaN. The dashed lines in (a) and (b) trace the contour of ϵ_{xx}= 0.09%. The dotted lines in (b), (c), and (d) indicate the measured transition energies. The circles in (b), (c), and (d) mark the in-plane strain coordinates $\epsilon_{yy} = -0.05\%$ and $\epsilon_{zz} = -0.26\%$, which are identified as being present in the investigated film.

may change somewhat, but the overall strain dependence and the resulting agreement with our experimental data will not be significantly affected.

4.3 Summary

In this chapter we have determined the transition energies for *C*-plane GaN film on GaN template and *A*-plane GaN thin film on *R*-plane sapphire. Additionally, a detailed investigation of the optical properties for *M*-plane GaN film on γ-$LiAlO_2$ is done. The obtained transition energies and the in-plane polarization properties are explained by taking into account the in-plane strain in the films. The experimentally determined transition energies are matched with the calculations based on $\mathbf{k}\cdot\mathbf{p}$ perturbation approach in Chapter 2. We find that the experimental results for *C*- and *A*-plane GaN thin films can be successfully explained with help of the theoretical calculation. For our case of 0.7 μm-thick *M*-plane GaN film, the polarization properties can be explained taking into account the anisotropic in-plane strain. The transmittance, reflectance and PR measurement suggest that there is a single transition for $\boldsymbol{E}\perp\boldsymbol{c}$ arising from the topmost VB state and another single transition for $\boldsymbol{E}\|\boldsymbol{c}$ from the second-highest VB state. The difference between these two VB state is 50 meV at 295 K. However, the maxi-

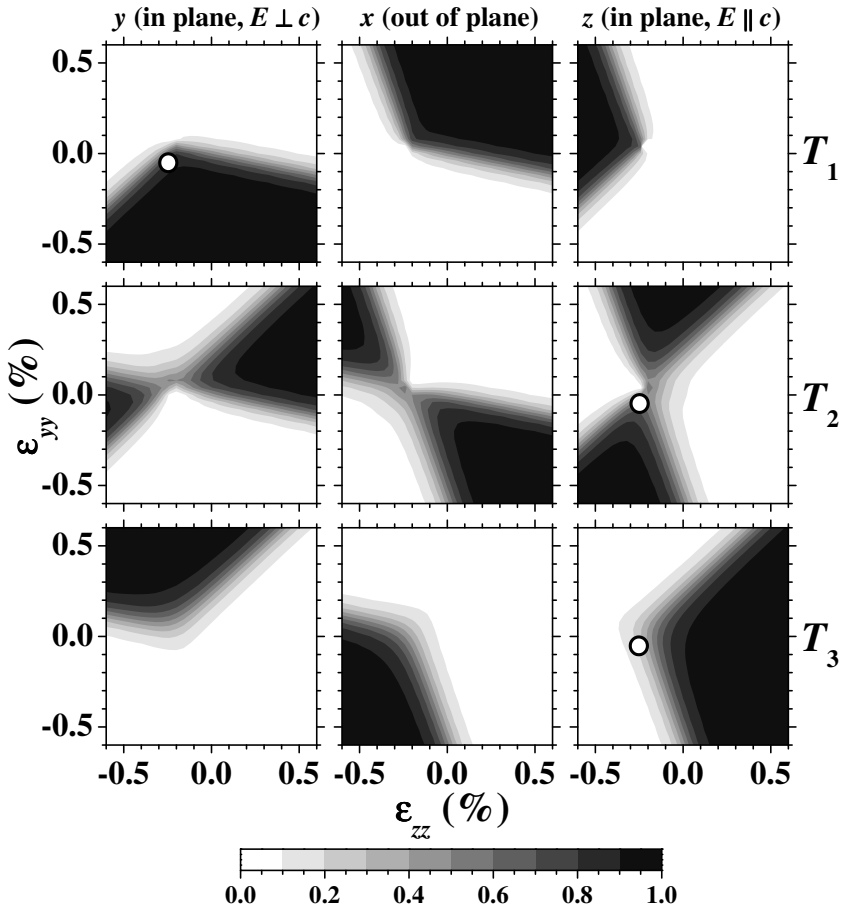

Figure 4.17: Relative magnitudes $f_{i\beta}$ ($i = 1, 2, 3$ and $\beta = x, y, z$) representing the oscillator strengths for the three transitions T_1, T_2, and T_3 as a function of in-plane strain ϵ_{yy} and ϵ_{zz} for A-plane GaN. T_1 (T_3) is defined as the transition with the lowest (highest) transition energy for a given in-plane strain value. The circles mark the in-plane strain coordinates $\epsilon_{yy} = -0.05\%$ and $\epsilon_{zz} = -0.26\%$, which are identified as being present in the investigated film.

mum value of the in-plane strain ϵ_{zz} exceeds the values obtained from literature. This ambiguity can be due to the inaccurate value of the lattice constants for the substrate.

Chapter 5

Polarization anisotropy in *M*-plane GaN thin films

5.1 Electromagnetic wave propagation in layered media

The reflection and refraction of an electromagnetic wave at a planar interface between two media with different dielectric properties is a familiar problem. The plane wave incident on the interface will in general be split into two waves: a transmitted wave proceeding into the second medium and a reflected wave propagating back into the first medium. The plane wave with wavevector $\mathbf{K}_1$ and frequency ω is incident from the medium 1. The transmitted and reflected waves have wavevectors $\mathbf{K}_2$ and $\mathbf{K}_1^{'}$, respectively, where 2 denotes the second medium. The coordinate system is chosen in such a way that the yz plane denotes the plane of incidence and the interface is located at $y = 0$. Maxwell's equations were solved in Chapter 4 and the general solutions were presented. Here, we write the general solution, as a superposition of the incident and the reflected waves in each medium:

$$(\mathbf{E}_1 e^{-\mathbf{K}_1 \cdot \mathbf{r}} + \mathbf{E}_1^{'} e^{-\mathbf{K}_1^{'} \cdot \mathbf{r}}) e^{i\omega t}, y < 0 \tag{5.1}$$

$$(\mathbf{E}_2 e^{-\mathbf{K}_2 \cdot \mathbf{r}} + \mathbf{E}_2^{'} e^{-\mathbf{K}_2^{'} \cdot \mathbf{r}}) e^{i\omega t}, y > 0 \tag{5.2}$$

where $\mathbf{K}_2^{'}$ is defined in such a way that the y-component of the wavevector $\mathbf{K}_2$ is same as that of $\mathbf{K}_2^{'}$, i.e., $K_{2y} = K_{2y}^{'}$. Similar equations as above can be written for the magnetic field vector $\mathbf{H}$. The boundary conditions on the tangential components of the electric and the magnetic field vectors require that E_z, E_x, H_z, and H_x be continuous at the interface y=0. In applying these boundary conditions, it is convenient to split each vector into components parallel (p) and perpendicular (s) to the plane of incidence. As long as the media 1 and 2 are isotropic and homogeneous, the two components s and p can be shown to be independent of each other, such that s (p) maintains its s (p) character in reflection and transmission. However, we will consider the reflection and refraction of an electromagnetic wave at normal incidence in an isotropic medium, so the distinction between s or p wave is lifted. Imposing the continuity of E_x and H_z at the interface and assuming that the material is nonmagnetic (μ=1) leads to:[125]

$$\begin{aligned} E_1 + E_1^{'} &= E_2 + E_2^{'} \\ \sqrt{\epsilon_1}(E_1 - E_1^{'}) &= \sqrt{\epsilon_2}(E_2 - E_2^{'}) \, , \end{aligned} \tag{5.3}$$

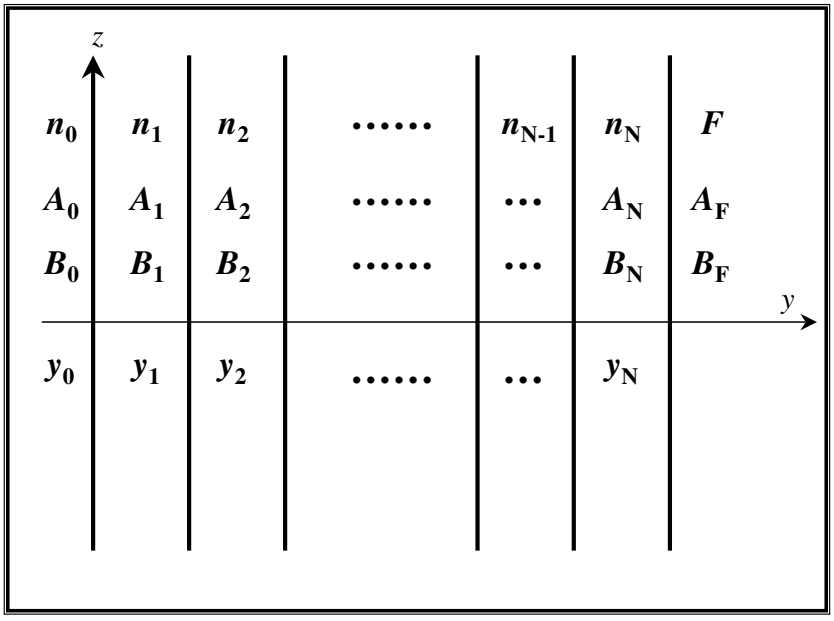

Figure 5.1: A multilayered dielectric medium

The two relations in Eq. (5.3) can be written as a matrix equation:

$$D(1)\begin{pmatrix} E_1 \\ E_1' \end{pmatrix} = D(2)\begin{pmatrix} E_2 \\ E_2' \end{pmatrix} , \tag{5.4}$$

where

$$D(i) = \begin{pmatrix} 1 & 1 \\ \sqrt{\epsilon_i} & -\sqrt{\epsilon_i} \end{pmatrix} \quad . \tag{5.5}$$

The matrix $D(i)$ is called the dynamical matrix for the medium i (i=1,2). This is the situation for a single interface. However, when the number of layers become too large, it is easier to use matrix method, which is a systematic approach for solving reflection and transmission at multiple interfaces.[125]

5.1.1 Matrix formulation for isotropic layered media

Let us now consider a multilayer structure such as the one shown in Fig. 5.1. The complex refractive index of such a structure is defined as follows:

$$\begin{aligned} n(y) = n_0 \quad &\text{for} \quad y < y_0 \\ n_1 \quad &\text{for} \quad y_0 < y < y_1 \\ n_2 \quad &\text{for} \quad y_1 < y < y_2 \\ n_3 \quad &\text{for} \quad y_2 < y < y_3 \\ \vdots \quad &\quad \vdots \\ n_N \quad &\text{for} \quad y_{N-1} < y < y_N \\ n_F \quad &\text{for} \quad y_N < y \, , \end{aligned}$$

where n_0, n_l, and n_F are the refractive indices of the incident medium, the l^{th} layer and the final medium, respectively. y_l is the position of the interface between the l^{th} and the $(l+1)^{th}$ layer while the initial and the final medium are described as the 0^{th} and the F^{th} medium, respectively. The whole medium is homogeneous in the z direction (i.e., $\frac{\delta n}{\delta z}$= 0). Further, we assume that the electromagnetic wave is propagating in the yz plane, and will take the case of normal incidence. The system can therefore, be simplified from 3 dimensions to 2 dimensions, and electric field vector can be written as: $\mathbf{E}(y,z,t)$ = $\mathbf{E}(y)$exp[i(ωt-βz)][126] where β is the z-component of the propagation vector. The distribution of the electric field, $E(y)$ as a function of position can be written as:

$$E(y) = \begin{cases} A_0 e^{-iK_{0y}(y-y_0)} + B_0 e^{iK_{0y}(y-y_0)} & , \quad y < y_0 \, , \\ A_l e^{-iK_{ly}(y-y_l)} + B_l e^{iK_{ly}(y-y_l)} & , \quad y_{l-1} < y < y_l \, , l = 1, ..., N \, , \\ A_F e^{-iK_{Fy}(y-y_F)} + B_F e^{iK_{Fy}(y-y_F)} & , \quad y_N < y \, , \end{cases}$$

where A_l and B_l represent the amplitude of the plane wave at interface $y = y_l$, travelling to right and left, respectively, and K_{ly} is the y component of the wave vector and is related to the refractive index of the medium

$$K_{ly} = n_l \frac{\omega}{c} \, . \tag{5.6}$$

If we represent the two amplitudes as column vectors, the amplitude of the electric field at $y < y_0$ is related to the ones at $y_0 < y < y_1$ as follows:

$$\begin{pmatrix} A_0 \\ B_0 \end{pmatrix} = D_0^{-1} D_1 \begin{pmatrix} A_1 \\ B_1 \end{pmatrix} \, , \tag{5.7}$$

while the amplitudes for $(l-1)^{th}$ and l^{th} layer are related by:

$$\begin{pmatrix} A_{l-1} \\ B_{l-1} \end{pmatrix} = D_{l-1}^{-1} D_l P_l \begin{pmatrix} A_l \\ B_l \end{pmatrix} \, , \quad l = 1, 2, ..., N. \tag{5.8}$$

D_l is the dynamical matrix described in Eq. (5.5), and can be written as:

$$D_l = \begin{pmatrix} 1 & 1 \\ n_l & -n_l \end{pmatrix} \, , \tag{5.9}$$

and the propagation matrix P_l is defined as:

$$P_l = \begin{pmatrix} e^{i\phi_l} & 0 \\ 0 & e^{-i\phi_l} \end{pmatrix} \, , \tag{5.10}$$

where $\phi_l = K_{ly} d_l$ and d_l is the thickness of l^{th} layer given by $d_l = y_{l+1} - y_l$. P_l is the matrix which introduces a phase delay after transmission through a layer. If there are N number of layers between initial medium labelled 0 and the final medium labelled F, the matrix, which relates $A(0)$ and $A(F)$, is given by

$$\begin{pmatrix} A_0 \\ B_0 \end{pmatrix} = T_{0,1} T_{1,2} T_{2,3} ..... T_{N-1,N} T_{N,F} \begin{pmatrix} A_F \\ B_F \end{pmatrix} \, , \tag{5.11}$$

where $F = N + 1$ and d_{N+1}=0 and $T_{l-1,l}$= $D_{l-1}^{-1} D_l P_l$

The relation between the initial and the final electric field amplitudes is given by:

$$\begin{pmatrix} A_0 \\ B_0 \end{pmatrix} = \mathbb{M} \begin{pmatrix} A_F \\ B_F \end{pmatrix} = \begin{pmatrix} M_{11} & M_{12} \\ M_{21} & M_{22} \end{pmatrix} \begin{pmatrix} A_F \\ B_F \end{pmatrix} , \tag{5.12}$$

with the matrix $\mathbb{M}$ given by

$$\mathbb{M} = T_{0,1}T_{1,2}T_{2,3}.....T_{N-1,N}T_{N,F} = D_0^{-1}\left[\prod_{l=1}^{N} D_l P_l D_l^{-1}\right] D_F \, . \tag{5.13}$$

Using the 2×2 matrix method described above, one can discuss the reflectance and transmittance of plane waves through a multi-layered dielectric structure. For light incident from the initial medium labelled 0 and with the assumption that the final medium is semi-infinite, i.e., there is no left travelling wave in the final medium so $B_F = 0$. The reflection and transmission coefficients are defined as:

$$\begin{aligned} r &= \left(\frac{B_0}{A_0}\right)_{B_F=0} , \\ \text{Using Eq. (5.12) we achieve} &= \left(\frac{M_{21}}{M_{11}}\right) \end{aligned} \tag{5.14}$$

and

$$\begin{aligned} t &= \left(\frac{A_F}{A_0}\right)_{B_F=0} , \\ \text{Using Eq. (5.12) we achieve} &= \left(\frac{1}{M_{11}}\right) . \end{aligned} \tag{5.15}$$

The reflectance is give by $R = |r|^2$ and for the case, when the initial and the final medium are both air, the transmittance is $T = |t|^2$.

However, if the light is incident from the right side (medium F) at the same angle, A_0=0 as there is no right-travelling wave in the initial medium for this case. Let $r^{'}$ and $t^{'}$ be the reflection and transmission coefficient given by:

$$\begin{aligned} r^{'} &= \left(\frac{A_F}{B_F}\right)_{A_0=0} = -\left(\frac{M_{12}}{M_{11}}\right) , \\ t^{'} &= \left(\frac{B_0}{B_F}\right)_{A_0=0} = \left(\frac{|\mathbb{M}|}{M_{11}}\right) , \end{aligned} \tag{5.16}$$

where $|\mathbb{M}|$ is the determinant of matrix $\mathbb{M}$. To illustrate the use of the matrix method, let us consider the case of a single, homogeneous thin film with index n and thickness d, in air. So from Eq. (5.13) we have, $\mathbb{M} = D_{\text{air}}^{-1} D_{\text{film}} P_{\text{film}} D_{\text{film}}^{-1} D_{\text{air}}$. The individual elements

of the matrix M_{ij} are:

$$M_{11} = \cos(\phi) + \frac{1}{2} i \sin(\phi) \left(n + \frac{1}{n} \right) ,$$
$$M_{12} = \frac{1}{2} i \sin(\phi) \left(n - \frac{1}{n} \right) ,$$
$$M_{21} = -\frac{1}{2} i \sin(\phi) \left(n - \frac{1}{n} \right) ,$$
$$M_{22} = \cos(\phi) - \frac{1}{2} i \sin(\phi) \left(n + \frac{1}{n} \right) , \tag{5.17}$$

where $\phi = \frac{2\pi n d}{\lambda}$. The matrix elements satisfy $M_{12} = M_{21}^*$ and $M_{22} = M_{11}^*$, provided that n is real. $*$ indicates complex conjugation. The matrix $\mathbb{M}$, for such a case, can be written as

$$\mathbb{M} = \begin{pmatrix} 1/t & r^*/t^* \\ r/t & 1/t^* \end{pmatrix} . \tag{5.18}$$

Although we have derived the above result for a single layer, it can be proved that Eq. (5.18) also holds true for a multilayered system. Therefore, calculating the transmission and reflection coefficients using the matrix approach is straightforward, since it is a matter of matrix multiplication.

Let us now turn our attention to a practical example, where the system consists of a thin film (GaN for our case) on a thick substrate. For such a system, the number of layers are two (both the thin film and the substrate), while the initial (0^{th}) and the final [$F = (n+1)^{th}$] medium is air. We can relate the amplitudes of the plane wave before the system (A_0, B_0) to the final amplitudes (A_F, B_F) using the relations in Eqs. (5.12) and (5.13), where $N = 2$. If the system consists of a thick layer, for example, a substrate which is more than several wavelengths thick and sufficiently transparent, narrow Fabry-Perot oscillations may occur in the reflectance R and transmittance T. The Fabry-Perot oscillation are usually not resolved in the measurements, because d_s is very large. Furthermore, the assumptions for the model calculations such as plane and parallel surfaces and monochromatic light source are not realistic. We can derive a much simpler formula using the procedure outlined by Harbecke [127] to turn off the interference within a thick layer based on the idea of coherent and incoherent multiple reflections. The thick substrate destroys coherence between the medium to its right and left. So instead of using individual elements of the complete matrix, we can write the matrix in such a form that we can easily turn off coherence between the single reflected amplitudes taking the absolute values of the complex coefficients t and r. Since the thick substrate needs special treatment, we divide the substrate into two parts as shown in Fig. 5.2:
a) One part relates the electric field vector as it enters the thick incoherent substrate, A_2^-, B_2^-, with the electric field vector in the initial medium, A_0, B_0.

$$\begin{pmatrix} A_0 \\ B_0 \end{pmatrix} = \begin{pmatrix} 1/t_1 & r_1^*/t_1^* \\ r_1/t_1 & 1/t_1^* \end{pmatrix} \begin{pmatrix} A_2^- \\ B_2^- \end{pmatrix} , \tag{5.19}$$

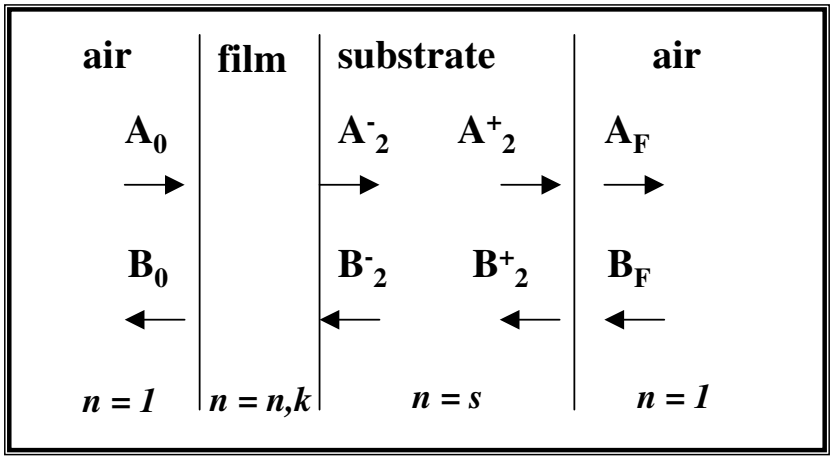

Figure 5.2: A schematic diagram of a thin film on a substrate. The analysis for the substrate is divided into two regimes with the electric field is defined: a) at the film-substrate interface on the substrate side b) at the substrate-air interface before exiting the substrate.

b) The second part relates the electric field vector as it exits the thick incoherent substrate, A_2^+, B_2^+, with the electric field vector in final medium, A_F, B_F.

$$\begin{pmatrix} A_2^+ \\ B_2^+ \end{pmatrix} = \begin{pmatrix} 1/t_2 & r_2^*/t_2^* \\ r_2/t_2 & 1/t_2^* \end{pmatrix} \begin{pmatrix} A_F \\ B_F \end{pmatrix} , \tag{5.20}$$

For the case of normal incidence and when the initial and final medium are same, i.e., air and the substrate is transparent, the calculations achieve the following simplified relations for reflectance R and transmittance T for the case of an incoherent substrate:

$$\begin{aligned} R = R_{\text{incoherent}} &= |r_1|^2 + \frac{|t_1 t_2 r_2|^2}{1 - |r_2 r_1|^2} \\ T = T_{\text{incoherent}} &= \frac{|t_1 t_2|^2}{1 - |r_2 r_1|^2} . \end{aligned} \tag{5.21}$$

A few relevant examples are as follows:
a) A thick, transparent substrate with a real refractive index s. Using the matrix method explained above, one can calculate the transmission and reflection coefficients, which are:

$$\begin{aligned} t_1 &= \frac{2}{1+s} , \\ t_2 &= \frac{2s}{1+s} , \\ r_1 &= \frac{1-s}{1+s} , \\ r_2 &= \frac{s-1}{1+s} . \end{aligned} \tag{5.22}$$

Using Eq. (5.21), we achieve for this system:

$$T = T_{\text{incoherent}} = \frac{2s}{s^2+1} . \tag{5.23}$$

b) A thin film with complex refractive index, $n + ik$ and thickness d on a thick transparent substrate with real refractive index s as shown in Fig. 5.2.

$$\begin{aligned} T_{\text{meas}}(\lambda) &= \frac{Ax}{B - Cx + Dx^2} \, . \\ A &= 16s(n^2 + k^2), \\ B &= [(n+1)^2 + k^2][(n+1)(n+s^2) + k^2] \, , \\ C &= [(n^2 - 1 + k^2)(n^2 - s^2 + k^2) - 2k^2(s^2 + 1)]2\cos(\phi) \\ &\quad -k[2(n^2 - s^2 + k^2) + (s^2 + 1)(n^2 - 1 + k^2)]2\sin(\phi) \, , \\ D &= [(n-1)^2 + k^2][(n-1)(n-s^2) + k^2] \, , \\ \phi &= 4\pi nd/\lambda, x = \exp(-\alpha d), \alpha = 4\pi k/\lambda \, . \end{aligned} \tag{5.24}$$

This formula takes into account all the multiple reflections at interfaces in the film, when calculating the transmittance. If the thickness of the film is not uniform or is slightly tapered, all interference effects are destroyed and the transmittance is a smooth curve.

5.1.2 Wave propagation in anisotropic layered media

So far, we have treated the propagation of optical waves in layers that are isotropic. As we know from the discussion in the preceding chapters, this is not the case for GaN as it is an anisotropic material where the optical response depends on the polarization of light. It is therefore important to discuss the optical response of anisotropic layered media. More importantly, we must check for similarities and differences between the isotropic and the anisotropic layered media. In this subsection, we will do a similar treatment of reflection and transmission coefficients for an anisotropic medium using matrix method, as was done for the isotropic layered medium in the last subsection.

For the isotropic media, the plane waves were divided into two independent uncoupled modes, i.e., s-polarization or the transverse electric (TE) and the p-polarization or transverse magnetic (TM). Both these polarizations have same phase velocity (c/n) in the medium. Since they are uncoupled, we have to deal with 2×2 matrix system as pointed in Eq. (5.5). However, the plane wave propagation in an anisotropic medium is determined by the dielectric tensor such that the displacement vector **D** and the electric field vector **E** are related by $D_i = \epsilon_{ij} E_j$. It is always possible to find three mutually orthogonal axes in such a way that the off-diagonal elements of the matrix defining the dielectric constant vanish, leaving:

$$\epsilon = \epsilon_0 \begin{pmatrix} n_x^2 & 0 & 0 \\ 0 & n_y^2 & 0 \\ 0 & 0 & n_z^2 \end{pmatrix} = \begin{pmatrix} \epsilon_x & 0 & 0 \\ 0 & \epsilon_y & 0 \\ 0 & 0 & \epsilon_z \end{pmatrix} \, . \tag{5.25}$$

ϵ_x, ϵ_y, and ϵ_z and n_x, n_y and n_z are the dielectric constants and the complex refractive indices along the principal direction and therefore, called the principal dielectric axes of the media. Since GaN is an uniaxial medium, the dielectric constant along the x and

the y axis are equivalent, i.e., $\epsilon_x = \epsilon_y = \epsilon_0 n_o^2$, where n_o is the ordinary refractive index. Similarly $\epsilon_z = \epsilon_0 n_e^2$ where n_e is the extraordinary refractive index. Specifically, for a plane wave propagating along the y-direction, the phase velocity is c/n_x ($n_x = n_o$) for the x-polarized light and c/n_z ($n_z = n_e$), for the z-polarized light. An anisotropic media can be birefringent (dichroic), by which we mean that the real (imaginary) part of the refractive index depends on the in-plane polarization of light. In such media, the electromagnetic radiation consists of four partial waves. Mode coupling takes place at the interface, where an incident plane wave produces waves with different polarization states due to anisotropy of the layers. Therefore, 4×4 matrices are needed in the matrix method.

Consider a general birefringent layered structure, where we assume that the dielectric axis is parallel to the interfaces and the light is incident normal to the layered structure. The propagation direction is along the y axis. Therefore, the light polarization lies in the xz plane. The distribution of the electric field as a function of position is written similar to Eq. (5.6) as:

$$\mathbf{E}(y) = \begin{cases} (A_0^z e^{iK_{0z}y} + B_0^z e^{-iK_{0z}y})\widehat{z} + (A_0^x e^{iK_{0x}y} + B_0^x e^{-iK_{0x}y})\widehat{x} & ; \quad y < y_0 \,, \\ (A_l^z e^{iK_{lz}y} + B_l^z e^{-iK_{lz}y})\widehat{z} + (A_l^x e^{iK_{lx}y} + B_l^x e^{-iK_{lx}y})\widehat{x} & ; \quad y_{l-1} < y < y_l \,, \\ (A_F^z e^{iK_{Fz}y} + B_F^z e^{-iK_{Fz}y})\widehat{z} + (A_F^x e^{iK_{Fx}y} + B_F^x e^{-iK_{Fx}y})\widehat{x} & ; \quad y_N < y \,, \end{cases}$$

where (A_0^z, B_0^z), (A_l^z, B_l^z), and (A_F^z, B_F^z) are the right- and left-travelling wave corresponding to z-polarization, in the 0^{th} (initially), l^{th}, and F^{th} (finally), respectively. Similarly, (A_0^x, B_0^x), (A_l^x, B_l^x), and (A_F^x, B_F^x) are the right- and left-travelling wave corresponding to x-polarization. y_l is the position of the interface between the l^{th} and the $(l+1)^{th}$ layer. Here, K_{lz} and K_{lx} are the y- component of the wavevector corresponding to the z- and the x-polarization in the l^{th} medium. These components are related to the ordinary and the extraordinary refractive indices.

Because of the anisotropy of the medium as well as the mode coupling, there are in general, four coefficients associated with reflection and another four associated with transmission. These are given by:

$$\tilde{r} = \begin{pmatrix} r_{zz} & r_{zx} \\ r_{xz} & r_{xx} \end{pmatrix} , \tag{5.26}$$

$$\tilde{t} = \begin{pmatrix} t_{zz} & t_{zx} \\ t_{xz} & t_{xx} \end{pmatrix} , \tag{5.27}$$

where $\tilde{r}$ and $\tilde{t}$ are the 2×2 matrix for the anisotropic medium.

We can relate the electromagnetic field vector in the $(l-1)^{th}$ layer to the field in l^{th} layer by:

$$\begin{pmatrix} A_{l-1}^z \\ B_{l-1}^z \\ A_{l-1}^x \\ B_{l-1}^x \end{pmatrix} = D_{l-1}^{-1} D_l P l \begin{pmatrix} A_l^z \\ B_l^z \\ A_l^x \\ B_l^x \end{pmatrix} . \tag{5.28}$$

Note that there are four components in the column vector as opposed to 2 in Eq. (5.7).

The matrix D_l is again the dynamical matrix and depends only on the direction of polarization of the four partial waves. These matrices are defined in such a way that they are block diagonalized, when the mode coupling disappears. The matrices P_l depend only on the phase of the four partial waves. If there are N number of layers between the initial medium labelled 0 and the final medium labelled F, the matrix, which relates A_0 and A_F, is given by

$$\begin{pmatrix} A_0^z \\ B_0^z \\ A_0^x \\ B_0^x \end{pmatrix} = T_{0,1}T_{1,2}T_{2,3}.....T_{N-1,N}T_{N,F} \begin{pmatrix} A_F^z \\ B_F^z \\ A_F^x \\ B_F^x \end{pmatrix} , \tag{5.29}$$

where $F = N + 1$ and d_{N+1}=0 and $T_{l-1,l}$= $D_{l-1}^{-1} D_l P_l$

For the simplistic case of normal incidence and when the dielectric axis of the medium is the same as the axis along which one measure the angle of the polarizer (lab axis), the dynamical matrix D_l and the propagation matrix P_l reduce to:

$$D_l = \begin{pmatrix} 1 & 1 & 0 & 0 \\ n_l^z & -n_l^z & 0 & 0 \\ 0 & 0 & 1 & 1 \\ 0 & 0 & n_l^x & -n_l^x \end{pmatrix} \tag{5.30}$$

$$P_l = \begin{pmatrix} e^{i2\pi n_l^z d_l/\lambda} & 0 & 0 & 0 \\ 0 & e^{-i2\pi n_l^z d_l/\lambda} & 0 & 0 \\ 0 & 0 & e^{i2\pi n_l^x d_l/\lambda} & 0 \\ 0 & 0 & 0 & e^{-i2\pi n_l^z d_l/\lambda} \end{pmatrix} , \tag{5.31}$$

where n_l^z and n_l^x are the refractive indices for the z-polarization and x-polarization in the l^{th} layer, respectively. d_l is the thickness of the l^{th} layer.

Matrix Method for Transmittance: In our case the system is as follows: We have a thin film of M-plane GaN, which is both birefringent and dichroic, on a thick substrate γ-$LiAlO_2$, which is also birefringent. Hence, both the layer and the substrate are anisotropic media with different dielectric constants for two orthogonal directions. Due to this anisotropy, the electromagnetic wave is expressed by four modes, of which two are for $\boldsymbol{E} \parallel \boldsymbol{c}$ and the other two are for $\boldsymbol{E} \perp \boldsymbol{c}$.

Assume that the light is incident from the left side of the structure and A_0^z and A_0^x (A_F^z and A_F^x) denote the amplitudes of the waves travelling in front of the system (after the system) to the right with a polarization parallel to the z and x axis, respectively, while B_0^z and B_0^x (B_F^z and B_F^x) denote the corresponding amplitudes for waves travelling in front of the system (behind the system) to the left. Using the matrix method one can relate the electric field amplitude before and after system by:

$$\begin{pmatrix} A_0^z \\ B_0^z \\ A_0^x \\ B_0^x \end{pmatrix} = \begin{pmatrix} M_{11}M_{12}M_{13}M_{14} \\ M_{21}M_{22}M_{23}M_{24} \\ M_{31}M_{32}M_{33}M_{34} \\ M_{41}M_{42}M_{43}M_{44} \end{pmatrix} \begin{pmatrix} A_F^z \\ B_F^z \\ A_F^x \\ B_F^x \end{pmatrix} . \tag{5.32}$$

Since the final medium is considered to be semi-infinite, there are no traveling waves to the left so that B_F^z and B_F^x are equal to zero. The reflection and transmission coefficients can be expressed in terms of individual matrix elements as follows:

$$\begin{aligned}
r_{zz} &= \left(\frac{B_0^z}{A_0^z}\right)_{A_0^x=0} = \frac{M_{21}M_{33} - M_{23}M_{31}}{M_{11}M_{33} - M_{13}M_{31}}\,, \\
r_{zx} &= \left(\frac{B_0^x}{A_0^z}\right)_{A_0^x=0} = \frac{M_{41}M_{33} - M_{43}M_{31}}{M_{11}M_{33} - M_{13}M_{31}}\,, \\
r_{xx} &= \left(\frac{B_0^x}{A_0^x}\right)_{A_0^z=0} = \frac{M_{11}M_{43} - M_{41}M_{13}}{M_{11}M_{33} - M_{13}M_{31}}\,, \\
t_{zz} &= \left(\frac{A_F^z}{A_0^z}\right)_{A_0^x=0} = \frac{M_{33}}{M_{11}M_{33} - M_{13}M_{31}}\,, \\
t_{zx} &= \left(\frac{A_F^x}{A_0^z}\right)_{A_0^x=0} = \frac{-M_{13}}{M_{11}M_{33} - M_{13}M_{31}}\,, \\
t_{xx} &= \left(\frac{A_F^x}{A_0^x}\right)_{A_0^z=0} = \frac{M_{11}}{M_{11}M_{33} - M_{13}M_{31}}\,.
\end{aligned} \tag{5.33}$$

Since we consider the transmission under normal incidence, the axes in the laboratory frame overlap with the optical axes of the uniaxial medium. Furthermore, the optical axes of the substrate overlap with the optical axes of the layer because of the epitaxial relation followed (cf. Chapter 3). Therefore, the matrix elements M_{13}, M_{14}, M_{23}, and M_{24} as well as M_{31}, M_{32}, M_{41}, and M_{42} are all equal to zero so that the 4×4 matrix is reduced to a block diagonal form with two 2×2 matrices, corresponding to the two primary directions, i.e., z and x. The individual components of the reflection and transmission coefficient in Eq. (5.33) now reduce to the following values:

$$r_{zz} = \frac{M_{21}}{M_{11}}; r_{zx} = 0; r_{xx} = \frac{M_{43}}{M_{33}}\,, \tag{5.34}$$

$$t_{zz} = \frac{1}{M_{11}}; t_{zx} = 0; t_{xx} = \frac{1}{M_{33}}\,. \tag{5.35}$$

$r_{zx} = t_{zx} = 0$ signify that there is no mode coupling between the two modes corresponding to the z- and the x-polarization. For an isotropic medium, there is no distinction between the s and p polarized wave at normal incidence. However, for an anisotropic medium, the distinction exist even for the case of normal incidence as the refractive indices are different for the two polarizations. However, we cannot distinguish the s and p wave at normal incidence so we describe such a case with z- and x-polarization. The problem is reduced to the following matrix:

$$\begin{pmatrix} A_0^i \\ B_0^i \end{pmatrix} = \begin{pmatrix} M_{11}^i A_F^i \\ M_{21}^i A_F^i \end{pmatrix}\,, \tag{5.36}$$

where i refers to the z- ($\boldsymbol{E} \parallel \boldsymbol{c}$) or x-direction ($\boldsymbol{E} \perp \boldsymbol{c}$) and M_{jk}^i ($j,k = 1$ or 2) denotes the transfer matrix components for the respective polarization direction. For polarization parallel to the c axis, the transmission coefficient is given by $A_F^z/A_0^z = t_{\parallel} = 1/M_{11}^z$ resulting in a transmittance $T_{\parallel} = 1/|M_{11}^z|^2$. For polarization perpendicular to the c axis,

$A_F^x/A_0^x = t_\perp = 1/M_{11}^x$ and the transmittance is $T_\perp = 1/|M_{11}^x|^2$. For an incoming light beam, which is linearly polarized with an arbitrary initial polarization angle ϕ_i, which is the angle the electric field vector makes with the unique c axis, the components of the electric field can be written as $A_0^z = A\cos(\phi_i)$ and $A_0^x = A\sin(\phi_i)$. We obtain for the transmittance

$$\frac{|A_F^z|^2 + |A_F^x|^2}{|A_0^z|^2 + |A_0^x|^2} = T(E,\phi_i) = T_\parallel(E)\cos^2(\phi_i) + T_\perp(E)\sin^2(\phi_i)\ . \tag{5.37}$$

Therefore, for an arbitrary angle ϕ_i, the transmittance is determined only by three independent quantities $T_\parallel$, $T_\perp$, and ϕ_i. The ratio of the amplitudes of the two orthogonal electric-field components of the outgoing light beam also depends only on these three quantities, i.e.,

$$\left|\frac{A_F^x}{A_F^z}\right| = \tan(\phi_i)\sqrt{\frac{T_\perp}{T_\parallel}}\ . \tag{5.38}$$

Note that in order to derive Eqs. (5.37) and [5.38], we did not have to make any assumptions about the polarization properties of the outgoing beam. It can either be linearly polarized or more generally elliptically polarized.

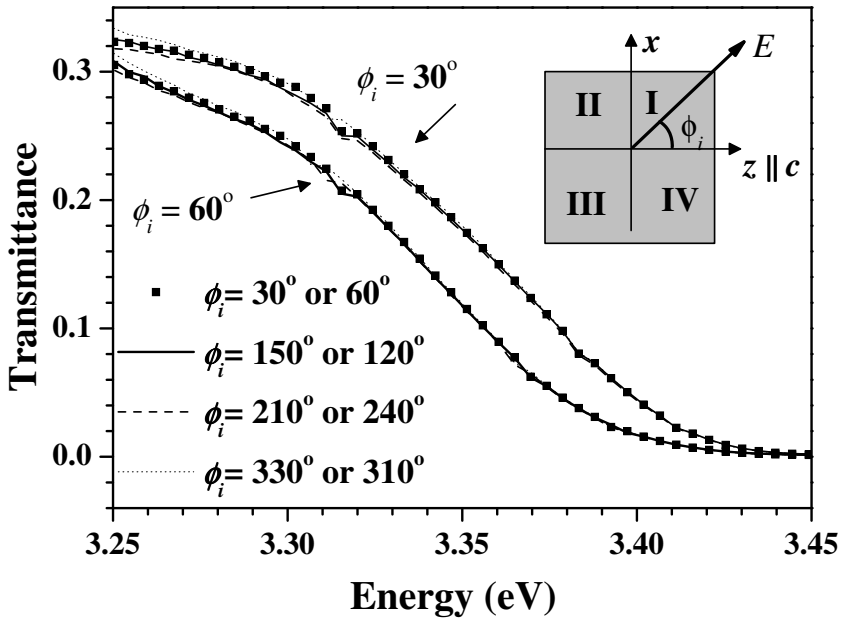

Figure 5.3: The symmetry in transmittance of the 1.22 μm-thick M-plane GaN film is verified by measurement of T(ϕ_i) at 295 K, for the measurement angle varying between $0^\circ < \phi_i < 360^\circ$. We find that T($\phi_i$)=T($180^\circ - \phi_i$) for ϕ_i in the I and II quadrant. Similar results hold for ϕ_i in the III and IV quadrant.

5.1.3 Experimental evidence of polarization anisotropy

We will now focus on the experimental characterization of in-plane polarization anisotropy in M-plane GaN grown on γ-$LiAlO_2$. Eq. (5.37) suggests that there is a symmetry in the transmittance (T) as a function of polarization angle ϕ_i. The transmittance satisfies the following relationship:

$$T(\phi_i) = T(180 - \phi_i);\quad 0^\circ < \phi_i < 180^\circ\ . \tag{5.39}$$

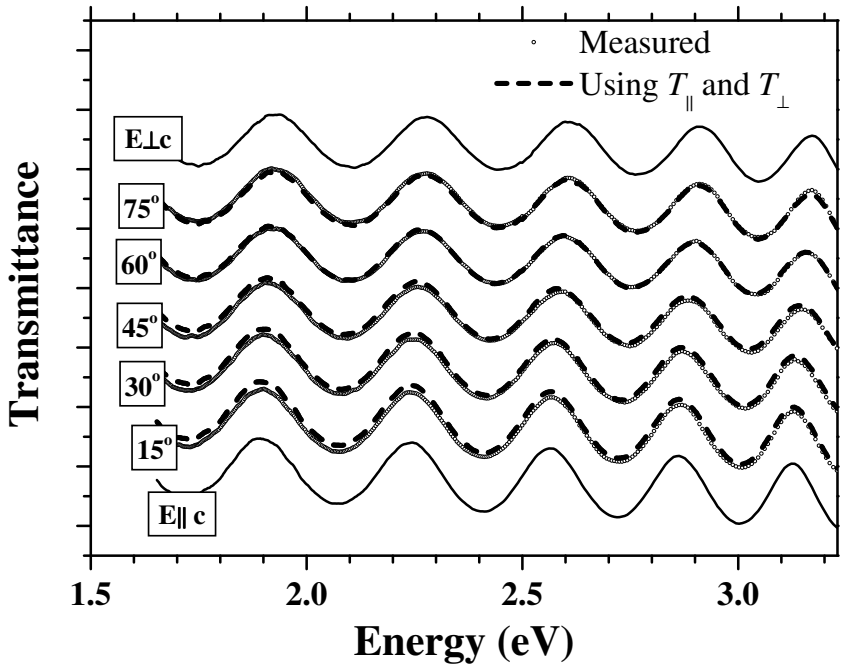

Figure 5.4: Measured transmission spectra (symbols) in the wavelength range 350 - 750 nm for several polarization angles ϕ_i between 0° and 90° in steps of 15° at 295 K for the 0.7 μm-thick *M*-plane GaN film in the transparent regime. The dashed lines for $\phi_i = 15°$ to 75° indicate the result of the calculation according to Eq. (5.37).

We have checked this symmetry relationship for $0° < \phi_i < 360°$ for the 1.22 μm-thick *M*-plane GaN film. Fig. 5.3 shows the measurement result for ϕ_i=30° and 60°. It is found that, when $\phi_i = 30°$ the transmittance T is exactly equal to that measured for $\phi_i = 180° - 30° = 150°$. Similarly, for ϕ_i= 60° and $\phi_i = 180° - 60° = 120°$, the transmittances are the same. Similarly, for ϕ_i lying in the IIIrd and the IVth quadrant, the relation is satisfied , proving symmetry relationship in Eq. (5.39).

Let us now focus on the relation in Eq. (5.37), where the transmittance for an arbitrary angle ϕ_i depends on the transmittance for $\phi_i = 0°$ and $\phi_i = 90°$. We divide the transmittance into the transparent and the absorbing regions. and will independently prove the validity of this equation in both the regimes.

Firstly, let us deal with the region where GaN is transparent. For this purpose, we measure the transmittance $T(\phi_i)$ for the 0.7 μm-thick *M*-plane GaN film at 295 K. The measurement is done for polarization angle ϕ_i between 0° and 90° in steps of 15° for wavelength from 380 nm to 750 nm. The experimental results are shown in Fig. 5.4. The individual transmittance curve for each polarization angle is shifted vertically for clarity. The interference fringes in the transparent region, show a constant energy shift, when the incoming polarization angle is rotated from ϕ_i= 0° ($\boldsymbol{E} \parallel \boldsymbol{c}$) to ϕ_i= 90° ($\boldsymbol{E} \perp \boldsymbol{c}$). The different position of the interference fringes indicates different refractive indices (linear birefringence) for different incoming polarizations. A detailed experimental characterization of linear birefringence is done in later sections. Using Eq. (5.37), we calculated the transmittance for different values of ϕ_i from the measured transmittances $T_{\parallel}$ ($\phi_i = 0°$) and $T_{\perp}$ ($\phi_i = 90°$). The dashed lines in Fig. 5.4 show the cal-

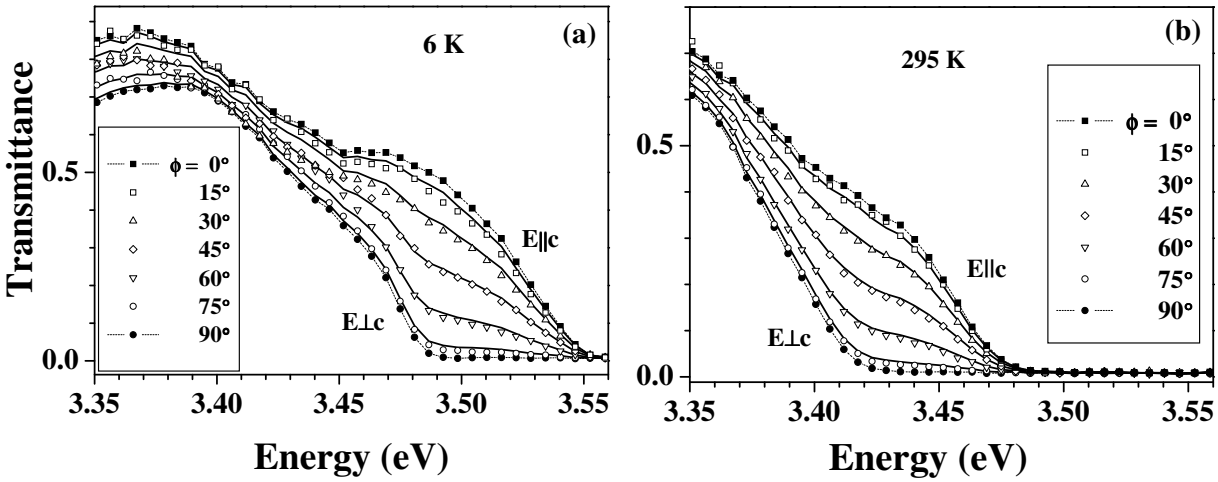

Figure 5.5: Measured transmission spectra (symbols) near the bandgap for several polarization angles ϕ_i between 0° and 90° in steps of 15° at (a) 6 K and (b) 295 K for the 0.7 μm-thick M-plane GaN film. The solid lines for $\phi_i = 15°$ to 75° indicate the result of the calculation according to Eq. (5.37).

culated transmittances. The excellent agreement of the measured transmittances with the calculated ones using Eq. (5.37) proves the validity of the equation in the transparent region.

Now we will focus on the transmittance near the band-gap of M-plane GaN. The measured transmittance under normal incidence of the M-plane GaN film is shown in Figs. 5.5(a) and 5.5(b) by the full symbols for $T_{\parallel}$ ($\phi_i = 0°$) and $T_{\perp}$ ($\phi_i = 90°$), for 6 and 295 K, respectively. At both the temperatures, we observe a significant shift of the effective energy gap towards higher energies for $\phi_i = 0°$, i.e., $\boldsymbol{E} \parallel \boldsymbol{c}$, in comparison to $\phi_i = 90°$, i.e., $\boldsymbol{E} \perp \boldsymbol{c}$. The band gap increases by 49 meV (60 meV) at 295 K (6 K). The larger separation at low temperatures may be due to a higher in-plane strain because of the larger thermal expansion coefficient mismatch compared to room temperature. A different inhomogeneous broadening of the two transitions at the two temperatures could also contribute to the difference in the separation. Note that the energy scales in Figs. 5.5(a) and 5.5(b) are identical in order to clearly demonstrate the red-shift of the energy gap from low to room temperature. The results of polarization dependent transmittance near the bandgap are shown by the open symbols in Fig. 5.5 for $0° < \phi_i < 90°$ in steps of 15°. The gradual shift in the energy of the absorption edge indicates that the film has different absorption coefficients (linear dichroism) depending on the incoming polarization angle. Using Eq. (5.37) again, we calculated the transmittance for different values of ϕ_i from the measured transmittances $T_{\parallel}$ ($\phi_i = 0°$), $T_{\perp}$ (90°) and ϕ_i. The solid lines in Fig. 5.5 show the calculated transmittances, which agree very well with the measured data.

The band-structure calculations done in Chapter 2 suggests that the T_1 transition from the top most valence band has predominantly X-like valence band states, the T_2 transition from the second-highest valence band states has Z-like wave characteristics, and the T_3 transition from the third-highest valence band states has Y-like wave characteristics (cf. Fig. 4.6). These three primary transitions gives rise to transmittance for light polarized along the fundamental directions. One of these fundamental directions

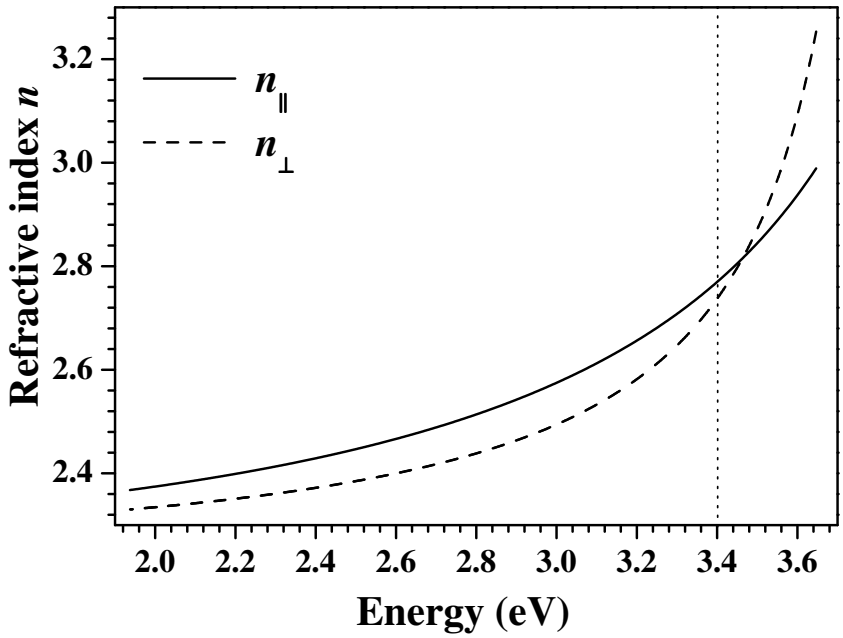

Figure 5.6: Using the method as discussed by Swanepoel [128], which uses only the transmittance data to estimate the refractive index, we have determined both the ordinary and the extraordinary refractive indices for the 0.7 μm-thick M-plane GaN film at 295 K. The film clearly shows birefringence but the difference $\Delta n = n_e - n_o$ becomes zero at about 3.44 eV (360 nm).

is along the c axis, while the other is normal to it, along the x axis. The optical properties for polarization in between these two directions, can be described in terms of the optical response of the system along the fundamental directions which are parallel and perpendicular to $\boldsymbol{c}$. The third transition, along the y axis is not accessible at normal incidence and, therefore, does not contribute to the transmittance spectra.

5.1.4 Calculation of the refractive index and absorption coefficient for *M*-plane GaN thin films

The optical transmittance of a thin absorbing film on a thick transparent substrate is given by Eq. (5.24), which depends on the dielectric constants of the film and the substrate, the thickness of the film and the wavelength. From a set of experimental data points (λ_i,$T_{\mathrm{meas},i}$), one needs to determine d, $n(\lambda)$ and $k(\lambda)$. The problem of retrieving these constants for the film from the transmittance data is highly undetermined. For example, even if the thickness d is known, the following relation must hold:

$$T_{\mathrm{theory}}[\lambda_i, s(\lambda_i), d, n(\lambda_i), k(\lambda_i)] = T_{\mathrm{meas}} \; . \tag{5.40}$$

Eq. (5.40) has two unknowns, $n(\lambda_i)$ and $k(\lambda_i)$ for each wavelength. The solutions are in general a curve in the $[n(\lambda_i), k(\lambda_i)]$ space. Since the number of equations exceeds the number of unknowns, there is no unique solution. Therefore, the sets of dielectric functions (n, k) that satisfy the above equation are infinite and are represented by a non-linear manifold of dimension $\mathbb{R}^{2N}$. Swanepoel [128] has manipulated Eq. (5.24) to yield relations in closed form to calculate the refractive index and the extinction coefficient. We will follow this technique to calculate the refractive index for the M-plane GaN thin film on γ-$LiAlO_2$. The transmittance for such a system as a thin absorbing film on a

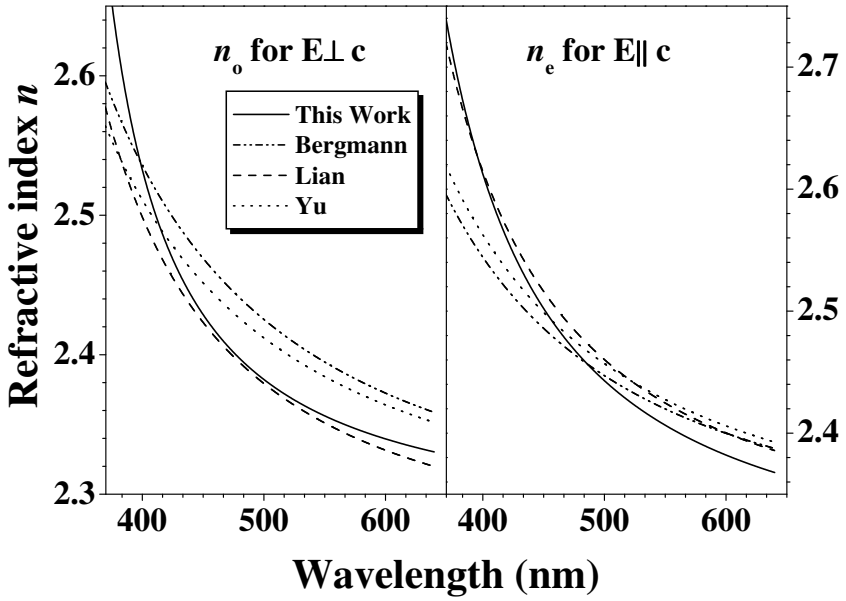

Figure 5.7: Comparison of the ordinary and the extraordinary refractive indices from our calculations with results from other groups. Various groups have used different functions to fit the refractive index dispersion. The following references are used: Bergmann [129], Lian [130], Yu [131].

thick transparent substrate can be roughly divided into 4 regions. In the transparent region, the absorption coefficient $\alpha = 0$, and the transmittance is determined by n and s through multiple reflections, which give rise to interference fringes. In the region of weak absorption, α is small, but starts to reduce the transmission. In the region of medium absorption, α is large, and the transmission decreases mainly because of increasing α. In the region of high absorption, the transmittance shows a sharp decrease and tends to zero. If the film is non-uniform and tapered, the transmission curve is smooth and can be used to calculate the dielectric constants. [132] However, when the thickness is uniform, interference effects due to the difference in the refractive indices between the GaN thin film and the substrate give rise to interference fringes. These fringes have been used to calculate the optical constants of the film as discussed in detail by Swanepoel. [128] The expression for T is much simpler in the regime, where the absorption coefficient is zero. One can achieve a closed form for the maximum T_M and the minimum T_m transmittance for this regime. T_M and T_m are considered as continuous functions of λ and also of $n(\lambda)$ and $k(\lambda)$ as was done by Manifacier *et al.* [133] So for any λ, T_M has a corresponding value T_m and vice versa. For all the calculations, the refractive index of the γ-$LiAlO_2$ substrate is taken to be 1.614 along for $\boldsymbol{E}\perp\boldsymbol{c}$ and 1.604 for $\boldsymbol{E}\|\boldsymbol{c}$ as suggested in Ref. [134]. We use the transmittance as shown in Fig. 4.11 to calculate the refractive index. Figure 5.6 shows the determined refractive indices for the two polarization directions in the energy range between 1.94 and 3.65 eV (340–640 nm). Since it is difficult to accurately determine the refractive index from the transmittance spectra alone in the strongly absorbing regime (above 3.4 eV), we have extrapolated the refractive indices calculated in the region of medium and low absorption (transparent regime) to the strongly absorbing energy range (energies larger than indicated by the vertical dotted line in Fig. 5.6). A similar extrapolation was done by Swanepoel. [128] Various functional forms of the Sellmeier dispersion formulation relating the refractive index and the wavelength are used to fit the dependence, i.e., n versus λ. We analyze

the experimental data using a Sellmeier-type dispersion relationship given as: [130]

$$n^2(\lambda) = \epsilon_\infty + \frac{A_1^2}{\lambda^2 - A_2^2} \,. \tag{5.41}$$

ϵ_∞, A_1 and A_2 are the fitting parameters, while λ is the wavelength in nm. As $\lambda \to \infty$, the electronic contribution to the dielectric function approaches a limiting value ϵ_∞. Another variation of the same relation is also used in literature [123, 131]:

$$n^2(\lambda) = 1 + \frac{B_1\lambda^2}{\lambda^2 - B_2^2} \,, \tag{5.42}$$

where $\epsilon_\infty = 1 + B_1$. The parameters that were achieved by fitting the experimental data with the Sellmeier relation are shown in Table. 5.1.

A comparison of the ordinary n_o and the extraordinary n_e refractive indices for GaN from our calculations with the results from other groups is shown in Fig. 5.7. There is a systematic error of 2% in the n_o and n_e values due to uncertainty in the film thickness. The average difference $n_e - n_o$ at long wavelengths is 0.03. Our n_o values agree well with those in Refs. [123] and [135].

Once $n(\lambda)$ is known, the extinction coefficient $k(\lambda)$ or absorption coefficient $\alpha(\lambda)$ can be determined using the envelope T_M or T_m. A formulation to obtain $\alpha(\lambda)$ from the transmittance alone has been suggested by Swanepoel. [128] Another method is to use an average of the interference fringes in absorption or transmittance spectrum. Ritter and Weiser [136] show that normalizing the absorbance by the transmittance practically eliminates interference fringes, and the absorption coefficient can be calculated from this ratio. This procedure is more accurate than averaging, particularly at higher absorption values, and has the advantage of combining transmission and reflection into one set of measurements. For a film with an absorption coefficient α and refractive index n on a non-absorbing substrate with refractive index s, the transmittance T reflectance R and absorbance $A = 1 - R - T$ results in the following relation

Table 5.1: Fit to the experimental data for refractive index measured for *M*-plane GaN film at 295 K. The fit is done for both $\boldsymbol{E}\|\boldsymbol{c}$ and $\boldsymbol{E}\perp\boldsymbol{c}$. Sellmeier's relation given in Eq. (5.41) is used for fitting and yields the following parameters.

Reference	Polarization	Formula used	ϵ_∞	A_1 or B_1 nm	A_2 or B_2 nm	Comments
This work	$\boldsymbol{E}\|\boldsymbol{c}$ (n_e)	Eq. (5.41)	5.23	353	286	Single Oscillator
	$\boldsymbol{E}\perp\boldsymbol{c}$ (n_o)		5.20	263	320	*M*-plane GaN film
Lian	$\boldsymbol{E}\|\boldsymbol{c}$ (n_e)	Eq. (5.41)	5.29	368	269	Single Oscillator
(Ref. [130])	$\boldsymbol{E}\perp\boldsymbol{c}$ (n_o)		5.06	331	260	
Bergmann	$\boldsymbol{E}\|\boldsymbol{c}$ (n_e)	Eq. (5.42)	5.307	4.307	190.3	Single Oscillator
(Ref. [129])	$\boldsymbol{E}\perp\boldsymbol{c}$ (n_o)		5.141	4.141	187.4	
Yu	$\boldsymbol{E}\|\boldsymbol{c}$ (n_e)	Eq. (5.42)	5.31	4.31	184.4	Single Oscillator
(Refs. [123, 131])	$\boldsymbol{E}\perp\boldsymbol{c}$ (n_o)		5.14	4.14	194.9	$\epsilon_\infty = 1 + B_1$
Ghosh	$\boldsymbol{E}\|\boldsymbol{c}$ (n_e)	—	5.514	—	—	Double Oscillator
(Ref. [22])	$\boldsymbol{E}\perp\boldsymbol{c}$ (n_o)		5.346	—	—	*M*-plane GaN film
Sobotta	$\boldsymbol{E}\|\boldsymbol{c}$ (n_e)	—	5.2	—	—	Infrared
(Ref. [135])	$\boldsymbol{E}\perp\boldsymbol{c}$ (n_o)	—	5.2	—	—	Reflectivity

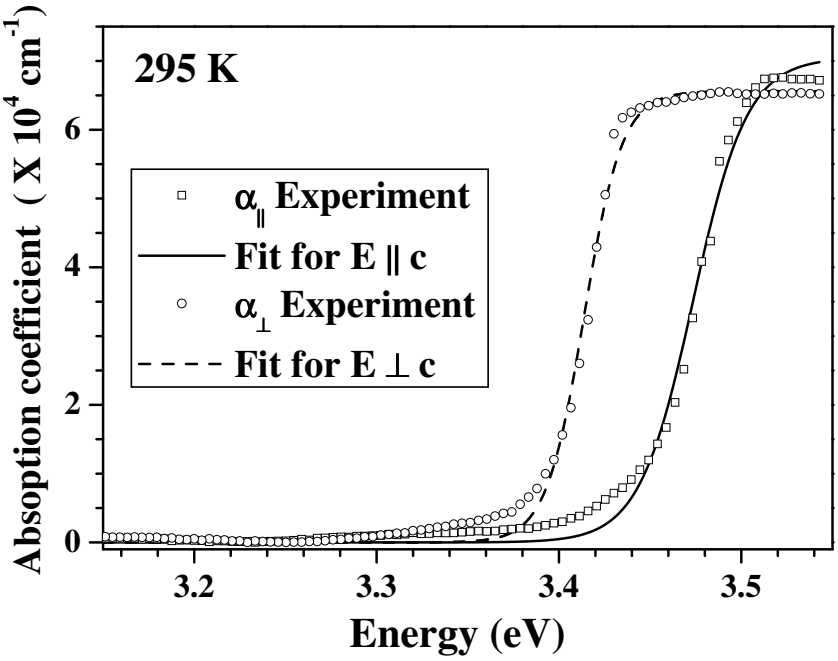

Figure 5.8: Comparison of the absorption coefficient for polarization $\boldsymbol{E}\|\boldsymbol{c}$ ($\alpha_{\|}$) and $\boldsymbol{E}\perp\boldsymbol{c}$ ($\alpha_{\perp}$) for the 0.7 μm-thick *M*-plane GaN film. A clear shift in the band gap of *M*-plane GaN can be seen when the polarization of the light is rotated by 90°. This shift signifies that *M*-plane GaN shows linear dichroism. The solid lines denote the fit using the sigmoidal function described in Eq. (5.45).

for the absorption coefficient α [136]:

$$\alpha = \frac{1}{d} \ln \left[\frac{(1-R_{fs})(1+A/T) + \sqrt{(1-R_{fs})^2(1+A/T)^2 + 4R_{fs}}}{2} \right] , \tag{5.43}$$

where

$$R_{fs} = \frac{(n-s)^2}{(n+s)^2} , \tag{5.44}$$

denotes the reflectivity from the film-substrate interface, when light is incident from the film side. The influence of the substrate-air interface on the absorbance as well as on the reflectance has been neglected, as was done by Driss-Khodja *et al.* [137] The absorption coefficients derived from Eqs. (5.43) and (5.44) are shown for polarization directions $\boldsymbol{E} \parallel \boldsymbol{c}$ and $\boldsymbol{E} \perp \boldsymbol{c}$ in Fig. 5.8. In the energy range from 3.35 to 3.5 eV, the absorption coefficients of the two polarization directions are different, clearly showing linear dichroism. Using the relation $(\alpha E)^2 = C(E - E_g)$, we can estimate the bandgap energy from the absorption coefficient. Figure 5.9 displays the energy gaps estimated from the absorption coefficient α by fitting a straight line to the quantity $(\alpha E)^2$ as shown by the solid lines in order to determine the energy separation of the two transitions. We obtain $E_{g\|} = 3.457$ eV and $E_{g\perp} = 3.402$ eV at room temperature, resulting in a separation of the top two valence bands of around 55 meV. The direct comparison of the measured absorption coefficients with values in the literature is rather difficult, because the VB structure and consequently the resulting absorption coefficients for the two polarization directions depend critically on the strain state of the investigated film. Note that the calculation of the refractive index is done using transmittance at normal

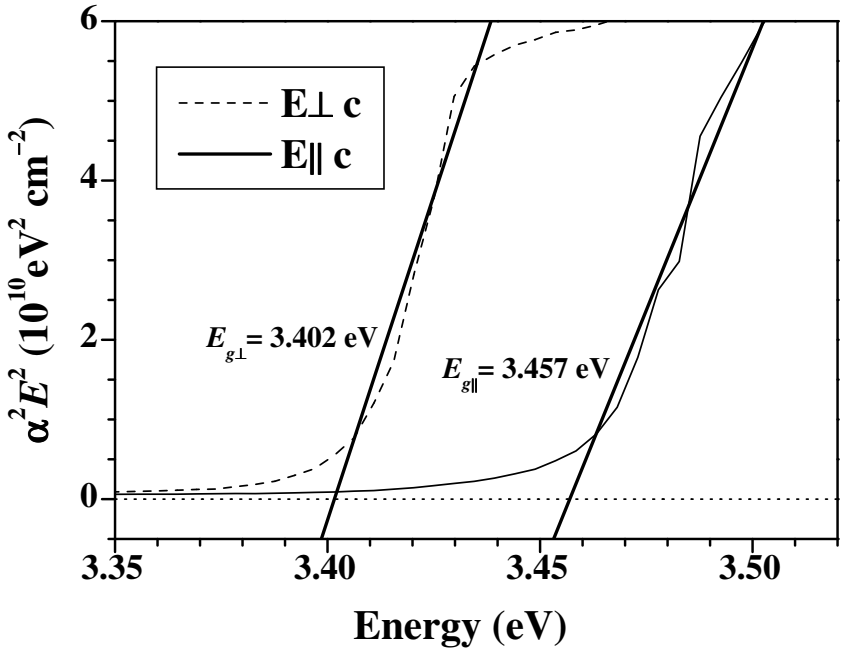

Figure 5.9: The band-gap energy is estimated by plotting $(\alpha E)^2$ versus the photon energy for the 0.7 μm-thick M-plane GaN film. The slope of the linear fit gives the band-gap energy.

Table 5.2: Fit to the calculated values of absorption coefficient α for M-plane GaN film at 295 K. The fit is done for both $\boldsymbol{E}\|\boldsymbol{c}$ and $\boldsymbol{E}\perp\boldsymbol{c}$. Eq. (5.45) is used for fitting and yields the following fit parameters in Fig. 5.9. E_g denotes the transition energy as achieved by using absorption coefficient.

Polarization	α_0 (10^4 cm^{-1})	E_B (eV)	ΔE (meV)	E_B - E_G meV
$\boldsymbol{E}\|\boldsymbol{c}$	7.05	3.473	14.8	16
$\boldsymbol{E}\perp\boldsymbol{c}$	6.56	3.414	10.4	12

incidence only, while the calculation of the absorption coefficients involve, in addition to the transmittance, the reflectance at near normal incidence.

It is known that the presence of band tail states influence the onset of absorption and therefore the absorption coefficient. Band tails are formed due to disorder and carrier interactions, and the band tail parameters depends on the carrier concentration, impurities and the structural disorder. The degree of structural disorder for crystalline semiconductors is associated with lattice imperfections, defects, dislocations and strain. It is essential to have an accurate description of the absorption edge that includes the effect of broadening due to band-tailing. This is provided by fitting the rising edge and plateau of the absorption coefficient α to the sigmoidal (S-shaped) function: [138]

$$\alpha = \frac{\alpha_0}{1 + \exp(\frac{E_B - E}{\Delta E})}\,, \tag{5.45}$$

where E_B is identified as the effective band gap energy of the semiconductor and a broadening parameter ΔE, which is equivalent to the Urbach energy. The fit using Eq. (5.45) is shown by solid line for both $\boldsymbol{E}\parallel$ and $\perp\boldsymbol{c}$ in Fig. 5.8. The fit parameters achieved are shown in Table 5.2. The effective band gap energy E_B is different than the ones calculated using absorption coefficient α in Fig. 5.9 by roughly 14 meV.

The values of the bandgap calculated using absorption coefficients are very different than the ones achieved from PR measurements in Chapter 4, where the values were $E_\perp$ = 3.437 + 0.026 = 3.463 eV and $E_\perp$ = 3.491 + 0.026 = 3.517 eV. 26 meV is added for the excitonic binding energy. This energy is roughly 60 meV higher than the values achieved by using the absorption coefficient. This may be due to tail states which affect the absorption more adversely than the PR spectra. The absolute transition energies achieved by PR measurement are more accurate than the ones calculated using the absorption coefficients. However, the separation between the top two valence bands measured by absorption coefficient (55 meV) is same as the one measured by PR, where it is 54 meV.

5.1.5 Polarization filtering and rotation

As stated before, we did not make any assumption regarding the polarization state of the outgoing beam to derive Eqs. (5.37) and (5.38). As a first approximation, let us now assume that the outgoing light is also linearly polarized. In this case, the polarization angle of the outgoing light beam with the c axis is denoted by ϕ_f so that $A_F^z = C\cos(\phi_f)$ and $A_F^x = C\sin(\phi_f)$ are the amplitudes of the plane wave after the system along the z- and x-direction, respectively. The transmittance for an arbitrary angle ϕ_f depends only on three quantities ($T_\parallel$, $T_\perp$, and ϕ_f) according to

$$\frac{1}{T(E,\phi_f)} = \frac{1}{T_\parallel(E)}\cos^2(\phi_f) + \frac{1}{T_\perp(E)}\sin^2(\phi_f)\ . \tag{5.46}$$

This relation is similar to Eq. (5.37) and has the same symmetry relations for ϕ_f as Eq. (5.37) satisfies for ϕ_i. We can also relate the outgoing angle ϕ_f to the incoming angle ϕ_i using the relation in Eq. (5.38):

$$\tan(\phi_f) = \tan(\phi_i)\,\sqrt{T_\perp/T_\parallel}\ . \tag{5.47}$$

The polarization angle of the outgoing light beam depends only on $T_\parallel$, $T_\perp$, and ϕ_i. A consequence of the large in-plane polarization anisotropy is the rotation of the polarization vector in the energy range, where the transmittances (absorption coefficients) for the two orthogonal polarizations are very different. The rotation is a result of an anisotropic polarization filtering, when the absorption of light is different for two orthogonal polarizations. The polarization of light for $\boldsymbol{E} \perp \boldsymbol{c}$ is more strongly absorbed than for $\boldsymbol{E} \parallel \boldsymbol{c}$. As a consequence, an incoming linearly polarized light beam, at an angle ϕ_i with respect to the c axis will be rotated to ϕ_f as shown in Fig. 5.10. According to Eq. (5.38), this rotation will be given by

$$\Phi = \phi_i - \phi_f = \phi_i - \arctan\left(\tan(\phi_i)\,\sqrt{\frac{T_\perp}{T_\parallel}}\right)\ . \tag{5.48}$$

The above formula is valid with the initial assumption that the film does not show any linear birefringence. A more general analysis, taking into account both the linear dichroism and linear birefringence, will be discussed below. Φ is a measure of the rotation of the in-plane polarization vector. However, this apparent rotation actually corresponds to a polarization filtering. If we consider a spectral region, where $T_\perp \ll T_\parallel$,

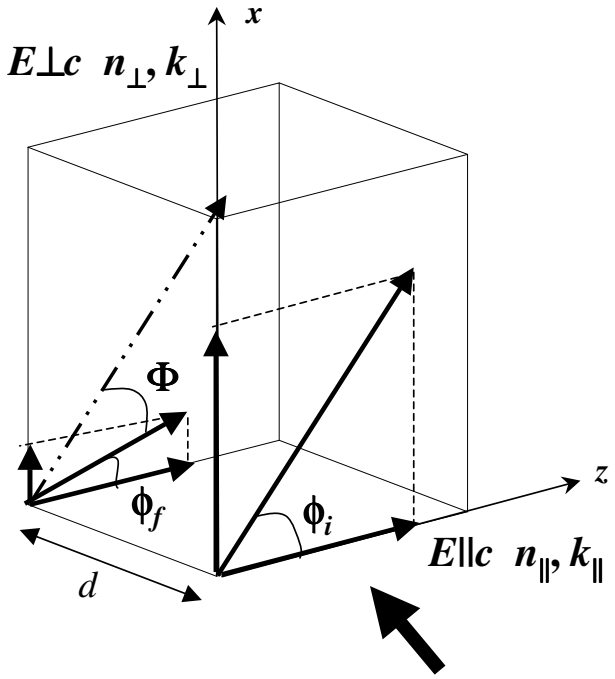

Figure 5.10: The propagation of light with initial polarization at ϕ_i. The polarization changes to ϕ_f after propagation, and the amplitude (intensity) of light decreases due to absorption. Effectively, the polarization vector is rotated by $\Phi = \phi_i - \phi_f$.

the polarization angle ϕ_f of the outgoing light beam will become almost zero. In this spectral region, only the parallel component of the polarization vector is transmitted, while the perpendicular component is almost completely absorbed. Note that in reality the polarization filtering or rotation will never be complete due to the finiteness of $T_\perp$, and consequently ϕ_f will never be exactly zero. For an infinitely thick film, no polarization filtering or rotation will occur, because all light is absorbed for both polarization directions. This type of polarization rotation is very different from the one seen in active devices such as waveplates. In such devices, the outgoing light has the same intensity as the incoming light before transmission, and only the polarization direction is changed due to an anisotropic phase delay introduced by linear birefringence. In our case, the intensity of the outgoing light after transmission is considerably reduced due to anisotropic absorption. The degree of rotation can be used to quantify the amount of anisotropic absorption.

Since in the energy range of interest $T_\perp \ll T_\parallel$ (cf. Fig. 5.5), the polarization rotation angle Φ will be positive so that the rotation will occur toward the c axis as shown in Fig. 5.10. In the ideal case, when $T_\perp$ becomes orders of magnitude smaller than $T_\parallel$, the rotation angle Φ will become almost equal to ϕ_i. Experimentally, however, the ratio $T_\perp / T_\parallel$ is considerably larger than in the ideal case due to a finite signal-to-noise ratio. We now, compare the measured rotation angle Φ to the one calculated using Eq. (5.48).

5.1.6 Polarization rotation for linearly polarized light at ϕ_i=45°

First let us take the case when the polarization vector of incoming linearly polarized light is making an angle of 45° with the c axis. The measurement is done at 6 and 295 K

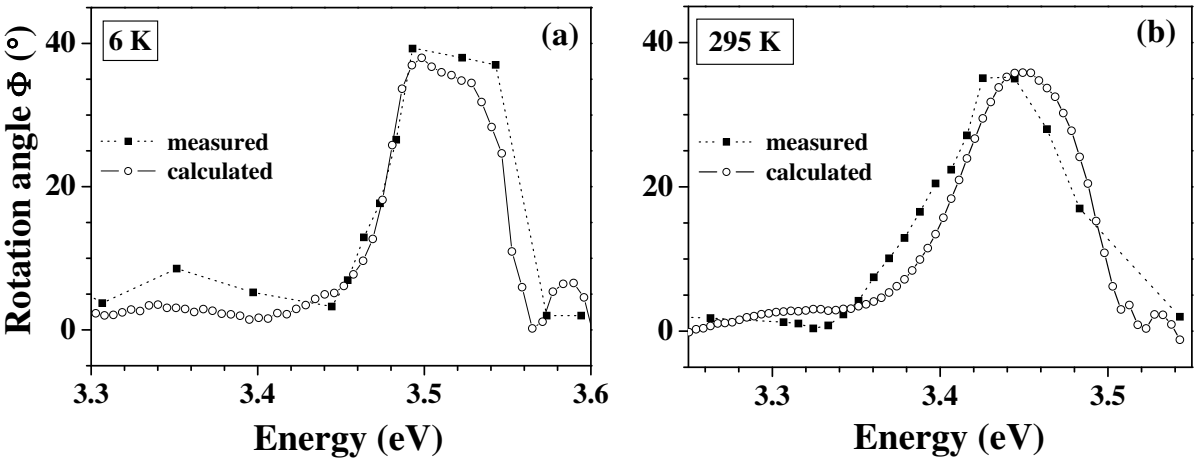

Figure 5.11: Measured (full squares) and calculated (open circles) rotation angle Φ of the polarization versus energy for $\phi_i = 45^\circ$ at (a) 6 K and (b) 295 K for the 0.7 μm-thick M-plane GaN film.

as a function of energy near the band gap region. Eq. (5.48) reduces to

$$\Phi = 45^\circ - \phi_f = 45^\circ - \arctan\left(\sqrt{\frac{T_\perp}{T_\parallel}}\right) . \tag{5.49}$$

The energy range near the band gap is of interest because the transmittances for both polarizations are significantly different. The full symbols in Fig. 5.11(a) for 6 K and Fig. 5.11(b) for 295 K denote the measured angle of rotation, as determined by $\phi_i - \phi_f$. Please check Appendix A for the details of the formulation and the experimental setup used for the measurement of the polarization rotation. The open symbols in Figs. 5.11(a) and 5.11(b) denote the calculated angle of rotation, which is determined using Eq. (5.49). The input parameters for these calculations are $T_\parallel$ and $T_\perp$ for the case of ϕ_i= 45°. The agreement between the measured and calculated curves is excellent. Note that the maximum polarization rotation at 295 K occurs near energy E = 3.44 eV (λ= 360 nm) as shown in Fig. 5.11(b). In this energy range, the ration $T_\perp / T_\parallel$ is smallest for the 0.7 μm-thick M-plane GaN film.

In comparison to ZnO, for which the largest measured rotation angle is 10° [139], the maximum measured rotation angle for M-plane GaN at 6 K is almost equal to 40°, which corresponds to about 90% of the incoming polarization angle of 45°. According to Eq. (5.49), the smaller the value of the ratio $T_\perp / T_\parallel$, the larger the experimentally achievable rotation angle. Since the shift of the energy gap between the two polarization directions is much larger for our M-plane GaN film than for the ZnO film in Ref. [139], the minimum value of the ratio $T_\perp / T_\parallel$ becomes much smaller for the GaN film in comparison to the ZnO film. This difference demonstrates the advantage of M-plane GaN over ZnO for devices based on polarization rotation. It should be noted that the experimentally determined rotation of the polarization vector is in very good agreement with the rotation calculated using Eq. (5.49), although assumption that the outgoing light is linearly polarized instead of being elliptically polarized has been made.

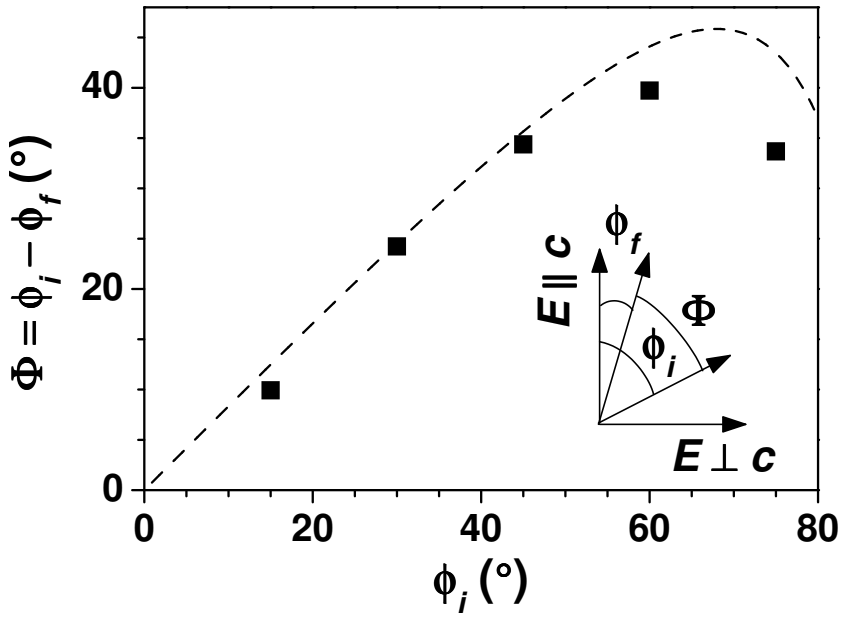

Figure 5.12: Measured (squares) and calculated (dashed line) static rotation angle Φ for $T_\perp/T_\parallel = 1/37$ versus ϕ_i for 360 nm at 300 K. The lower right inset shows the definition of the angles and polarization directions. The measurement is done for the 0.7 μm-thick M-plane GaN film.

5.1.7 Polarization rotation for linearly polarized light at arbitrary ϕ_i

In the previous section we studied the case for polarization rotation, when the incoming polarization angle was $\phi_i = 45°$. Let us now carry out the dependence of polarization rotation as a function of arbitrary incoming polarization angle ϕ_i. For such a case, Φ can be expressed by

$$\Phi = \phi_i - \arctan\left(\tan(\phi_i)\sqrt{\frac{T_\perp}{T_\parallel}}\right) , \tag{5.50}$$

where $T_\perp$ and $T_\parallel$ denote the corresponding transmittances. Eq. (5.50) indicates that the polarization filtering depends on three independent quantities, which are $T_\parallel$, $T_\perp$, and the incoming polarization angle ϕ_i. Choosing a particular sample fixes the transmittances along the two polarization directions ($T_\perp$ and $T_\parallel$). The rotation angle will therefore depend only on the incoming polarization angle. The variation of the rotation angle Φ as a function of the incoming angle is plotted in Fig. 5.12 for incoming angles between 0° and 90° for the 0.7 μm-thick M-plane GaN film. The experiment is done for our sample at λ=360 nm ($E = 3.444$ eV), where we know from the previous subsection that the rotation is maximum for ϕ_i= 45°. The measured rotation is shown as squares. For such a measurement, the light beam at 360 nm was derived from a second harmonic of a pulsed Ti-Sapphire laser at 720 nm. Its intensity is several orders of magnitude higher than the one for the light beam of the Xe-Arc lamp. It has been verified that the higher intensity of the light beam does not affect the experimental results.

The dashed line in Fig. 5.12 indicates the calculated value of Φ using Eq. (5.50) with a value of $T_\perp/T_\parallel = 1/37$, which was independently measured by detecting the transmittances for $\phi_i = 0$ and 90°. We find that the experimentally determined rotation values agree very well with the one calculated according to Eq. (5.50). The maximum static

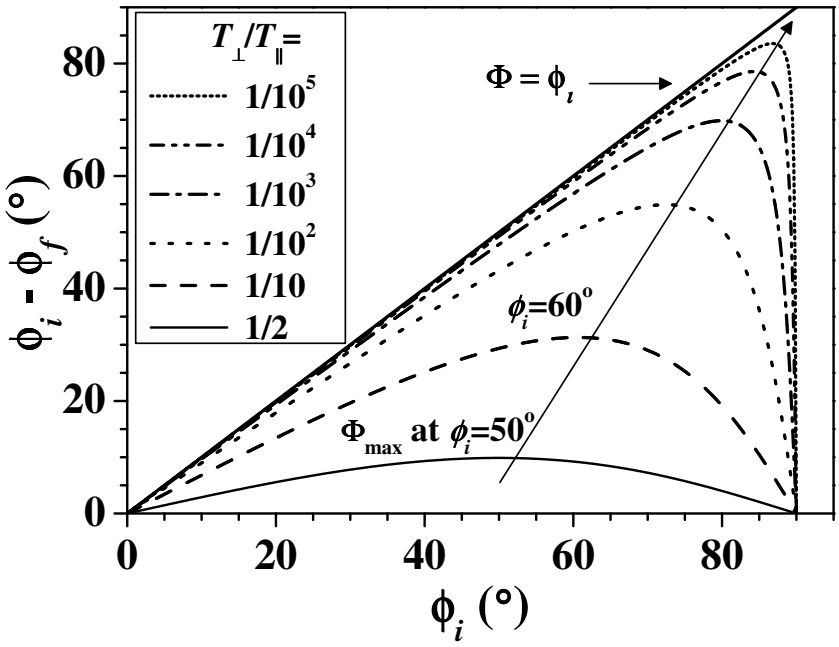

Figure 5.13: The degree of rotation $\Phi = \phi_i - \phi_f$ is calculated using the relation in Eq. (5.50). The input parameter is the transmittance ratio ($T_\perp/T_\parallel$) which is varied by 5 orders of magnitude. The arrow marks the position of ϕ_i where Φ, exhibits a maximum. The maximum achievable rotation shifts to higher values as the ratio $T_\perp/T_\parallel$ increases. The straight line denotes the function $\Phi = \phi_i$ which implies $\phi_f = 0$.

rotation of 40° is observed for $\phi_i = 60°$. Note that the maximum static rotation is solely determined by the value of the ratio $T_\perp/T_\parallel = a^2$, since $\Phi_{\max} = \arctan[(1-a)/(2\sqrt{a})]$, which becomes about 46° for $a^2 = 1/37$. The maximum rotation $\Phi_{\max}$ depends only on the ratio of the transmittances, i.e., $T_\perp/T_\parallel$, so the higher the ratio, the larger the rotation. The dependence of the degree of rotation Φ on the transmittance ratio a^2 is shown in Fig. 5.13. This ratio is varied over 5 orders of magnitude. Both the maximum value of the degree of rotation $\Phi_{\max}$ and the incoming angle ϕ_i corresponding to this maximum, shift towards higher values as the ratio a^2 is increased. Therefore, for the case of 0.7 μm-thick M-plane film, where the ratio a= 1/37 give the maximum rotation of about 40°. However, for the case of ZnO film in Ref. [139], this ratio is around 1/2 giving a maximum rotation of 10°, as plotted by solid line in Fig. 5.13.

5.1.8 Linear dichroism and birefringence in *M*-plane GaN

Figure 5.6 clearly shows that the calculated refractive indices for the electric field $\boldsymbol{E} \parallel \boldsymbol{c}$ and $\boldsymbol{E} \perp \boldsymbol{c}$ are different suggesting that M-plane GaN is a birefringent material. Similarly, Fig. 5.8 suggest that the absorption coefficient is also different along these two polarization directions signifying that the material also shows linear dichroism. The linear dichroism (LD) and linear birefringence (LB) of the M-plane GaN film are summarized in Fig. 5.14, showing the difference in the absorption coefficients $\Delta\alpha = \alpha_\perp - \alpha_\parallel$ and refractive indices $\Delta n = n_\perp - n_\parallel$, respectively. Note that the dichroism $\Delta\alpha$ becomes maximal in an energy region, where the birefringence Δn almost vanishes. The energy region between 3.4 and 3.5 eV is of particular interest, because in this range

the difference in the absorption coefficients is largest, while the difference in the indices of refraction is close to zero. In the transparent regime ($E < 3.4$ eV), $n_\perp < n_\parallel$ so that the birefringence is negative, while in the absorbing regime $n_\perp > n_\parallel$ and birefringence becomes positive. The absorption coefficient follows $\alpha_\perp > \alpha_\parallel$ in the transparent regime In the highly absorbing regime $\alpha_\perp < \alpha_\parallel$. Observation of LD and LB for light incident normal to the MQW structure is also reported in GaAs/(Al,Ga)As multiple quantum wells [31], where the optical anisotropy is due to thermally induced in-plane uniaxial strain. For this case, both LD and LB are due to the in-plane uniaxial strain in the system. For our case, however, both LD and LB exist due to the reduced symmetry of the crystal structure in addition to having contributions from the in-plane anisotropic strain. In order to separate the two contributions, unstrained *M*-plane GaN thin films will be required to determine the contribution of the reduced crystal symmetry alone.

5.1.9 Polarization rotation taking linear dichroism and linear birefringence into account

In the previous subsection, we made the assumption that the film is not linearly birefringent, while calculating the polarization filtering and rotation. This leads to the situation that the outgoing beam is linearly polarized. Generally, the outgoing light beam will not be linearly polarized, but rather elliptically polarized because of the linear birefringence of the material. The refractive indices for the two orthogonal polarization directions, $n_\parallel$ and $n_\perp$, are not equal so that the phase retardation for these two directions is different. After transmission through the film, the outgoing light is elliptically polarized as shown in Fig. 5.15 as opposed to the situation shown in Fig.

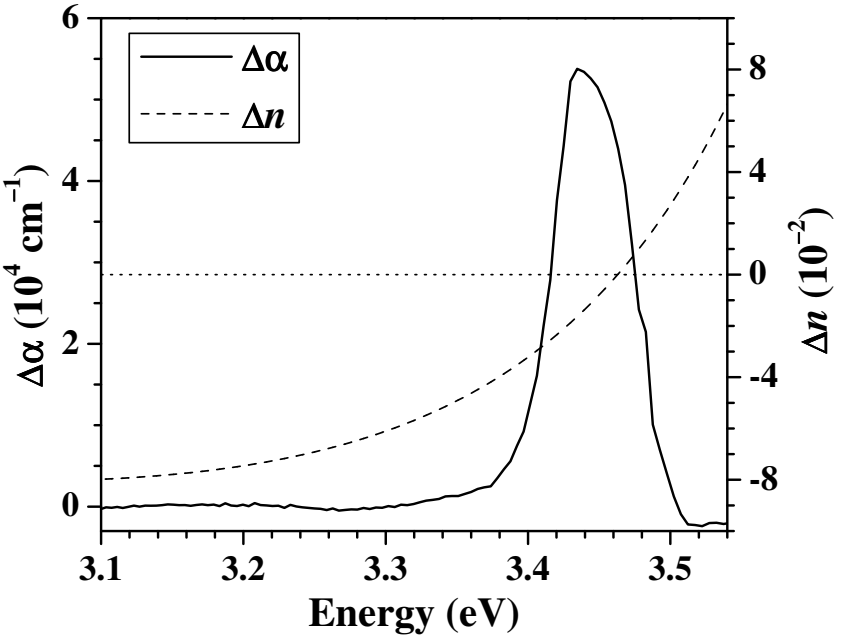

Figure 5.14: Linear dichroism $\Delta\alpha = \alpha_\perp - \alpha_\parallel$ (solid line) and linear birefringence $\Delta n = n_\perp - n_\parallel$ (dashed line) are plotted for the 0.7 μm-thick *M*-plane GaN film. The dotted line denotes zero linear birefringence, i.e., $n_\perp = n_\parallel$. The maximum in the linear dichroism occurs in the energy range near the band gap of GaN when the linear birefringence is almost zero.

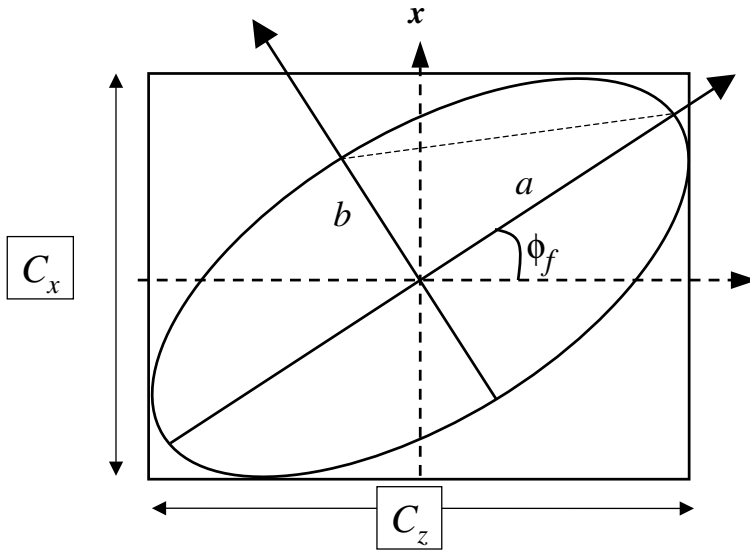

Figure 5.15: The outgoing light is elliptically polarized. The various angles are explained in the text.

5.10. The electric field components can be denoted as:

$$\begin{aligned} E_F^z &= |A_F^z| \exp[-i(\omega t - K_F y + \delta_\parallel)] \,, \\ E_F^x &= |A_F^x| \exp[-i(\omega t - K_F y + \delta_\perp)] \,. \end{aligned} \tag{5.51}$$

Using a simple trigonometric relation, we can reduce Eq. (5.51) to:

$$\left(\frac{E_F^z}{|A_F^z|}\right)^2 + \left(\frac{E_F^x}{|A_F^x|}\right)^2 - 2\frac{E_F^z E_F^x}{|A_F^z||A_F^x|}\cos(\delta) = \sin^2(\delta) \,, \tag{5.52}$$

where $\delta = \delta_\perp - \delta_\parallel$ denotes the phase retardation difference between the two orthogonal polarization directions [$t_{\parallel,\perp} = |t_{\parallel,\perp}| \exp(i\delta_{\parallel,\perp})$]. The above equation denotes an ellipse because the associated determinant is larger than zero.[126]

The angle ϕ_f now refers to the angle between the major axis of the polarization ellipse and the c axis. Defining an auxiliary angle by $\tan(\beta) = |A_F^x / A_F^z|$, ϕ_f and β, which are equal for the case of linear polarization of the outgoing light beam, will now be different. According to Ref. [126], ϕ_f and β are now related by

$$\tan(2\phi_f) = \tan(2\beta)\ \cos(\delta) \,. \tag{5.53}$$

This equation together with Eq. (5.38) in the form $\tan(\beta) = \tan(\phi_i)\ \sqrt{T_\perp / T_\parallel}$ determine ϕ_f. Note that now the polarization filtering or rotation also depends on δ, which is mainly determined by the refractive indices. Elliptically polarized light is usually described by the ellipticity η, defined as the ratio of the length b of the minor axis to the length a of the major axis of the polarization ellipse, i.e., $\eta = b/a$ (cf. Fig. 5.15 for details). Introducing an auxiliary angle χ by defining $\eta = \tan(\chi)$, the following relation between χ, β, and δ is obtained [126]

$$\sin(2\chi) = -\sin(2\beta)\sin(\delta) \,. \tag{5.54}$$

If $\delta = m\pi$ ($m = 0, 1, 2, ...$), the outgoing beam will be linearly polarized ($\eta = 0$). For an incoming polarization angle $\phi_i = 45^\circ$ and for $T_\parallel = T_\perp$, the outgoing beam becomes

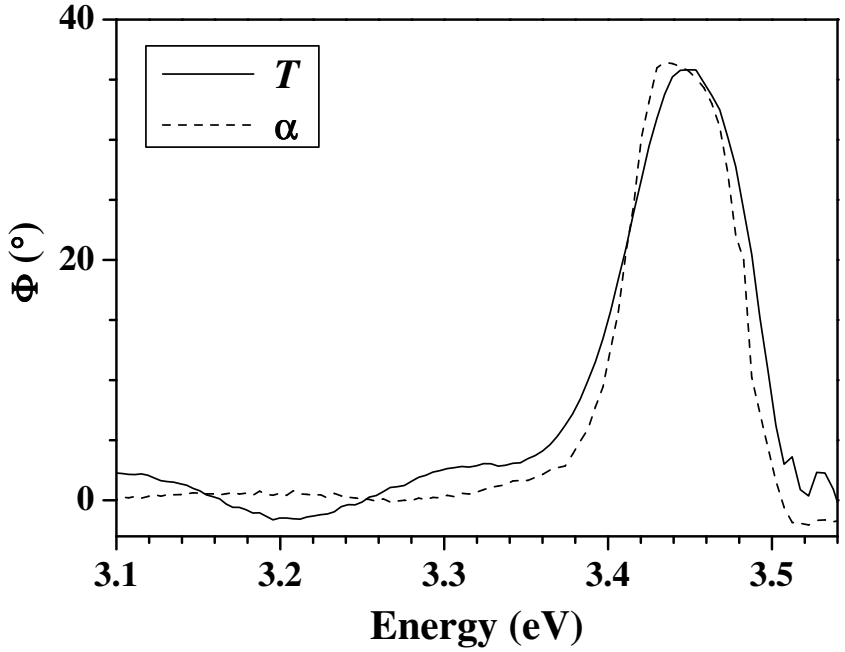

Figure 5.16: Rotation Φ versus energy for $\phi_i = 45°$ calculated using Eq. (5.48) with the ratio of the transmittances $T_\perp$ and $T_\parallel$ (solid line) and using Eq. (5.56) with the difference in the absorption coefficients $\Delta\alpha$ (dashed lines) for the 0.7 μm-thick M-plane GaN film at 295 K.

circularly polarized ($\eta = 1$), if $\delta = (2m+1)\pi/2$. For all other cases, the outgoing beam will be elliptically polarized.

In order to calculate the rotation of polarization due to the anisotropic filtering and phase retardation, we will make the following approximations in the absorbing regime, i.e., near the band gap of the respective material

$$\frac{T_\perp}{T_\parallel} \approx \exp(-\Delta\alpha d) \;\text{ and }\; \delta \approx \frac{2\pi\Delta n d}{\lambda}\,, \tag{5.55}$$

where $\Delta\alpha = \alpha_\perp - \alpha_\parallel$, and $\Delta n = n_\perp - n_\parallel$. For linear polarization of the outgoing light beam, the degree of rotation in Eq. (5.48) can now be approximated by

$$\Phi \approx \phi_i - \arctan[\tan(\phi_i)\exp(-\Delta\alpha d/2)]\,. \tag{5.56}$$

In order to prove that the above approximations are correct and that we can approximately describe the polarization filtering or rotation by the absorption coefficient and film thickness alone, we compare, for the case of no birefringence, the rotation Φ as a function of energy for $\phi_i = 45°$ calculated from Eqs. (5.48) and (5.56) in Fig. 5.16. For Eq. (5.48), the input parameters are the measured transmittances $T_\perp$ and $T_\parallel$, while for Eq. (5.56) they are the film thickness d and the difference in the absorption coefficients $\Delta\alpha$ as determined from the measured transmittances as well as reflectances. Both curves are in excellent agreement in the energy range, where we have a large difference in the transmittances (near the energy gap). A large value of the rotation is only obtained in the region, for which the transmittances and absorption coefficients are very different. In the transparency regime, the small non-zero values of Φ are due to the different location of the interference fringes in the respective transmittance spectra (cf. Fig. 5.4). The rotation calculated using the absorption coefficient is relatively free from

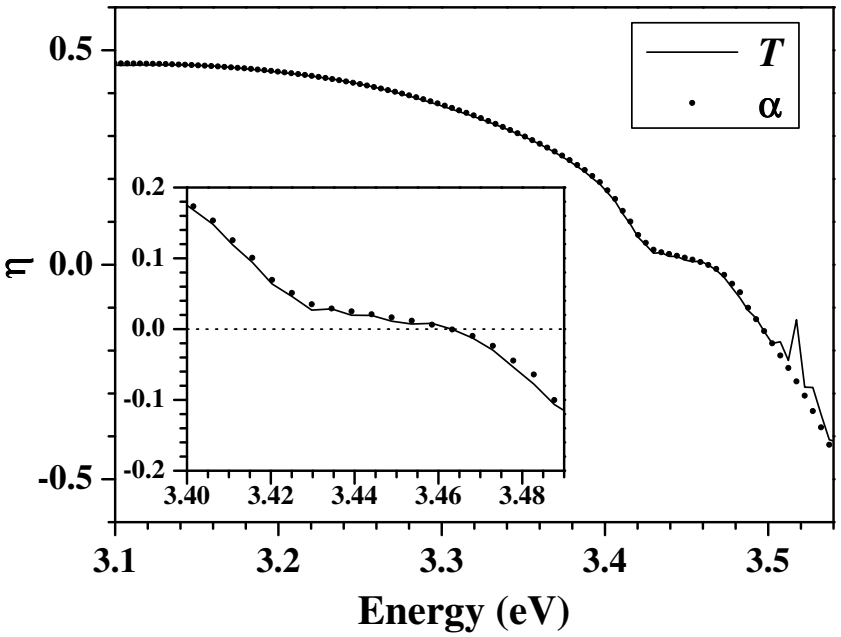

Figure 5.17: Ellipticity η versus energy for $\phi_i = 45°$ calculated using Eq. (5.54) with the transmittances $T_\perp$ and $T_\parallel$ (solid line) and using Eq. (5.58) with $\Delta\alpha$ (dots) for the 0.7 μm-thick M-plane GaN film at 295 K.

these small non-zero oscillations in the transparency regime, because the interference fringes are suppressed in the calculation of the absorption coefficient. The excellent agreement of the result for Φ using the approximate relation in Eq. (5.56) with the result for Φ using the exact relation in Eq. (5.48) indicates that the ratio of the transmittances can be rather well approximated by the difference of the absorption coefficient for the two polarization directions.

Now we will determine the effect of the birefringence of the GaN film on the ellipticity of the outgoing light beam. Applying the approximations of Eq. (5.55) to Eqs. (5.38) and (5.53), we obtain for elliptically polarized light

$$\tan(2\phi_f) \approx \tan(2\arctan[\tan(\phi_i)\exp(-\Delta\alpha d/2)]) \times \cos(2\pi\Delta n d/\lambda)\ . \tag{5.57}$$

For the ellipticity angle χ, Eq. (5.54) is reduced to

$$\sin(2\chi) \approx -\sin(2\arctan[\tan(\phi_i)\exp(-\Delta\alpha d/2)]) \times \sin(2\pi\Delta n d/\lambda)\ . \tag{5.58}$$

Figure 5.17 shows the ellipticity η as a function of energy for $\phi_i = 45°$ calculated from Eqs. (5.54) and (5.58). In addition to the indices of refraction, the input parameters for Eq. (5.54) are the measured transmittances $T_\perp$ and $T_\parallel$, while for Eq. (5.58) we use $\Delta\alpha$ as derived from the measured transmittances and reflectances as an input parameter. Both calculated values of η agree very well over the whole energy range. The inset of Fig. 5.17 displays the ellipticity in the energy range of effective polarization filtering. At room temperature, the ellipticity becomes basically zero where the filtering is most effective (3.444 eV) due to almost identical refractive indices, i.e., $n_\perp \approx n_\parallel$, as shown in Fig. 5.14. Note that the large difference in the absorption coefficients in this energy range does not guarantee a vanishing ellipticity, since the product of $\Delta\alpha d/2$ determines the contribution of the first term in Eq. (5.58), which in our case is 1.75. We conclude

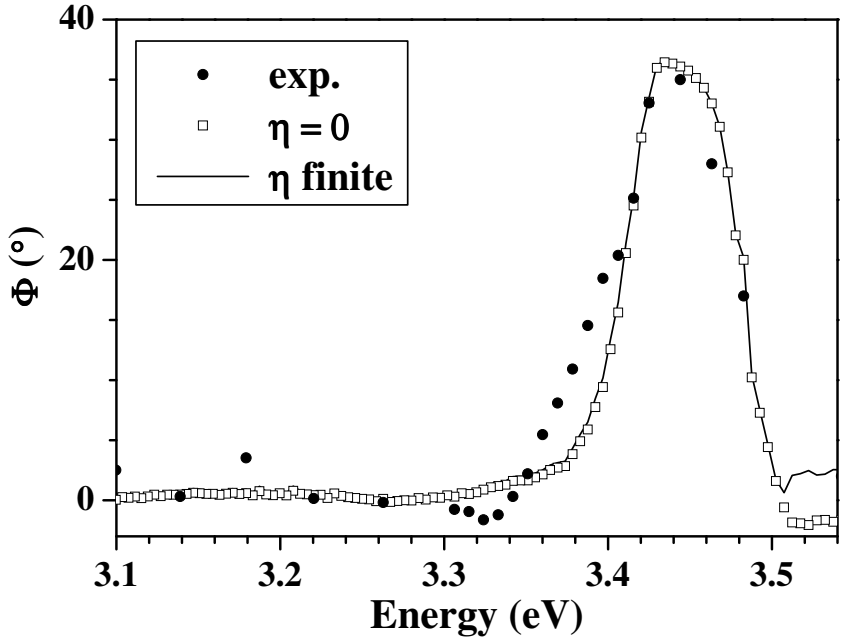

Figure 5.18: Rotation Φ versus energy for $\phi_i = 45°$ measured for the 0.7 μm-thick M-plane GaN film at 295 K (dots) in comparison with the calculated values using Eq. (5.56), i.e., $\eta = 0$ (open squares), and Eq. (5.57), i.e., finite ellipticity (solid line).

that in the vicinity of 3.444 eV, the outgoing beam is almost linearly polarized rather than elliptically polarized, since no phase retardation of one polarization with respect to the orthogonal one occurs. In this energy regime, only linear dichroism, which results in polarization filtering, has to be considered.

Next we will compare the measured polarization rotation with values calculated from Eqs. (5.56) and (5.57). Figure 5.18 shows the energy dependence of the measured rotation Φ for $\phi_i = 45°$ and the calculated values. For Eq. (5.56), $\eta = 0$, while for Eq. (5.57) the ellipticity is non-zero. As expected, the calculated results are in excellent agreement with each other except for high energies, where the transmission through the sample becomes rather small for both polarization directions. At the same time, the experimental values are well reproduced by the calculated ones within the experimental uncertainty. This agreement implies that the contribution of phase retardation to the rotation is negligible in the region, where $\Delta\alpha \neq 0$. The experimentally measured rotation of polarization is as high as 36° at room temperature and reaches even 40° at low temperatures.[34] In contrast to previously published values for A-plane ZnO of about 10° for the same initial angle [139], the M-plane GaN film exhibits a much higher value. The reason for this is the much larger polarization anisotropy in the absorption coefficient of the M-plane GaN film on $LiAlO_2$ in comparison to the A-plane ZnO film on R-plane sapphire, which occurs due to the large anisotropic strain in the M-plane GaN film. According to Eqs. (5.56) and (5.58), the polarization angle of the outgoing beam depends on the thickness of the GaN film. However, since $\Delta\alpha$ decreases with increasing film thickness due to a decreasing in-plane strain [22, 55], the polarization filtering may remain the same or even decrease. As shown in Fig. 3.3, the out-of-plane strain depends on the thickness of the film with the maximum strain. We find that for film thicknesses up to about 0.7 μm, the anisotropic strain is largest resulting in the

most effective polarization filtering.

5.1.10 Dynamic polarization filtering in *M*-plane GaN films

In the previous subsection, we studied the static polarization filtering and rotation of the polarization vector and the time dependence of these properties were not discussed. We have shown that the degree of polarization rotation depends on the ratio of the transmittance perpendicular ($T_\perp$) and parallel ($T_\parallel$) to the c axis. The transmittances $T_\perp$ and $T_\parallel$ are related to the transition from the highest ($|X\rangle$-like) and second-highest ($|Z\rangle$-like) VB state. The polarization filtering is maximum in the energy region where the absorption coefficient are significantly different, i.e., the film shows maximum linear dichroism. This polarization rotation can be modulated by selective photoexcitation, since the photoexcited carriers bleach the anisotropic absorption and remove the static linear dichroism.

To investigate the dynamic behavior of the polarization filtering, we performed time-resolved transmittance spectroscopy using the degenerate pump-and-probe technique. The pump and probe were adjusted to 360 nm (3.44 eV) using the second harmonic of a femtosecond Ti:Sapphire laser, since the film shows the largest difference of the absorption coefficients $\alpha_\perp - \alpha_\parallel$ at this wavelength. The effectiveness of the filtering of the incoming polarization vector with an angle ϕ_i with respect to the outgoing polarization vector with an angle ϕ_f, can be quantified by the difference $\Phi(t)$ as

$$\begin{aligned} \Phi(t) &= \phi_i - \phi_f \\ &= \phi_i - \arctan\left(\sqrt{\frac{I_\perp(t)}{I_\parallel(t)}}\right), \end{aligned} \tag{5.59}$$

where $I_\perp(t)$ and $I_\parallel(t)$ are the transmitted intensities perpendicular and parallel to the c axis, respectively and t denotes the time delay between the pump and the probe.

We find that the static rotation is almost compensated by the bleaching of the absorption due to photoexcited carriers and the polarization vector is rotated away from the c axis. This is in contrast to the static rotation where the polarization vector rotates towards the c axis and has a value of 40° for incoming polarization angle of ϕ_i=60°. The maximum dynamic rotation becomes largest for ϕ_i=60° with a value of 35° at zero time delay between the pump and the probe. Since the bleaching almost removes the static anisotropy of absorption coefficient, the maximum dynamic rotation occurs for the same value of ϕ_i as the maximum static rotation (cf. Fig. 5.12). This type of optical in-plane polarization anisotropy in semiconductors can be used to realize an optical modulator, which has both a high contrast and a fast response.[31, 33]

5.2 Summary

We have demonstrated that the polarization filtering in *M*-plane GaN films due to linear dichroism gives rise to a rotation of the in-plane polarization vector as large as 40° after transmission. The degree of rotation can be accurately described in terms of the

transmittances for two orthogonal polarization directions, where one of them is parallel to the c axis of the GaN film. The polarization filtering and polarization rotation is maximum in the energy region where the ratio of the transmittances is minimum and the film shows maximum linear dichroism. Furthermore, the rotation can be very well approximated by the product of the film thickness and the difference of the absorption coefficients for the two polarization directions. The contribution of the linear birefringence to the rotation is negligible in the energy range, for which the polarization filtering is most effective. Finally, the static optical anisotropy of the absorption coefficient is almost removed by bleaching of the absorption due to the photoexcited carriers of the pump as shown using degenerate pump-and-probe spectroscopy. The maximum dynamic rotation is measured to be as large as 35° for a incoming polarization angle of $\phi_i = 60^\circ$.

Chapter 6

Polarization anisotropy of photoluminescence spectra

In the preceding chapters, we have focused on the in-plane polarization anisotropy in absorption. In this chapter, we will study the in-plane polarization anisotropy in emission.

The emitted photoluminescence intensity I_{PL} per unit energy is given by:

$$I_{\mathrm{PL}}(\hbar\omega) = \text{Const.} \times \alpha(\hbar\omega)\omega^3 \frac{1}{\exp(\hbar\omega/k_BT) - 1} \,, \tag{6.1}$$

where $\alpha(\hbar\omega)$ is the absorption coefficient which can be related to the individual optical transition probability element by:

$$\begin{aligned} \alpha(\omega) &= \frac{8\pi^2e^2}{n(\omega)c\omega m^2} \sum_{v,c}\sum_{K} |\hat{\mathfrak{e}} \cdot \mathbf{P}_{v,c}(K)|^2 \times \delta(E_c(K) - E_v(K) - \hbar\omega) \,, \\ &= \frac{8\pi^2e^2}{n(\omega)c\omega m^2} \sum_{v,c}\sum_{K} [\cos(\phi_{pl})P^z_{v,c}(K) + \sin(\phi_{pl})P^x_{v,c}(K)]^2 \times \delta(...) \,. \end{aligned} \tag{6.2}$$

where $\vec{P}^z_{v,c}$ ($\vec{P}^x_{v,c}$) is the z-(x-) component of the momentum matrix element. ϕ_{pl} is the angle the polarization vector $\hat{\mathfrak{e}}$ makes with the c axis of GaN, such that the general direction of the polarization vector $\hat{\mathfrak{e}}$ in M-plane GaN for a wave travelling along y axis can be written as (sin(ϕ_{pl}),0,cos(ϕ_{pl})). Combining Eqs. (6.1) and (6.2), we obtain for the total PL intensity I_{tot}:

$$I_{\mathrm{tot}}(\phi_{pl}) = I_{\parallel}\cos^2(\phi_{pl}) + I_{\perp}\sin^2(\phi_{pl}) + I_{zx}\sin(\phi_{pl})\cos(\phi_{pl}) \,, \tag{6.3}$$

where $I_{\perp}(I_{\parallel})$ denotes the PL intensity for light polarized perpendicular (parallel) to the c axis, while the term I_{zx} denotes the emission due to valence-band mixing. The individual component for I_{zx} for our value of strain is zero because each state is either purely $|Z\rangle$- or $|X\rangle$-like. The above relation can be simplified to:

$$\frac{I_{\mathrm{tot}}(\phi_{pl})}{I_{\perp}} = \frac{I_{\parallel}}{I_{\perp}}\cos^2(\phi_{pl}) + \sin^2(\phi_{pl}) \,. \tag{6.4}$$

The equation relating the PL intensity to the arbitrary in-plane polarization angle ϕ_{pl} is similar to the Eq. (5.37) achieved for transmittance in Chapter 5. We investigate

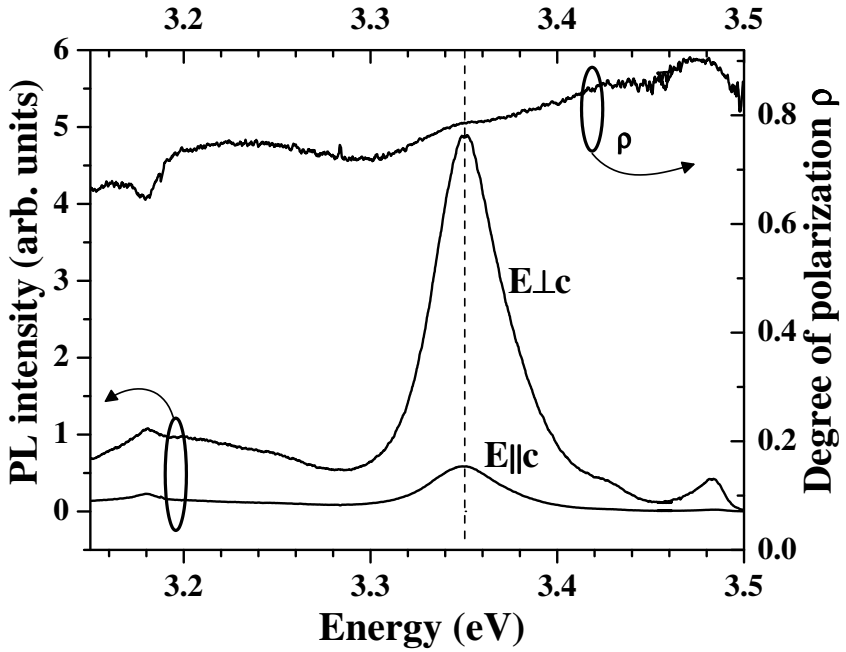

Figure 6.1: photoluminescence (PL) and Degree of polarization ρ for the 0.7 μm-thick *M*-plane GaN film measured at 5K. The polarization degree is as high as 0.9 and slowly decreases to 0.75 with decreasing energy. The PL peak position does not shift when the incoming electric field is rotated by 90° from $\boldsymbol{E} \parallel \boldsymbol{c}$ to $\boldsymbol{E} \perp \boldsymbol{c}$.

the in-plane polarization anisotropy in emission for both the low-temperature regime and at temperatures above room temperature.

In order to study the polarization anisotropy, the degree of polarization is usually used, and is defined as:

$$\rho = \frac{I_{\perp} - I_{\parallel}}{I_{\perp} + I_{\parallel}} \,. \tag{6.5}$$

The study of the degree of polarization yields additional information about the electronic structure of the emitting semiconductors and the dynamic processes that occur during the lifetime of the excited state. In uniaxial crystals such as GaN, it is possible to use degree of polarization to study the excitation mechanism and band structure. [140, 141]

The experimental setup for the measurement of in-plane polarization anisotropy in emission is as follows: The excitation source is He-Cd laser at 325nm (3.812 eV), while the polarized luminescence is collected by using a Glan-Taylor prism placed between the sample and the monochromator. The collected luminescence is corrected for the polarization dependence of the setup.

6.1 *M*-plane GaN thin films

Figure 6.1 shows the polarization-dependent low-temperature PL spectra and the degree of polarization of the 0.7 μm-thick *M*-plane GaN film. Note that the PL peak position at 3.350 eV is ascribed to excitons bound to stacking faults (SF,X), while the other peak around 3.484 eV is related to excitons bound to donors (D°,X) (cf. Chapter

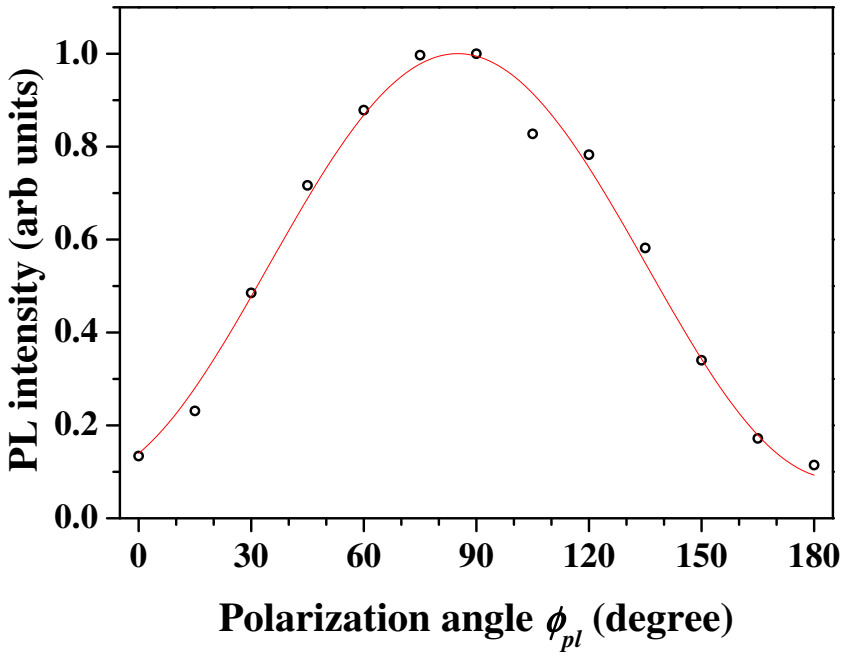

Figure 6.2: Spectrally integrated PL intensity at 5 K of the 0.7 μm-thick *M*-plane GaN film as a function of polarization angle ϕ_{pl}. The fit using Eq. (6.4) shown by the solid line agrees very well with the experimental data plotted as symbols. An angle of 90° describes the case of $\boldsymbol{E}\perp\boldsymbol{c}$.

4). The PL intensity for both the peaks decreases as the polarization for the detected signal is rotated from $\boldsymbol{E} \perp \boldsymbol{c}$ to $\boldsymbol{E} \parallel \boldsymbol{c}$. This can be explained using Eq. (6.2), where the polarization of the spontaneous emission is determined by the interband dipole matrix elements, which in turn follow the selection rules arising from the valence band structure of *M*-plane GaN under biaxial, anisotropic in-plane strain. At low temperatures, the top-most valence band, which has $|X\rangle$-like VB state is occupied while the second highest $|Z\rangle$-like VB state remains empty (cf. Fig. 4.6). The transition between the CB and the $|X\rangle$-like VB state gives rise to a high intensity, because the occupation is high. However, when the detected polarization is parallel to the *c* axis, the PL intensity corresponds to the transition between CB state and $|Z\rangle$-like VB state. Since the occupation of this VB state is low, the PL intensity is very small.

Figure 6.1 also shows the degree of polarization obtained for *M*-plane GaN at low temperatures. ρ can be as high as 0.9 at higher energies and gradually decreases to 0.75 with decreasing energy. This high degree of polarization is due to the large valence band splitting between the two top-most VB states, which is as large as 60 meV at low temperatures. Therefore, only the top-most (*X*-like) state is occupied. The relation $I_\perp \gg I_\parallel$ holds, which simplifies Eq. (6.4) to $I_{\text{tot}}=I_\perp \sin^2(\phi_{pl})$. The PL has also been measured for $0° < \phi_{pl} < 180°$. The resulting spectrally integrated PL intensity is plotted versus ϕ_{pl} in Fig. 6.2 as symbols. The data are fitted with Eq. (6.4) and the resulting fit is shown in the figure as solid line. The fit agrees well with the experimental data. The small value of the ratio $I_\parallel / I_\perp$ suggests that the PL is mostly $|X\rangle$-like polarized. We emphasize that the total width of the PL band is much larger than the valence band splitting. Since we do not observe any spectral shift in the PL spectra between $\boldsymbol{E}\perp\boldsymbol{c}$ and $\boldsymbol{E}\parallel\boldsymbol{c}$, we attribute the emission to a band of localized states, each of which are only

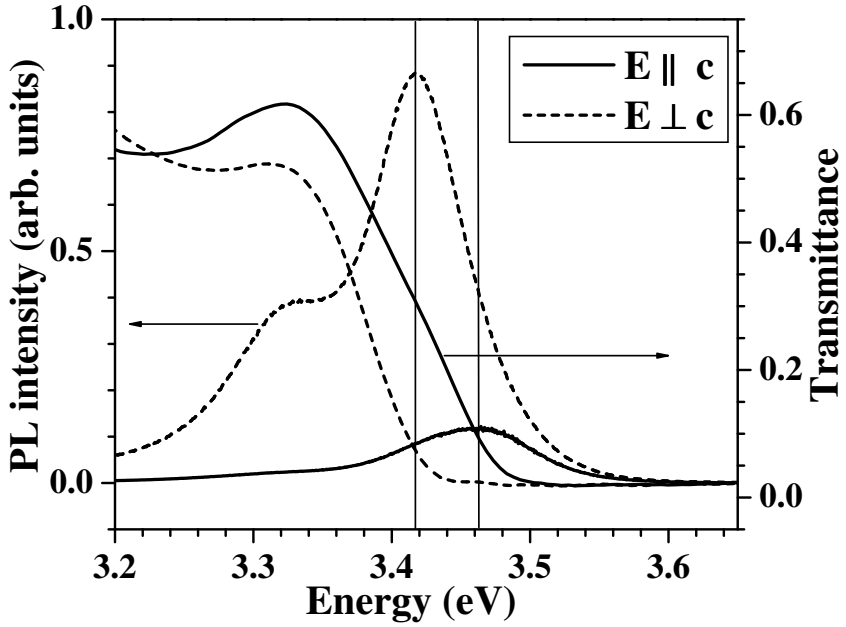

Figure 6.3: PL and transmittance spectra for the 0.5 μm-thick *M*-plane GaN film at 300 K for polarizations $\boldsymbol{E} \parallel \boldsymbol{c}$ and $\boldsymbol{E} \perp \boldsymbol{c}$. Both the measurement shows an energy shift towards higher energy when $\boldsymbol{E}$ is rotated from $\perp \boldsymbol{c}$ to $\parallel \boldsymbol{c}$.

occupied with T_1 excitons. This implies a very fast thermalization compared to the exciton lifetime. Any occupation of T_2 states leads to components $\boldsymbol{E}\|\boldsymbol{c}$ at higher PL energies.

At elevated temperatures, however, one would expect an occupation of both VB states. Figure 6.3 shows the comparison of the PL and transmittance spectra for the 0.5 μm-thick *M*-plane GaN film at room temperature measured for the polarizations $\boldsymbol{E} \parallel \boldsymbol{c}$ and $\boldsymbol{E} \perp \boldsymbol{c}$. The PL peak energy as well as the absorption edge in the transmittance spectra shift by 50 meV to higher energy, when the polarization is changed from $\boldsymbol{E} \perp \boldsymbol{c}$ to $\boldsymbol{E} \parallel \boldsymbol{c}$. Although the transmittance (absorption coefficient) at the corresponding peak position, indicated by the vertical lines, is almost the same for both polarization directions, the PL intensity for $\boldsymbol{E} \parallel \boldsymbol{c}$ is much smaller than for $\boldsymbol{E} \perp \boldsymbol{c}$. This is because even at 300 K the energy states of the second VB are much less occupied. The peak at 3.325 eV, which is clearly visible in the spectrum for $\boldsymbol{E} \perp \boldsymbol{c}$, is also present in the spectrum for $\boldsymbol{E} \parallel \boldsymbol{c}$ at exactly the same energy, although not clearly resolved in Fig. 6.3. Since the separation between the two uppermost VB's is considerably larger than the thermal energy at 300 K (26 meV), it is necessary to measure the PL at much higher temperatures in order to obtain a significant occupation of the second VB with holes.

Figure 6.4 shows the spectrally resolved degree of polarization ρ as a function of temperature for a 0.5 μm-thick *M*-plane GaN film. As expected, ρ decreases from a value of 0.9 at 300 K to about 0.5 at about 700 K with increasing temperature. As the occupation in the second-highest VB state ($|Z\rangle$-like) increases with increasing temperature, $I_{\parallel}$ corresponding to $\boldsymbol{E}\|\boldsymbol{c}$, increases. The ratio $I_{\parallel}/I_{\perp}$ gets smaller and the numerator in $\rho = (1 - I_{\parallel}/I_{\perp})/((1 + I_{\parallel}/I_{\perp}))$ decreases while the denominator increases. Therefore, the degree of polarization decrease with increasing temperature. Moreover,

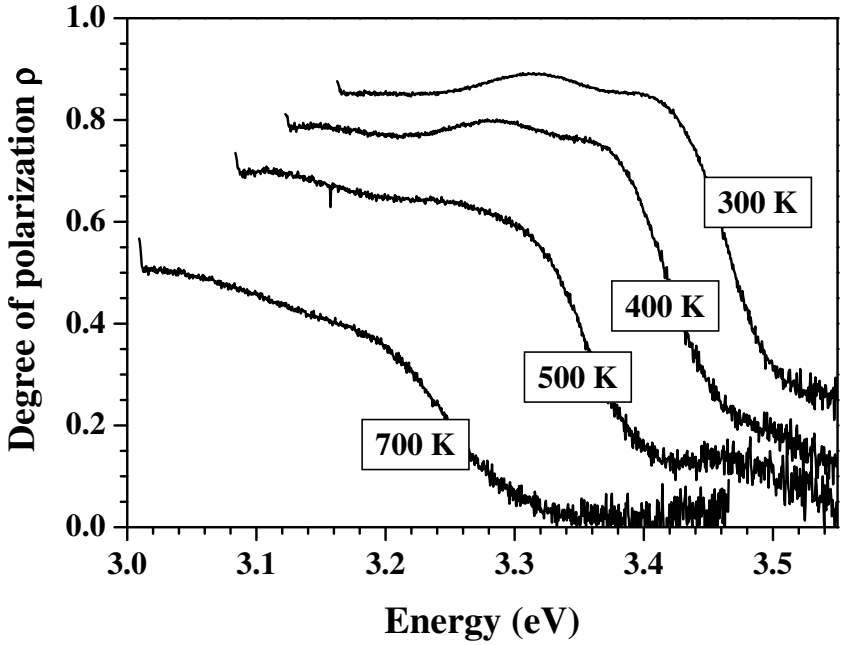

Figure 6.4: The degree of polarization as a function of temperature for the 0.5 μm-thick *M*-plane GaN calculated using Eq. (6.5). The measurement for $I_{\|}$ and $I_{\perp}$ is done from room temperature till 400 °C.

ρ is not constant over the whole energy range but starts to decrease around the energy maximum of $I_{\|}$, as opposed to a more uniform value at low temperature (cf. Fig. 6.1).

The difference in the energy gap between the top two valence band states can be estimated by varying the temperature for this 0.5 μm-thick sample and measuring the polarization ratio of the PL. [142] We plot the ratio $I_{\perp}/I_{\|}$ in Fig. 6.5 as a function of the inverse temperature. An Arrhenius relation is used to fit the data, which gives an activation energy of about 63 meV. This is close to the separation of around 50 meV estimated from the transmittance spectra depicted in Fig. 6.3. The difference may be due to the inaccurate calculation of exact band gap energy by transmittance due to the presence of band tail states as was discussed in the last chapter. Also the separation of the VB state depends on the in-plane strain in the film. The value of the in-plane strain can different at elevated temperatures can be different, as compared to the value at room temperature due to the thermal expansion coefficient mismatch between the substrate and GaN.

6.2 *A*-plane GaN thin films

We will now study the in-plane polarization anisotropy in emission for the *A*-plane GaN thin film grown on *R*-plane sapphire. The sample is 1 μm-thick. The details of the growth conditions, the sample structure, and the structural properties were discussed in Chapter 3. The polarized PL spectra measured for $\boldsymbol{E} \parallel \boldsymbol{c}$ and $\boldsymbol{E} \perp \boldsymbol{c}$ at 5 K are shown in Fig. 6.6. The spectra at low temperatures are dominated by peaks at 3.487 eV ascribed to the (D°,X) while the peak near 3.32 eV is related to the (SF,X) transition. There is another peak lying 60 meV below the (D°,X) transition at 3.425 eV, which is the dominant peak. The origin of such a transition is not clear and can be treated as

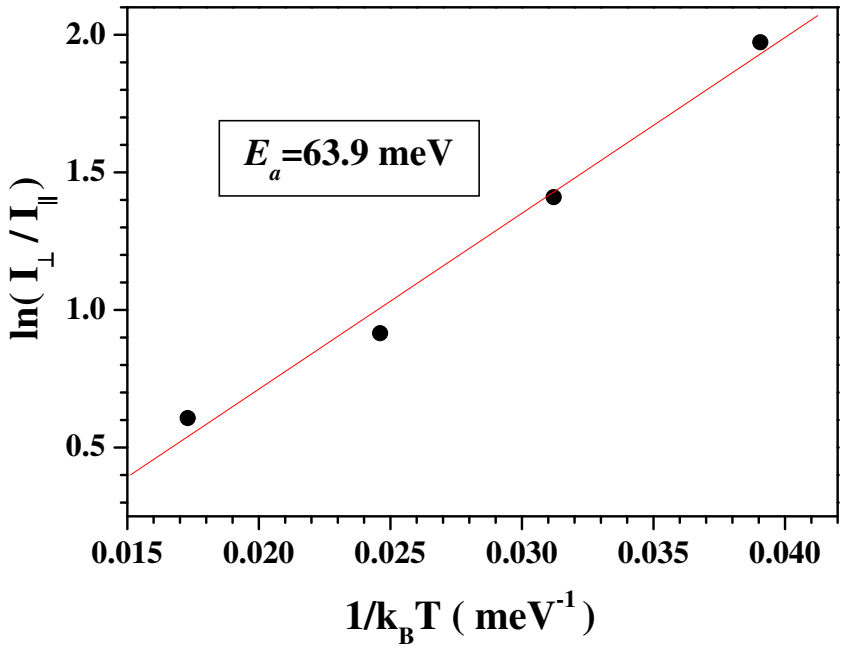

Figure 6.5: The data plotted (dots) in an Arrhenius relationship with the fitted activation energy of 63.5 meV shown as solid line for the 0.5 μm-thick *M*-plane GaN film, when the temperature is increased from room temperature to 400 °C. $I_{\perp}$ ($I_{\parallel}$) denotes the integrated PL intensity for $\boldsymbol{E}\perp\boldsymbol{c}$ ($\boldsymbol{E}\parallel\boldsymbol{c}$).

an anomalous peak. Several groups have reported the presence of anomalous peaks in GaN. [143] The peak around 3.42 eV has been observed by other groups, and the origin of this line is ascribed to excitons bound to structural defects on the surface.[143] Further analysis needs to be done in order to verify, if this is the case for our sample. The

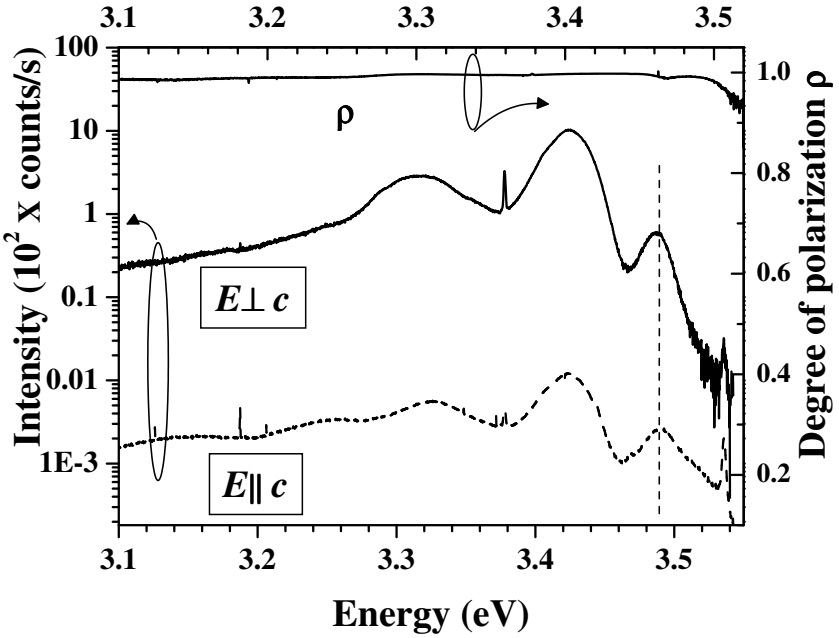

Figure 6.6: The polarization dependent cw-PL spectra for the 1 μm-thick *A*-plane GaN thin film on sapphire at 5 K. The measurement is done for $\boldsymbol{E}\perp\boldsymbol{c}$ and $\boldsymbol{E}\parallel\boldsymbol{c}$. The figure also shows the degree of polarization ρ, which attains a value of 0.98 for most of the energy range.

PL intensity for $\boldsymbol{E} \perp \boldsymbol{c}$ is 2 orders of magnitude higher than for $\boldsymbol{E} \parallel \boldsymbol{c}$ which can be explained by the band structure discussed in Chapter 2. At low temperature, the topmost Y-like VB states are mostly occupied. However, the second-highest or the third-highest VB states, both of which have Z-like wave characteristics are unoccupied. Therefore, $I_{\parallel} \ll I_{\perp}$ Fig. 6.6 also shows the spectrally resolved degree of polarization which has a value of 0.98 for most of the energy range. Although, the energy separation between the top two VB states is 10 meV for A-plane GaN thin film compared to a much higher value of 50 meV for M-plane GaN thin film, the degree of polarization is higher for the A-plane sample. This ambiguity may me related to the origin of the PL signal at 3.425 eV and further analysis needs to be done to explain the results.

6.3 Summary

In this chapter we studied the in-plane polarization anisotropy in emission for M- and A-plane GaN thin films at low and elevated temperatures. The results of the in-plane polarization anisotropy can be explained in terms of the band structure calculation done in Chapter 2. The degree of polarization is determined and is as high as 0.9 for M-plane and 0.98 for A-plane GaN at 5 K.

Chapter 7

Conclusions and outlook

In this work, we have studied the optical properties of *C*-, *M*-, and *A*-plane GaN thin films. It is found that the optical polarization response for a thin film strongly depends on the growth direction due to the different symmetry and the nature of the in-plane strain. We observe that no strain or isotropic strain in the *C* plane preserves the symmetry in the *x*-*y* plane of the WZ-GaN lattice so that no significant in-plane optical polarization anisotropy occurs. For anisotropic strain in the *C* plane, an in-plane anisotropy can arise. The situation is completely different for *M*- or *A*-plane GaN thin films, where the unique *c* axis lies in the growth plane. Here, even in the absence of an in-plane strain, one expects to see an in-plane polarization anisotropy. It is observed that any biaxial, anisotropic in-plane strain further lifts the symmetry of the *x*-*y* plane of the WZ-GaN lattice. Theoretical calculations using the $\mathbf{k}\cdot\mathbf{p}$ perturbation approach to calculate the band structure modifications suggests that, while in the absence of any strain the top two VB states have wave functions with identical symmetry, this is no longer true in the presence of biaxial strain in the *M* or *A* plane. This change in symmetry affects the polarization selections rules for the interband transitions. We found that the dependence of the transition energies and the value of the oscillator strengths for an *A*-plane GaN on the in-plane strain are similar to the case for *M*-plane GaN except for the exchange of *x* and *y* axis.

The transitions involving the electrons in the conduction band and holes in the top three valence bands are termed as the T_1, T_2, and T_3 transitions. The band-structure calculations reveal that for large biaxial, compressive in-plane strain in the *M* plane the transitions T_1, T_2, and T_3 are predominantly *x*, *z*, and *y* polarized, respectively. Therefore, in *M*-plane GaN thin films, for normal incident light beam, one expects to see a single dominant transitions for electric field vector $\boldsymbol{E} \perp \boldsymbol{c}$ and another single dominant transition for $\boldsymbol{E} \parallel \boldsymbol{c}$. This is experimentally verified by measuring the polarization-dependent transmittance, reflectance, photoluminescence, and photoreflectance. The independence of the transitions along the fundamental directions is verified by measuring the transmission spectra as a function of the polarization angle of a linearly polarized light. The transmission spectrum for an arbitrary in-plane polarization angle is a linear combination of the transmission spectra originating from the two transitions with polarizations parallel and perpendicular to the *c* axis.

A consequence of the in-plane polarization anisotropy is polarization filtering in the

energy range where the transmittance (absorption) along the fundamental directions is significantly different. This polarization filtering leads to a rotation of the polarization vector toward the *c* axis after transmission through the film. In this work, we present a detailed theoretical and experimental investigation of the in-plane optical polarization filtering of *M*-plane GaN films grown on γ-$LiAlO_2$(100). In addition to linear birefringence, the film also exhibits linear dichroism, resulting in a very effective polarization filtering near the band gap. We have included both the linear dichroism and linear birefringence effects to describe the polarization filtering, which can be detected as a rotation of the in-plane polarization vector. For an initial polarization angle of 45°, the measured polarization rotation can be as large as 36° at room temperature. In addition to the polarization angle of the incoming light beam, the rotation angle is determined by the ratio of the transmittances of the two orthogonal polarization directions, where one of them is parallel to the *c* axis. We show that the rotation angle can be approximately described by the exponential of the film thickness times the difference in the absorption coefficients for the two polarization directions. Although the outgoing light is generally elliptically polarized, it turns out that, in the energy range where polarization filtering is most effective, the linear birefringence almost vanishes. The study of dynamic rotation is also carried out and we find that the polarization rotation can be modulated by selective photoexcitation, since the photoexcited carriers bleach the anisotropic absorption and remove the static linear dichroism. Additionally, the in-plane polarization anisotropy in emission for the *M*- and *A*-plane is studied and this anisotropy in explained in terms of the band structure.

Outlook: The optically anisotropic response for semiconductors such as nonpolar GaN can be used to fabricate devices, in which the state of polarization is of critical importance for optical information processing. *M*-plane GaN is a promising candidate for the realization of polarization-sensitive photodetectors (PSPDs), because it is intrinsically sensitive to optical polarization. The advantage of intrinsically anisotropic material for the fabrication of PSPDs is that it allows for the miniaturization of the detection system, leading to large-scale integration and easier alignment because no external polarizing element is needed. Furthermore, nonpolar GaN can be used for the fabrication of optical modulators based on the rotation of the polarization vector, which has both a high contrast and fast response. In such a device, the polarization rotation can be modulated by selective photoexcitation. Intrinsically anisotropic nonpolar GaN can also be used for devices such as tunable polarization converter, polarization threshold switches and polarized light emitting diodes as well as device features such as polarization stabilization of vertical cavity surface emitting lasers.

Appendix A

Mathematical and experimental determination of polarization filtering

A.1 A mathematical framework for the measurement of polarization rotation

In the Mueller calculus, the light beam is represented by a vector called the Stokes vector, and the optical element encountered by the beam is represented by a matrix called the Mueller Matrix. [144] The two are multiplied to yield another vector representing the light beam after interaction with the optical element. The Mueller calculus can treat partially polarized light as well as fully polarized light and has this advantage over the Jones calculus which is more applicable if one is dealing with the phase of the electric field as the phase information is retained. So if one is dealing with polarized light beam and polarization optics one should use Mueller calculus but on the other hand solving multiple reflections and transmission at the interfaces one should use Jones calculus because the phase information is important in this case.

A.1.1 Mueller calculus : Stokes vector & Mueller matrix

The vector representing the light beam has four elements. The parameter of the Stokes vector represent intensities, therefore all elements are real. The Stokes vector **S** is defines as

$$\mathbf{S} = \begin{pmatrix} I \\ C \\ M \\ S \end{pmatrix} \tag{A.1}$$

where
I is the total intensity,
$C = I_{0^\circ} - I_{90^\circ}$ the difference in intensities between horizontally and vertically linearly polarized light,
$M = I_{-45^\circ} - I_{45^\circ}$ the difference in intensities between linearly polarized light oriented at +45° and -45°, and
$S = I_{rcp} - I_{lcp}$ the difference in intensities between right circularly polarized and left circularly polarized light.

A few example at this point are instructive. They include the Stokes vector for
a) linear polarization oriented at an angle α with x axis $\mathbf{S}_\alpha$ = (1,cos 2α,sin 2α,0).
b) Elliptically polarized light with major axis at an angle α to the x axis and tan(χ) is the ellipticity. $\mathbf{S}_{\alpha\omega}$ = (1,cos 2χ cos 2α,cos 2χ sin 2α,sin 2χ).

In order to write the interaction between the light beam defined by the Stokes vector and the optical element, which we wish to write as a Mueller matrix we need to know how a Stokes vector is changed by this interaction.

$$\begin{pmatrix} I' \\ C' \\ M' \\ S' \end{pmatrix} = \begin{pmatrix} m_{11} & m_{12} & m_{13} & m_{14} \\ m_{21} & m_{22} & m_{23} & m_{24} \\ m_{31} & m_{32} & m_{33} & m_{34} \\ m_{41} & m_{42} & m_{43} & m_{44} \end{pmatrix} \begin{pmatrix} I \\ C \\ M \\ S \end{pmatrix}, \tag{A.2}$$

or $\mathbf{S}' = \mathfrak{M}\mathbf{S}$ where $\mathfrak{M}$ is the 4 $\times$4 Mueller matrix. In case one is interested in the changes in intensity and polarization as light passes through a series of optical devices. It is straightforward that an entire series of optical elements can be represented by a single matrix $\mathfrak{M}_T$ for the train of elements it encounters hence

$$\mathfrak{M}_T = \prod_{i=1}^{n} \mathfrak{M}_i \tag{A.3}$$

It is again instructive to give a few examples at this point. These include
a) general linear polarizer θ = any

$$\begin{pmatrix} 1 & \cos(2\theta) & \sin(2\theta) & 0 \\ \cos(2\theta) & \cos^2(2\theta) & \cos(2\theta)\sin(2\theta) & 0 \\ \sin(2\theta) & \cos(2\theta)\sin(2\theta) & \sin^2(2\theta) & 0 \\ 0 & 0 & 0 & 0 \end{pmatrix} \tag{A.4}$$

b) general linear retarder: δ = retardance, ρ = azimuth of the fast axis

$$\begin{pmatrix} 1 & 0 & 0 & 0 \\ 0 & \cos(4\rho)\sin^2(\delta/2) + \cos^2(\delta/2) & \sin(4\rho)\sin^2(\delta/2) & -\sin(2\rho)\sin(\delta) \\ 0 & \sin(4\rho)\sin^2(\delta/2) & -\cos(4\rho)\sin^2(\delta/2) + \cos^2(\delta/2) & \cos(2\rho)\sin(\delta) \\ 0 & \sin(2\rho)\sin(\delta) & \cos(2\rho)\sin(\delta) & \cos(\delta) \end{pmatrix} \tag{A.5}$$

c) general elliptical retarder: tan $|\chi|$ is the ellipticity, ρ is the azimuth of the outgoing elliptically polarized light corresponding to the fast axis while δ is the retardance of the sample

$$\begin{pmatrix} 1 & 0 & 0 & 0 \\ 0 & D^2 - E^2 - F^2 + G^2 & 2(DE + FG) & -2(DF + EG) \\ 0 & 2(DE - FG) & -D^2 + E^2 - F^2 + G^2 & 2(DG - EF) \\ 0 & -2(DF - EG) & -2(DG + EF) & -D^2 - E^2 + F^2 + G^2 \end{pmatrix},$$

$$D = \cos(2\chi)\cos(2\rho)\sin(\delta/2), \quad E = \cos(2\chi)\sin(2\rho)\sin(\delta/2);$$

$$F = \sin(2\chi)\sin(\delta/2), \quad G = \cos(\delta/2) \tag{A.6}$$

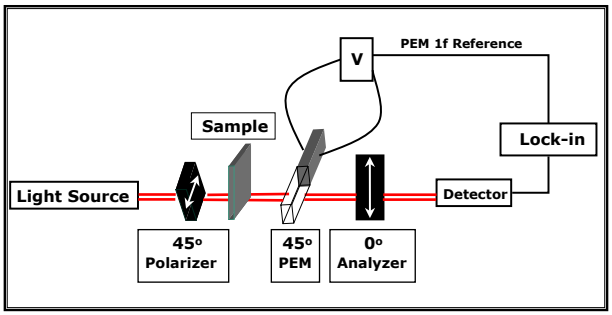

Figure A.1: A schematic diagram for the measurement of polarization properties of *M*-plane GaN

A.2 Experimental setup

The setup for the measurement of the polarization rotation is shown in Fig. A.1 for the case when, the incoming polarization angle $\phi_i = 45^\circ$. All angles are with respect to the unique c axis of the sample. A brief explanation of the setup is as follows: The probe light is coming from the xenon lamp after dispersion by the 0.64 m monochromator. It is then linearly polarized using a Glan-Taylor prism for the incoming angle of $\phi_i = 45^\circ$. The sample is treated as an elliptical polarizer with the ellipticity given as $\eta = \tan(\chi)$ and the final outgoing angle of the major axis to be ϕ_f. After passing through the sample, the polarization of light changes from linear to elliptical polarization. This elliptically polarized light passes through a linear analyzer with a polarization axis set to 0° before being detected by an UV-enhanced Si-based photo-detector. Two lock-in amplifiers are employed to detect the first and the second harmonic of the detected signal which is modulated using the photo-elastic modulator (PEM) which has a frequency of ω. For all measurements a compensating substrate is needed in order to compensate for the birefringence introduced by the $LiAlO_2$ substrate, which itself is a birefringent media. Many groups have reported the use of PEM for the measurement of rotation. [145, 146] In our calculations the sample is treated a linear retarder while PEM is treated as a general Elliptical retarder.

In terms of the Mueller calculus, the experimental setup can be described as follows:

[Output Stokes Vector] = [Analyzer at 0°]X [PEM with axis at 45°]X [Sample] X [Linear Polarizer at $\phi_i = 45^\circ$] X [Input Stokes Vector] which gives rise to the following detected intensity

$$\begin{aligned} V &= -\frac{1}{16}[I - M][-1 + \cos\left(2\phi_f\right)\cos\left(2\tan\chi\right)] \times \\ &\quad \left\{-2 - 2[\mathrm{J}_0(\delta_0) + 2\mathrm{J}_2(\delta_0)\cos(2t\omega)]\cos(2\tan\chi)\sin(2\phi_f)\right. \\ &- \left. 4\mathrm{J}_1(\delta_0)\sin(t\omega)\sin(2\tan\chi)\right\} . \end{aligned} \tag{A.7}$$

Next, the Fourier-Bessel expansions are applied to give us an expression for $V(t)$ in

terms of measurable quantities. The Fourier-Bessel expansions are written as follows:

$$\begin{aligned} V &= -\frac{1}{8}(I-M)(-1+\cos\left[2\phi_f\right]\cos\left[2\tan\chi\right])\times \\ &\quad \left\{1+\left[\mathrm{J}_0(\delta_0)+2\mathrm{J}_2(\delta_0)\cos(2t\omega)\right]\cos(2\tan\chi)\sin(2\phi_f)\right. \\ &+ \left.2\mathrm{J}_1(\delta_0)\sin(t\omega)\sin(2\tan\chi)\right\} \\ &+ \text{higher order harmonics.....} \end{aligned} \tag{A.8}$$

It is desired that the modulated birefringence system be calibrated by setting the electro-optical modulation amplitude by PEM such that $\mathrm{J}_0(\delta_0]$=0 since this greatly simplifies the final data analysis. The following individual components are achieved in this regards.

$$\begin{aligned} V_{DC} &= -\frac{1}{8}[I-M][-1+\cos\left(2\phi_f\right)\cos\left(2\tan\chi\right)]\,, \\ V_{1F} &= -\frac{1}{4}[I-M]\mathrm{J}_1(\delta_0)[-1+\cos\left(2\phi_f\right)\cos\left(2\tan\chi\right)][\sin(2\tan\chi)]\,, \\ V_{2F} &= -\frac{1}{4}(I-M)\mathrm{J}_2(\delta_0)[-1+\cos\left(2\phi_f\right)\cos\left(2\tan\chi\right)][\cos(2\tan\chi)\sin(2\phi_f)]\,, \end{aligned} \tag{A.9}$$

which reduces to the following relations:

$$\begin{aligned} \frac{V_{1F}}{V_{DC}} &= 2\mathrm{J}_1(\delta_0)\sin(2\tan\chi)\,, \\ \frac{V_{2F}}{V_{DC}} &= 2\mathrm{J}_2(\delta_0)\cos(2\tan\chi)\sin(2\phi_f)\,. \end{aligned} \tag{A.10}$$

Using the two relations in Eq. (A.10), we can calculate the outgoing angle ϕ_f of the ellipse to be

$$\sin(2\phi_f) = \frac{\mathrm{J}_1(\delta_0)}{\mathrm{J}_2(\delta_0)}\sqrt{\frac{V_{2F}^2}{[2\mathrm{J}_2(\delta_0)V_{DC}]^2-[V_{1F}]^2}}\,. \tag{A.11}$$

Bibliography

[1] S. Nakamura and G. Fasol. *The Blue Laser Diode*. Springer-Verlag, Berlin, 1997.

[2] F. Bernardini, V. Fiorentini, and D. Vanderbilt. *Phys. Rev. B*, 56:R10024, 1997.

[3] J. E. Northrup and J. Neugebauer. *Phys. Rev. B*, 53:10477, 1996.

[4] P. Waltereit, O. Brandt, A. Trampert, H. T. Grahn, J. Menniger, M. Ramsteiner, M. Reiche, and K. H. Ploog. *Nature (London)*, 406:865, 2000.

[5] Y. J. Sun, O. Brandt, U. Jahn, T. Y. Liu, A. Trampert, S. Cronenberg, S. Dhar, and K. H. Ploog. *J. Appl. Phys.*, 92:5714, 2002.

[6] P. Waltereit, O. Brandt, M. Ramsteiner, R. Uecker, P. Reiche, and K. H. Ploog. *J. Cryst. Growth*, 218:143, 2000.

[7] Y. J. Sun, O. Brandt, S. Cronenberg, S. Dhar, H. T. Grahn, K. H. Ploog, P. Waltereit, and J. S. Speck. *Phys. Rev. B*, 67:041306, 2003.

[8] Y. J. Sun, O. Brandt, and K. H. Ploog. *J. Vac. Sci. Technol. B*, 21:1350, 2003.

[9] M. D. Craven, S. H. Lim, F. Wu, J. S. Speck, and S. P. DenBaars. *Appl. Phys. Lett.*, 81:469, 2002.

[10] B. A. Haskell, F. Wu, S. Matsuda, M. D. Craven, P. T. Fini, S. P. DenBaars, J. S. Speck, and S. Nakamura. *Appl. Phys. Lett.*, 83:1554, 2003.

[11] B. A. Haskell, F. Wu, M. D. Craven, S. Matsuda, P. T. Fini, T. Fujii, K. Fujito, S. P. DenBaars, J. S. Speck, and S. Nakamura. *Appl. Phys. Lett.*, 83:644, 2003.

[12] Hongmei Wang, Changqing Chen, Zheng Gong, Jianping Zhang, Mikhail Gaevski, Ming Su, Jinwei Yang, and M. Asif Khan. *Appl. Phys. Lett.*, 84:499, 2004.

[13] H. M. Ng. *Appl. Phys. Lett.*, 80:4369, 2002.

[14] H. M. Ng, A. Bell, F. A. Ponce, and S. N. G. Chu. *Appl. Phys. Lett.*, 83:653, 2003.

[15] W. H. Sun, J. W. Yang, C. Q. Chen, J. P. Zhang, M. E. Gaevski, E. Kuokstis, V. Adivarahan, H. M. Wang, Z. Gong, M. Su, and M. Asif Khan. *Appl. Phys. Lett.*, 83: 2599, 2003.

[16] C. Chen, V. Adivarahan, J. Yang, M. Shatalov, E. Kuokstis, and M. A. Khan. *Jpn. J. Appl. Phys.*, 42:L1039, 2003.

[17] M. D. Craven, P. Waltereit, J. S. Speck, and S. P. DenBaars. *Appl. Phys. Lett.*, 84: 496, 2004.

[18] T. Koida, S. F. Chichibu, T. Sota, M. D. Craven, B. A. Haskell, J. S. Speck, S. P. DenBaars, and S. Nakamura. *Appl. Phys. Lett.*, 84:3768, 2004.

[19] T. Onuma, A. Chakraborty, B. A. Haskell, S. Keller, S. P. DenBaars, J. S. Speck, S. Nakamura, U. K. Mishra, T. Sota, and S. F. Chichibu. *Appl. Phys. Lett.*, 86: 151918, 2005.

[20] A. Chakraborty, B. A. Haskell, S. Keller, J. S. Speck, S. P. DenBaars, S. Nakamura, and U. K. Mishra. *Appl. Phys. Lett.*, 85:5143, 2004.

[21] A. Chakraborty, S. Keller, C. Meier, B. A. Haskell, S. Keller, P. Waltereit, S. P. DenBaars, S. Nakamura, J. S. Speck, and U. K. Mishra. *Appl. Phys. Lett.*, 86:031901, 2005.

[22] S. Ghosh, P. Waltereit, O. Brandt, H. T. Grahn, and K. H. Ploog. *Appl. Phys. Lett.*, 80:413, 2002.

[23] S. Ghosh, O. Brandt, H. T. Grahn, and K. H. Ploog. *Appl. Phys. Lett.*, 81:3380, 2002.

[24] H. Shen, M. Wraback, J. Pamulapati, P. G. Newman, M. Dutta, Y. Lu, and H. C. Kuo. *Phys. Rev. B*, 47:13933, 1993.

[25] R. Wirth, A. Moritz, C. Geng, F. Scholz, and A. Hangleiter. *Appl. Phys. Lett.*, 69: 2225, 1996.

[26] E. Greger, K. H. Gulden, P. Riel, H. P. Schweizer, M. Moser, G. Schmiedel, P. Kiesel, and G. H. Döhler. *Appl. Phys. Lett.*, 68:2383, 1996.

[27] K. D. Choquette, R. P. Schneider, Jr., and J. A. Lott. *Opt. Lett.*, 19:969, 1994.

[28] Y. H. Chen, C. I. Wilkinson, J. Woodhead, J. P. R. David, C. C. Button, and P. N. Robson. *IEEE Photonics Technol. Lett.*, 9:143, 1997.

[29] E. Greger, P. Riel, M. Moser, T. Kippenberg, P. Kiesel, and G. H. Döhler. *Appl. Phys. Lett.*, 71:3245, 1997.

[30] J. Krauss, T. Kippenberg, J. Spieler, P. Kiesel, G. H. Döhler, and M. Moser. *Electron. Lett.*, 35:1878, 1999.

[31] H. Shen, M. Wraback, J. Pamulapati, M. Dutta, P. G. Newman, A. Ballato, and Y. Lu. *Appl. Phys. Lett.*, 62:2908, 1993.

[32] H. Shen, J. Pamulapati, M. Wraback, M. Taysing-Lara, M. Dutta, H. C. Kuo, and Y. Lu. *IEEE Photonics Technol. Lett.*, 6:700, 1994.

[33] D. S. McCallum, X. R. Huang, A. L. Smirl, D. Sun, and E. Towe. *Appl. Phys. Lett.*, 66:2885, 1995.

[34] P. Misra, Yue Jun Sun, O. Brandt, and H. T. Grahn. *Appl. Phys. Lett.*, 83:4327, 2003.

[35] K. Omae, T. Flissikowski, P. Misra, O. Brandt, H. T. Grahn, K. Kojima, and Y. Kawakami. *Appl. Phys. Lett.*, 86:191909, 2005.

[36] T. Deguchi, K. Sekiguchi, A. Nakamura, T. Sota, R. Matsuo1, S. Chichibu, and S. Nakamura. *Jpn. J. Appl. Phys.*, 38:L914, 1999.

[37] N. Grandjean, B. Damilano, S. Dalmasso, M. Leroux, M. Laugt, and J. Massies. *J. Appl. Phys.*, 86:3714, 1999.

[38] M. D. Craven, S. H. Lim, F. Wu, J. S. Speck, and S. P. DenBaars. *Appl. Phys. Lett.*, 81:469, 2002.

[39] M. D. Craven, S. H. Lim, F. Wu, J. S. Speck, and S. P. DenBaars. *Appl. Phys. Lett.*, 81:1201, 2002.

[40] P. Waltereit, O. Brandt, and K. H. Ploog. *Appl. Phys. Lett.*, 75:2029, 1999.

[41] R. R. Vanfleet, J. A. Simmons, H. P. Maruska, D. W. Hill, M. M. C. Chou, and B. H. Chai. *Appl. Phys. Lett.*, 83:1139, 2003.

[42] C. Q. Chen, M. E. Gaevski, W. H. Sun, E. Kuokstis, J. P. Zhang, R. S. Q. Fareed, H. M. Wang, J. W. Yang, G. Simin, M. A. Khan, Herbert-Paul Maruska, David W. Hill, Mitch M. C. Chou, and Bruce Chai. *Appl. Phys. Lett.*, 81:3194, 2002.

[43] N. W. Ashcroft and N. D. Mermin. *Solid State Physics*. Thomson Brooks/Cole, California, 1976.

[44] O. Brandt, P. Waltereit, and K. H. Ploog. *J. Phys. D*, 35:577, 2002.

[45] M. Marezio. *Acta Crystallogr.*, 19:396, 1965.

[46] H. Morkoç. *Nitride Semiconductors and Devices*. Springer, Berlin, 1999.

[47] P. Waltereit, O. Brandt, K. H. Ploog, M. A. Tagliente, and L. Tapfer. *Phys. Rev. B*, 66:165322, 2002.

[48] E. O. Kane. *J. Phys. Chem. Solids*, 1:249, 1957.

[49] M. Suzuki. PhD thesis, Central Research Laboratories, Matsusita electric Co. Ltd, Japan, 1997.

[50] G. L. Bir and G. E. Pikus. *Symmetry and Strain Induced Effects in Semiconductors*. Wiley, New York, 1974.

[51] M. Suzuki, T. Uenoyama, and A. Yanase. *Phys. Rev. B*, 52:8132, 1995.

[52] S. L. Chuang and C. S. Chang. *Phys. Rev. B*, 54:2491, 1996.

[53] S. Kamiyama, K. Ohnaka, M. Suzuki, and T. Uenoyama. *Jpn. J. Appl. Phys.*, 34: L821, 1995.

[54] W. Shan, R. J. Hauenstein, A. J. Fischer, J. J. Song, W. G. Perry, M. D. Bremser, R. F. Davis, and B. Goldenberg. *Phys. Rev. B*, 54:13460, 1996.

[55] S. Ghosh, P. Waltereit, O. Brandt, H. T. Grahn, and K. H. Ploog. *Phys. Rev. B*, 65: 075202, 2002.

[56] B. Gil and A. Alemu. *Phys. Rev. B*, 56:12446, 1997.

[57] T. Ohtoshi, A. Niwa, and T. Kuroda. *J. Appl. Phys.*, 82:1518, 1997.

[58] M. Suzuki and T. Uenoyama. *J. Appl. Phys.*, 80:6868, 1996.

[59] M. Suzuki and T. Uenoyama. *Jpn. J. Appl. Phys.*, 35:1420, 1996.

[60] A. Alemu, B. Gil, M. Julier, and S. Nakamura. *Phys. Rev. B*, 57:3761, 1998.

[61] M. Yamaguchi, T. Yagi, T. Azuhata, T. Sota, K. Suzuki, S. Chichibu, and S. Nakamura. *J. Phys.: Condens. Matter*, 9:241, 1997.

[62] K. Domen, K. Horino, A. Kuramata, and T. Tanahashi. *Appl. Phys. Lett.*, 70:987, 1997.

[63] A. Shikanai, T.i Azuhata, T. Sota, S. Chichibu, A. Kuramata, K. Horino, and S. Nakamura. *J. Appl. Phys.*, 81:417, 1997.

[64] A. Polian, M. Grimsditch, and I. Grzegory. *J. Appl. Phys.*, 79:3343, 1996.

[65] R. B. Schwarz, K. Khachaturyan, and E. R. Weber. *Appl. Phys. Lett.*, 70:1122, 1997.

[66] C. Deger, E. Born, H. Angerer, O. Ambacher, M. Stutzmann, J. Hornsteiner, E. Riha, and G. Fischerauer. *Appl. Phys. Lett.*, 72:2400, 1998.

[67] A. F. Wright. *J. Appl. Phys.*, 82:2833, 1997.

[68] K. Kim, Walter R. L. Lambrecht, and B. Segall. *Phys. Rev. B*, 53:16310, 1996.

[69] J.-M. Wagner and F. Bechstedt. *Phys. Rev. B*, 66:115202, 2002.

[70] K. Shimada, T. Sota, and K. Suzuki. *J. Appl. Phys.*, 84:4951, 1998.

[71] T. Deguchi, D. Ichiryu, K. Toshikawa, K. Sekiguchi, T. Sota, R. Matsuo, T. Azuhata, M. Yamaguchi, T. Yagi, S. Chichibu, and S. Nakamura. *J. Appl. Phys.*, 86:1860, 1999.

[72] S. Yu. Davydov. *Semiconductors*, 36:41, 2002.

[73] K. Torii, T. Deguchi, T. Sota, K. Suzuki, S. Chichibu, and S. Nakamura. *Phys. Rev. B*, 60:4723, 1999.

[74] M. Suzuki and T. Uenoyama. *Jpn. J. Appl. Phys.*, 35:543, 1996.

[75] David. J. Griffiths. *Introduction to Electrodynamics*. Prentice Hall of India, New Delhi, 1997.

[76] H. T. Grahn. *Introduction to Semiconductor Physics*. World Scientific, Singapore, 1999.

[77] B. Gil, editor. *Group III Nitride Semiconductor Compounds*. Clarendon Press, Oxford, 1998.

[78] O. J. Glembocki, B. V. Shanabrook, N. Bottka, W. T. Beard, and J. Comas. *Appl. Phys. Lett.*, 46:970, 1985.

[79] H. Shen, S. H. Pan, Fred H. Pollak, M. Dutta, and T. R. AuCoin. *Phys. Rev. B*, 36: 9384, 1987.

[80] M. Balkanski, editor. *Optical Properties of Solids*. North-Holland, Amsterdam, 1980.

[81] E. F. Schubert, I. D. Goepfert, and J. M. Redwing. *Appl. Phys. Lett.*, 71:3224, 1997.

[82] In-Hwan Lee, J. J. Lee, P. Kung, F. J. Sanchez, and M. Razeghi. *Appl. Phys. Lett.*, 74:102, 1999.

[83] D. A. Turnbull, X. Li, S. Q. Gu, E. E. Reuter, J. J. Coleman, and S. G. Bishop. *J. Appl. Phys.*, 80:4609, 1996.

[84] D. M. Hofmann, D. Kovalev, G. Steude, B. K. Meyer, A. Hoffmann, L. Eckey, R. Heitz, T. Detchprom, H. Amano, and I. Akasaki. *Phys. Rev. B*, 52:16702, 1995.

[85] K. P. Korona, A. Wysmolek, K. Pakula, R. Stepniewski, J. M. Baranowski, I. Grzegory, B. Lucznik, M. Wroblewski, and S. Porowski. *Appl. Phys. Lett.*, 69:788, 1996.

[86] W. Shan, T. J. Schmidt, X. H. Yang, S. J. Hwang, J. J. Song, and B. Goldenberg. *Appl. Phys. Lett.*, 66:985, 1995.

[87] K. Kornitzer, T. Ebner, K. Thonke, R. Sauer, C. Kirchner, V. Schwegler, M. Kamp, M. Leszczynski, I. Grzegory, and S. Porowski. *Phys. Rev. B*, 60:1471, 1999.

[88] M. Mayer, A. Pelzmann, M. Kamp, K. J. Ebeling, H. Teisseyre, G. Nowak, M. Leszczynski, I. Grzegory, S. Porowski, and G. Karczewski. *Jpn. J. Appl. Phys.*, 36:L1634, 1997.

[89] R. Dingle, D. D. Sell, S. E. Stokowski, and M. Ilegems. *Phys. Rev. B*, 4:1211, 1971.

[90] B. Monemar. *Phys. Rev. B*, 10:676, 1974.

[91] D. Volm, K. Oettinger, T. Streibl, D. Kovalev, M. Ben-Chorin, J. Diener, B. K. Meyer, J. Majewski, L. Eckey, A. Hoffmann, H. Amano, I. Akasaki, K. Hiramatsu, and T. Detchprohm. *Phys. Rev. B*, 53:16543, 1996.

[92] J. J. Hopfield. *J. Phys. Chem. Solids*, 15:97, 1960.

[93] R. Stepniewski, K. P. Korona, A. Wysmolek, J. M. Baranowski, K. Pakula, M. Potemski, G. Martinez, I. Grzegory, and S. Porowski. *Phys. Rev. B*, 56:15151, 1997.

[94] B. Gil, O. Briot, and R-L. Aulombard. *Phys. Rev. B*, 52:17028, 1995.

[95] J. Jayapalan, B. J. Skromme, R. P. Vaudo, and V. M. Phanse. *Appl. Phys. Lett.*, 73: 1188, 1998.

[96] N. N. Syrbu, I. M. Tiginyanu, V. V. Ursaki, V. V. Zalamai, V. Popa, S. M. Hubbard, and D. Pavlidis. *MRS Internet J. Nitride Semicond. Res*, 8, 2003.

[97] B. J. Skromme, J. Jayapalan, R. P. Vaudo, and V. M. Phanse. *Appl. Phys. Lett.*, 74: 2358, 1999.

[98] K. Kornitzer, T. Ebner, M. Grehl, K. Thonke, R. Sauer, C. Kirchner, V. Schwegler, M. Kamp, M. Leszczynski, I. Grzegory, and S. Porowski. *Phys. Status Solidi B*, 216:5, 1999.

[99] Y. Kawakami, Zhi Gang Peng, Y. Narukawa, S. Fujita, S. Fujita, and S. Nakamura. *Appl. Phys. Lett.*, 69:1414, 1996.

[100] K. Pakula, A. Wysmolek, K. P. Korona, J. M. Baranowski, R. StImagepniewski, I. Grzegory, M. BoImagekowski, J. Jun, S. Krukowski, M. Wróblewski, and S. Porowski. *Solid State Commun.*, 97:919, 1996.

[101] F. Fisher, D. Volm, D. Kovalev, B. Averboukh, A. Graber, H. C. Alt, and B. K. Meyer. *Mater. Sci. and Eng. B*, 43:192, 1997.

[102] B. Santic, C. Merz, U. Kaufmann, R. Niebuhr, H. Obloh, and K. Bachem. *Appl. Phys. Lett.*, 71:1837, 1997.

[103] G. D. Chen, M. Smith, J. Y. Lin, H. X. Jiang, M. Asif Khan, and C. J. Sun. *Appl. Phys. Lett.*, 67:1653, 1995.

[104] D. G. Chtchekine, G. D. Gilliland, Z. C. Feng, S. J. Chua, D. J. Wolford, S. E. Ralph, M. J. Schurman, and I. Ferguson. *MRS Internet J. Nitride Semicond. Res*, 4S1:G6.47, 1999.

[105] C. H. Hong, D. Pavlidis, S. W. Brown, and S. C. Rand. *J. Appl. Phys.*, 77:1705, 1995.

[106] L. Eckey, J.-Ch. Holst, P. Maxim, R. Heitz, A. Hoffmann, I. Broser, B. K. Meyer, C. Wetzel, E. N. Mokhov, and P. G. Baranov. *Appl. Phys. Lett.*, 68:415, 1996.

[107] C. Wetzel, S. Fischer, J. Kruger, E. E. Haller, R. J. Molnar, T. D. Moustakas, E. N. Mokhov, and P. G. Baranov. *Appl. Phys. Lett.*, 68:2556, 1996.

[108] W. Rieger, R. Dimitrov, D. Brunner, E. Rohrer, O. Ambacher, and M. Stutzmann. *Phys. Rev. B*, 54:17596, 1996.

[109] N. Grandjean, M. Leroux, M. Laugt, and J. Massies. *Appl. Phys. Lett.*, 71:240, 1997.

[110] C. Trager-Cowan, S. McArthur, P. G. Middleton, K. P. O'Donnel, D. Zubia, and S. D. Hersee. *Mater. Sci. and Eng. B*, 59:235, 1999.

[111] W. Grieshaber, E. F. Schubert, I. D. Goepfert, Jr. R. F. Karlicek, M. J. Schurman, and C. Tran. *J. Appl. Phys.*, 80:4615, 1996.

[112] C. F. Li, Y. S. Huang, L. Malikova, and F. H. Pollak. *Phys. Rev. B*, 55:9251, 1997.

[113] Y. P. Varshni. *Physica*, 34:149, 1967.

[114] R. Pässler. *J. Appl. Phys.*, 88:2570, 2000.

[115] R. Pässler. *J. Appl. Phys.*, 89:6235, 2001.

[116] R. Pässler. *J. Appl. Phys.*, 90:3956, 2001.

[117] R. Pässler. *Phys. Rev. B*, 66:085201, 2002.

[118] H. Teisseyre, P. Perlin, T. Suski, I. Grzegory, S. Porowski, J. Jun, A. Pietraszko, and T. D. Moustakas. *J. Appl. Phys.*, 76:2429, 1994.

[119] W. Shan, T. Schmidt, X. H. Yang, J. J. Song, and B. Goldenberg. *J. Appl. Phys.*, 79: 3691, 1996.

[120] S. Chichibu, T. Mizutani, T. Shioda, H. Nakanishi, T. Deguchi, T. Azuhata, T. Sota, and S. Nakamura. *Appl. Phys. Lett.*, 70:3440, 1997.

[121] F. Calle, F. J. Sánchez, J. M. G. Tijero, M. A. Sánchez-García, E. Calleja, and R. Beresford. *Semicond. Sci. Technol.*, 12:1396, 1997.

[122] H. Y. Zhang, X. H. He, Y. H. Shih, M. Schurman, Z. C. Feng, and R. A. Stall. *Appl. Phys. Lett.*, 69:2953, 1996.

[123] G. Yu, H. Ishikawa, T. Egawa, T. Soga, J. Watanabe, T. Jimbo, and M. Umeno. *Jpn. J. Appl. Phys.*, 36:L1029, 1997.

[124] D. E. Aspnes. *Surf. Sci.*, 37:418, 1973.

[125] Poochi Yeh. *Optical Waves in Layered Media*. Wiley-Interscience, New York, 1988.

[126] M. Born and E. Wolf. *Principles of Optics*. Pergamon, Oxford, 1965.

[127] B. Harbecke. *Appl, Phys. B*, 39:165, 1986.

[128] R. Swanepoel. *J. Phys. E*, 16:1214, 1983.

[129] M. J. Bergmann, U. Ozgur, Jr. H. C. Casey, H. O. Everitt, and J. F. Muth. *Appl. Phys. Lett.*, 75:67, 1999.

[130] C. X. Lian, X. Y. Li, and J. Liu. *Semicond. Sci. Technol.*, 19:417, 2004.

[131] G. Yu, G. Wang, H. Ishikawa, M. Umeno, T. Soga, T. Egawa, J. Watanabe, and T. Jimbo. *Appl. Phys. Lett.*, 70:3209, 1997.

[132] E. C. Freeman and W. Paul. *Phys. Rev. B*, 20:716, 1979.

[133] J. C. Manifacier, J. Gasiot, and J. P. Fillard. *J. Phys. E*, 9:1002, 1976.

[134] R. Allmann, W. Pies, and W. Weiss, editors. *Landolt-Börnstein, Series III*, volume 7d2. Springer, Berlin, 1980.

[135] H. Sobotta, H. Neumann, R. Franzheld, and W. Seifert. *Phys. Stat. Sol.*, 174:K57, 1992.

[136] D. Ritter and K. Weiser. *Opt. Commun.*, 57:336, 1986.

[137] K. Driss-Khodja, A. Gheorghiu, and M. L. Theye. *Opt. Commun.*, 55:169, 1985.

[138] R. W. Martin, P. G. Middleton, K. P. O'Donnell, and W. Van der Stricht. *Appl. Phys. Lett.*, 74:263, 1999.

[139] M. Wraback, H. Shen, S. Liang, C. R. Gorla, and Y. Lu. *Appl. Phys. Lett.*, 74:507, 1999.

[140] B. Rau, P. Waltereit, O. Brandt, M. Ramsteiner, K. H. Ploog, J. Puls, and F. Henneberger. *Appl. Phys. Lett.*, 77:3343, 2000.

[141] Yue Jun Sun, O. Brandt, M. Ramsteiner, H. T. Grahn, and K. H. Ploog. *Appl. Phys. Lett.*, 82:3850, 2003.

[142] N. F. Gardner, J. C. Kim, J. J. Wierer, Y. C. Shen, and M. R. Krames. *Appl. Phys. Lett.*, 86:111101, 2005.

[143] M. A. Reshchikov and H. Morkoc. *J. Appl. Phys.*, 97:061301, 2005.

[144] D. S. Kliger, J. W. Lewis, and C. E. Randall. *Polarized light in optics and spectroscopy*. Academic Press, Boston, 1990.

[145] T. C. Oakberg. Hinds Instruments, Hillsboro, OR, 1992.

[146] J. R. Mackey, K. K. Das, S. L. Anna, and G. H. McKinley. *Meas. Sci. and Technol.*, 10:946, October 1999.

Acknowledgement

This thesis could not have existed without the help of many people who have given me support, encouragement and inspiration during the course of my work. I would especially like to thank the following persons...

... Prof. Dr. Klaus H. Ploog for giving me the opportunity to do my PhD thesis at PDI, allowing me to learn MBE growth in addition to doing spectroscopy and for providing the financial means to attend an important international conference. His continued support and encouragement is gratefully appreciated.

... Prof. Dr. Oliver Benson and Prof. Dr. Elías Muñoz for taking their time to review this work.

... Prof. Dr. Holger T. Grahn for being my advisor. Without his help, the interpretation of the results and the models used in this work will not exist as written in this thesis. I also thank him for his constant guidance, engagement and encouragement. His systematic approach and clarity in thinking is something I will always try to emulate.

...Dr. Oliver Brandt who introduced me to the world of molecular beam epitaxy and x-ray diffraction. His infectious energy, positive attitude, and his commitment to research taught me a lot. Thanks.

...Dr. Lutz Schrottke for lending his continued support and critical discussion concerning physical and technical problems in the PL lab.

...Dr. Manfred Ramsteiner for helping with the measurements in the micro-PL lab and for his help on computer related problems.

...Dr. Manfred Giehler for discussions we had on the theory of matrix method.

...Dr. Yue Jun Sun for providing me with the *M*-plane samples and sharing a good time together.

...Dr. Kunimichi Omae who introduced me to time-resolved spectroscopy and for thought provoking scientific discussions.

...Dr. Timur Flissikowski for instructive discussions on a lot of physical issues. I

also thank him for proofreading this thesis and coming up with various suggestions to make it better.

...Dr. Sandip Ghosh who introduced me to the band structure calculations and PR measurements.

...Tommy Ive for teaching me the technical issues concerning the MBE. We had a good time together discussing topics related to physics and other profound subjects.

...H. von Kiedrowski for his help with cleaving γ-$LiAlO_2$ substrates and A-K. Bluhm for carrying out SEM measurements.

...Hans-Peter Schönherr for his technical help with growth and for teaching me the various aspects of MBE.

...Dr. Helmar Kostial for his help on metal contacts and I-V measurements.

...Dr. Atsushi Kawaharazuka for sharing his knowledge of physics and computers with me.

...Dr. Fumitaro Ishikawa for providing the *C*-plane GaN sample and for various growth related discussions.

...Prof. Dr. J. Speck for providing the *A*-plane GaN samples.

...Ilka Schuster for her help with image processing.

I also appreciate the good time shared with Devender S. Negi, Pranaba K. Muduli, Dillip K. Satapathy, Dr. Jyoti Mohanty, Jaya Datta, Dr. Gregor Mußler, Prasad Bhalerao, Sharvari Dixit, Dr. S. Dhar, Dr. Yukihiko Takagaki, and Dr. Jean-Michel Chauveau. I wish them all a very bright future.

Lastly, I would like to express my deepest gratitude to my father Nagendra Dutt and my mother Susheela. Their constant support, encouragement and love kept me going. I dedicate this work to them.

Curriculum Vitae

Name:	PranobMisra
Geburtstag:	17. Januar 1979
Geburtsort:	Dehradun, Indien
08.07.2002	Promotionsstudent an der Humboldt-Universität zu Berlin und am Paul-Drude Institut für Festkörperelektronik in der Arbeitsgruppe von Herrn Prof. Dr. H. T. Grahn unter Betreuung von Herrn Prof. Dr. K. H. Ploog
28.05.2002	Master of Science (M.Sc.) Indian Institute of Technology, Kanpur, Indien Thema: "Optical Properties of Organic Semiconductor Thin Films using technique such as Null Ellipsometry and Interferometry"
08.1997 – 04.2002	Integrated 5-year Master of Science (M.Sc.) in Physik Indian Institute of Technology, Kanpur, Indien
03.1989 – 04.1997	High School in Dehradun, Indien
03.1984 – 02.1989	Primary School in Dehradun, Indien

Selbständigkeitserklärung

Hiermit erkläre ich, die vorliegende Arbeit *Optical polarization anisotropy in nonpolar GaN thin films due to crystal symmetry and anisotropic strain* selbständig und nur unter Verwendung der gemäß §6 Absatz (3) angegebenen Hilfen und Hilfsmittel angefertigt zu haben.

Ich habe mich an keiner anderen Universität um einen Doktorgrad beworben und besitze auch keinen entsprechenden Doktorgrad.

Ich erkläre die Kenntnis der dem Verfahren zugrunde liegenden Promotionsordnung der Mathematisch-Naturwissenschaftlichen Fakultät I der Humboldt-Universität zu Berlin.

PranobMisra
6. October 2005